



# Overview of constitutive laws, kinematics, homogenization and multiscale methods in crystal plasticity finite-element modeling: Theory, experiments, applications

F. Roters<sup>a</sup>, P. Eisenlohr<sup>a</sup>, L. Hantcherli<sup>a</sup>, D.D. Tjahjanto<sup>a</sup>, T.R. Bieler<sup>b</sup>, D. Raabe<sup>a,\*</sup>

<sup>a</sup> Max-Planck-Institut für Eisenforschung, Düsseldorf, Germany

<sup>b</sup> Chemical Engineering and Materials Science, Michigan State University, East Lansing, MI, USA

Received 27 February 2009; received in revised form 19 October 2009; accepted 24 October 2009

Available online 11 December 2009

## Abstract

This article reviews continuum-based variational formulations for describing the elastic–plastic deformation of anisotropic heterogeneous crystalline matter. These approaches, commonly referred to as crystal plasticity finite-element models, are important both for basic microstructure-based mechanical predictions as well as for engineering design and performance simulations involving anisotropic media. Besides the discussion of the constitutive laws, kinematics, homogenization schemes and multiscale approaches behind these methods, we also present some examples, including, in particular, comparisons of the predictions with experiments. The applications stem from such diverse fields as orientation stability, microbeam bending, single-crystal and bicrystal deformation, nanoindentation, recrystallization, multiphase steel (TRIP) deformation, and damage prediction for the microscopic and mesoscopic scales and multiscale predictions of rolling textures, cup drawing, Lankfort ( $r$ ) values and stamping simulations for the macroscopic scale.

© 2009 Acta Materialia Inc. Published by Elsevier Ltd. All rights reserved.

**Keywords:** Crystal plasticity; Twinning; Indentation; Multiphase steel; Anisotropy

## 1. Introduction

### 1.1. Crystalline anisotropy and the spirit of the crystal plasticity finite-element method

The elastic–plastic deformation of crystalline aggregates depends on the direction of loading, i.e. crystals are mechanically anisotropic. This phenomenon is due to the anisotropy of the elastic tensor and to the orientation dependence of the activation of the crystallographic deformation mechanisms (dislocations, twins, martensitic transformations). A consequence of crystalline anisotropy is that the associated mechanical phenomena such as shape change, crystallographic texture, strength, strain hardening, deformation-induced surface roughening and damage

are also orientation dependent. This is not a trivial statement as it implies that mechanical parameters of crystalline matter are tensor quantities.

An example is the uniaxial stress–strain curve, which is the most important mechanical measure in structural materials design. The statement above means that such flow curves represent an incomplete description of plastic deformation as they reduce a six-dimensional yield surface and its change upon loading to a one-dimensional (scalar) yield curve (see Fig. 1). Another consequence of this statement is that the crystallographic texture (orientation distribution) and its evolution during forming is a quantity that is inherently connected with plasticity theory. Texture can hence be used to describe the integral anisotropy of polycrystals in terms of the individual tensorial behavior of each grain and the orientation-dependent boundary conditions among the crystals. Formally, the connection between shear and texture evolution becomes clear from the fact that any deformation gradient can be expressed as the combination

\* Corresponding author.

E-mail address: [d.raabe@mpie.de](mailto:d.raabe@mpie.de) (D. Raabe).

URL: <http://www.mpie.de> (D. Raabe).

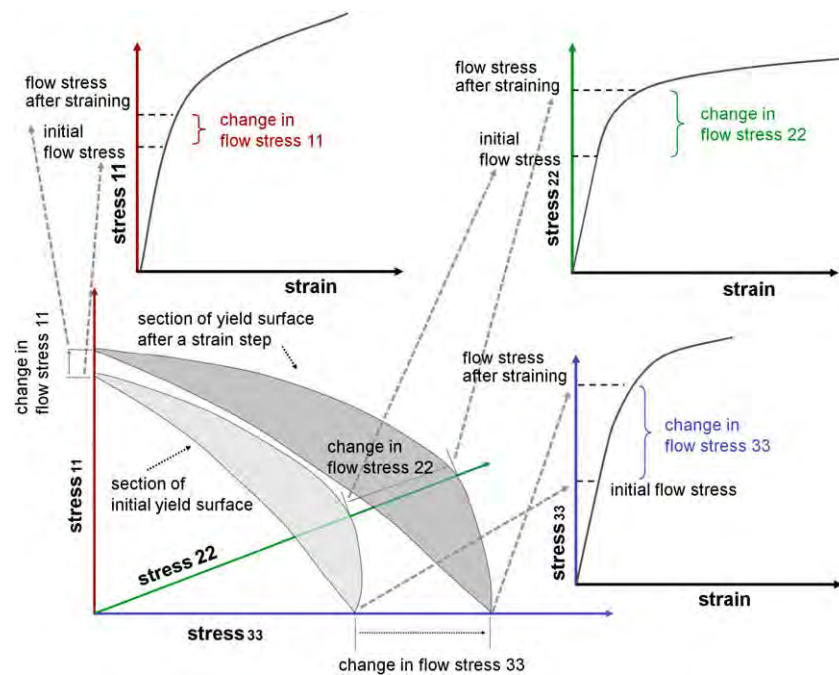


Fig. 1. Flow stress and strain hardening of anisotropic materials are tensor quantities.

of its skew-symmetric portion, which represents a pure rotation leading to texture changes if not matched by the rotation implied by plastic shear, and a symmetric tensor that is a measure of pure stretching. Plastic shear hence creates both shape and orientation changes, except for certain highly symmetric shears. Therefore, a theory of the mechanical properties of crystals must include, first, the crystallographic and anisotropic nature of those mechanisms that create shear, and second, the orientation(s) of the crystal(s) studied relative to the applied boundary conditions (e.g. loading axis, rolling plane).

Early approaches to describe anisotropic plasticity under simple boundary conditions have considered these aspects, such as, for instance, the Sachs [3], Taylor [4], Bishop–Hill [5,6] or Kröner [7] formulations. However, these approaches were neither designed for considering explicitly the mechanical interactions among the crystals in a polycrystal nor for responding to complex internal or external boundary conditions (Fig. 2). Instead, they are built on certain simplifying assumptions of strain or stress homogeneity to cope with the intricate interactions within a polycrystal.

For that reason variational methods in the form of finite-element (FE) approximations have gained enormous momentum in this field. These methods, which are referred to as crystal plasticity finite-element (CPFE) models, are based on the variational solution of the equilibrium of the forces and the compatibility of the displacements using a weak form of the principle of virtual work in a given finite-volume element. The entire sample volume under consideration is discretized into such elements. The essential step which renders the deformation kinematics of this approach a crystal plasticity formulation is the fact that the velocity gradient is written in dyadic form. This reflects

the tensorial crystallographic nature of the underlying defects that lead to shear and consequently, to both shape changes (symmetric part) and lattice rotations (skew-symmetric part)—see Section 3. This means that the CPFE method has evolved as an attempt to employ some of the extensive knowledge gained from experimental and theoretical studies of single-crystal deformation and dislocations to inform the further development of continuum field theories of deformation. The general framework supplied by variational crystal plasticity formulations provides an attractive vehicle for developing a comprehensive theory of plasticity that incorporates existing knowledge of the physics of deformation processes [8–10] into the computational tools of continuum mechanics [11,12] with the aim of developing advanced and physically based design methods for engineering applications [13].

One main advantage of CPFE models lies in their ability to solve crystal mechanical problems under complicated internal and/or external boundary conditions. This aspect is not a mere computational advantage but is an inherent part of the physics of crystal mechanics since it enables one to tackle those boundary conditions that are imposed by inter- and intra-grain micromechanical interactions (see Fig. 3) [14]. This is not only essential to study in-grain or grain cluster mechanical problems but also to better understand the often quite abrupt mechanical transitions at interfaces [15].

However, the success of CPFE methods is not only built on their efficiency in dealing with complicated boundary conditions. They also offer great flexibility with respect to including various constitutive formulations for plastic flow and hardening at the elementary shear system level. The constitutive flow laws that were suggested during the last

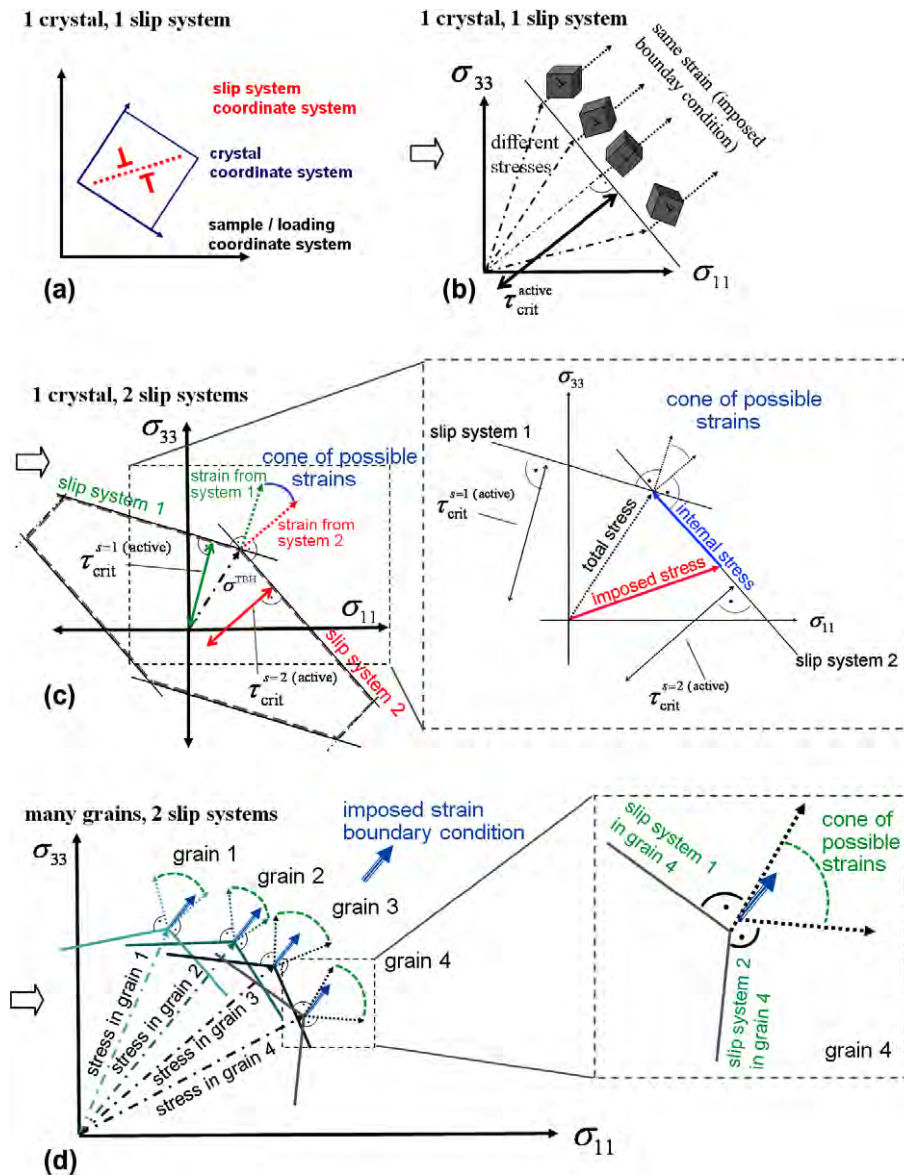


Fig. 2. Schematic presentation of the growing complexity of grain-scale mechanics with respect to the equilibrium of the forces and the compatibility of the displacements for different situations. (a and b) Single slip problem in a single crystal presented in stress space. (c) Part of a single-crystal yield surface with two slip systems. (d) Multislip situation in a polycrystal where all different crystals have to satisfy an assumed imposed strain in their respective yield corners. If the strain is homogeneous, this situation leads to different stresses in each crystal [1,2].  $\tau_{crit}$ : critical shear stress.  $\sigma^{TBH}$ : Taylor–Bishop–Hill stress state (stress required to reach a yield corner).

decades have gradually developed from empirical viscoplastic formulations [16,17] into physics-based multiscale internal-variable models of plasticity, including a variety of size-dependent effects and interface mechanisms [9,18–26]. In this context it should be emphasized that the FE method itself is not the actual model but the variational solver for the underlying constitutive equations that map the anisotropy of elastic–plastic shears associated with the various types of lattice defects (e.g. dislocations, twins, martensite). Since its first introduction by Peirce et al. in 1982 [27] the CPFE method has matured into a whole family of constitutive and numerical formulations that has been applied to a broad variety of crystal mechanical problems (Table 1).

## 1.2. The crystal plasticity finite-element method as a multimechanism and multiphysics platform

A conceptual advantage of the CPFE approach is that it may not only include dislocations but also other mechanisms which follow dyadic kinematics such as martensite formation [74,80], shear band formation (e.g. in glassy matter) [208,209], mechanical twinning [164–166,169] and even superplastic grain boundary shear [41,45]. The CPFE method allows the user to implement these shear mechanisms including their interactions. But it also adds complexity to the model: the use of different competing crystallographic deformation mechanisms within a CPFE model requires the formulation of local homogenization



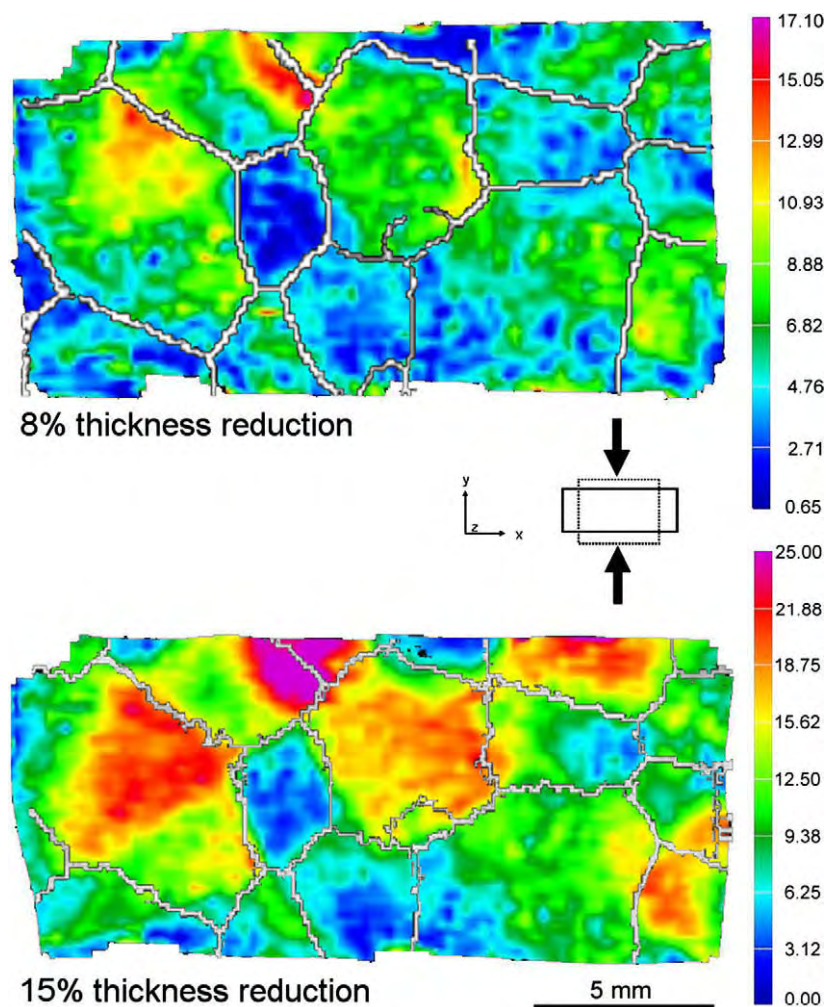


Fig. 3. Experimental example of the heterogeneity of plastic deformation at the grain and subgrain scale using an aluminum polycrystal with large columnar grains [14]. The images show the distribution of the accumulated von Mises equivalent strain in a specimen after 8% and 15% plane strain sample thickness reduction (the deformation is given in % of  $\Delta d/d$ , where  $d$  is the sample extension along compression direction). The experiment was conducted in a lubricated channel–die set-up. The strains were determined using digital image correlation. The high-angle grain boundaries indicated by white lines were taken from electron backscatter diffraction microtexture measurements. The equivalent strains differ across some of the grain boundaries by a factor of 4–5, giving evidence of the enormous orientation-dependent heterogeneity of plasticity even in pure metals.

rules [1,142]. This means that at some material points only one type of deformation mechanism (e.g. dislocation slip) may occur, while in others a mix (e.g. dislocations and twins) must be considered within the same volume portion. The latter situation requires appropriate submodels that describe the evolving fractions (e.g. of the twinned volume) and the interactions of coexisting and competing deformation mechanisms at the same field point (Fig. 4). An aspect that increases complexity in such cases is the possibility that deformation martensite or twins may, after their formation, undergo further plastic deformation or create accommodation strains related to volume changes. Some of these aspects will be discussed in Sections 5 and 6.

Another strength of the CPFE method is the close connection between shape change, rotation and geometrically necessary dislocations (GNDs) [210–213]. This allows one to implement constitutive laws that treat mechanical size effects in conjunction with local orientation gradients

[24]. This point is relevant for size-dependent plasticity modeling, as the polarized portions of dislocation arrays (which are often conceptually treated as GNDs),<sup>1</sup> such as anticipated in many size effect models, must necessarily coincide with orientation gradients [210]. Such lattice rotations are nowadays accessible to precise and high-resolution measurements in 2-D and 3-D so that corresponding models can be tested [95,98,171,177,214–216].

<sup>1</sup> It should be noted that a dislocation does actually not know whether it is a geometrically necessary one or a statistical one unless its state is specified in the context of an adequately defined Frank loop around a material portion of interest. Furthermore, GNDs are, from a physics standpoint, not a separate type of lattice defect when compared to statistically stored dislocations, i.e. their evolution must be embedded in a unified kinetic framework so that they can assume either state depending on the local lattice defect configuration.

Table 1  
Some examples for different applications of the CPFE method.

Application of the CPFE method	Reference
Surface roughening, ridging, roping, thin film mechanics	Becker [28], Raabe et al. [15], Zhao et al. [29], Yue [30], Siska et al. [31], Zhao et al. [32]
Grain boundary mechanics, Hall–Petch behavior, grain interaction, grain size effects, strain gradient effects, non-local formulations, interface mechanics, superplasticity	Becker and Panchanadeeswaran [33], Mika and Dawson [34], Acharya and Beaudoin [35], Meissonnier et al. [36], Barbe et al. [37], Raabe et al. [38], Evers et al. [20], Park et al. [39], Clarke et al. [40], Wei and Anand [41], Fu et al. [42], Evers et al. [26], Evers et al. [21], Diard et al. [43], Bate and Hutchinson [44], Wei et al. [45], Murphy et al. [46], Deka et al. [47], Ma et al. [24], Ma et al. [25], Counts et al. [48], Gurtin et al. [49], Venkatramani et al. [50], Okumura et al. [51], Gerken and Dawson [52], Gerken and Dawson [53], Kuroda and Tvergaard [54], Bitzek et al. [55], Borg et al. [56], Li et al. [57]
Creep, high temperature deformation, diffusion mechanisms	McHugh and Mohrmann [58], Balasubramanian and Anand [59], Hasija et al. [60], Bower and Wininger [61], Venkatramani et al. [50], Agarwal et al. [62], Venkataramani et al. [63], Xu et al. [64]
Dislocation-based constitutive modeling	Arsenlis and Parks [18], Arsenlis and Parks [19], Arsenlis and Tang [65], Arsenlis et al. [9], Evers et al. [20], Evers et al. [21], Cheong and Busso [22], Ma and Roters [23], Evers et al. [26], Ma et al. [24], Ma et al. [25], McDowell [66], Li et al. [57]
Martensite mechanics, phase transformation, shape memory	Marketz and Fischer [67], Marketz and Fischer [68], Tomita and Iwamoto [69], Diani et al. [70], Diani and Parks [71], Cherkaoui et al. [72], Cherkaoui et al. [73], Thamburaja and Anand [74], Tomita and Iwamoto [75], Govindjee and Miehe [76], Anand and Gurtin [77], Turteltaub and Suiker [78], Thamburaja [79], Lan et al. [80], Turteltaub and Suiker [81], Tjahjanto et al. [82], Geers and Kouznetsova [83]
In-grain texture, grain-scale mechanics, mesoscale, non-uniform deformation	Peirce et al. [27], Peirce et al. [84], Beaudoin et al. [85], Mika and Dawson [34], Sarma and Dawson [86], Sarma and Dawson [87], Sarma et al. [88], Forest [89], Bhattacharyya et al. [90], Raabe et al. [38], Miller and Turner [91], Raabe et al. [92], Sachtleber et al. [14], Kim and Oh [93], Clarke et al. [40], Choi [94], Zaefferer et al. [95], Eriean and Rey [96], Sarma and Radhakrishnan [97], Roters et al. [98], Kim et al. [99], Murphy et al. [46], daFonseca et al. [100], You et al. [101], Musienko et al. [102], Han and Dawson [103], Zhao et al. [32], Zhang et al. [104]
Texture evolution, texture stability, in-grain texture formation, anisotropy	Asaro and Needleman [105], Becker [106], Becker et al. [107], Bronkhorst et al. [108], Kalidindi et al. [109], Beaudoin et al. [110], Bertram et al. [111], Becker and Panchanadeeswaran [33], Beaudoin et al. [110], Mika and Dawson [112], Miehe et al. [113], Kalidindi [114], Balasubramanian and Anand [59], Van Houtte et al. [115], Delannay et al. [116], Raabe et al. [117], Bate and An [118], Raabe et al. [119], Li et al. [120], Sarma and Radhakrishnan [97], Anand [121], Roters et al. [122], Van Houtte et al. [123], Li et al. [124], Van Houtte et al. [125], Delannay et al. [126], Tang et al. [127], Tikhovskiy et al. [128], Lee et al. [129], Tikhovskiy et al. [130], Mayeur et al. [131], Delannay et al. [132]
Forming, deep drawing, process modeling, cup drawing, spring-back, earing, wire drawing, extrusion, anisotropy, design, fretting	Beaudoin et al. [133], Beaudoin et al. [134], Neale [135], Kalidindi and Schoenfeld [136], Nakamachi et al. [137], Zhao et al. [138], Xie and Nakamachi [139], Raabe et al. [1] Goh et al. [140], McGarry et al. [141], Raabe and Roters [142], Zhao et al. [13], Tugcu et al. [143], Delannay et al. [144], Li et al. [124], Raabe et al. [145], Dick and Cailletaud [146], Tikhovskiy et al. [128], Delannay et al. [126], Chen et al. [147], Raabe [148], Nakamachi et al. [149], Ocenasek et al. [150], Tikhovskiy et al. [130], Mayeur et al. [131], Li et al. [151], Li et al. [152], Zhuang et al. [153], Delannay et al. [132], Zamiri et al. [154]
Crystal plasticity and recrystallization	Bate [155], Raabe and Becker [156], Raabe [157], Radhakrishnan et al. [158], Raabe [159], Takaki et al. [160], Raabe [148], Semiatin et al. [161], Zambaldi et al. [162], Loge et al. [163]
Deformation twinning	Kalidindi [164], Staroselsky and Anand [165], Marketz et al. [166], Staroselsky and Anand [167], Marketz et al. [168], Salem et al. [169]
Nanoindentation, pillar testing, micro-bending, micro-scale deformation and testing	Wang et al. [170], Zaafarani et al. [171], You et al. [101], Raabe et al. [172], Casals et al. [173], Zaafarani et al. [174], Alcalá et al. [175], Weber et al. [176], Xu et al. [64], Demir et al. [177]
Numerical aspects, FE shape effects, mesh dependence, accuracy, robust integration methods, texture discretization	Miehe [178], Bachu and Kalidindi [179], Harewood and McHugh [180], Amirkhizi and Nemat-Nasser [181], Harewood and McHugh [182], Kuchnicki et al. [183], Melchior and Delannay [184], Zhao et al. [185], Li et al. [186], Ritz and Dawson [187], Barton et al. [188], Gerken and Dawson [52]
Damage, fatigue, cyclic loading, void growth	Bruzzi et al. [189], Turkmen et al. [190], Turkmen et al. [191], Kysar et al. [192], Sinha and Ghosh [193], Potirniche et al. [194], Zhang et al. [195], Cheong et al. [196], Dunne et al. [197], Liu et al. [198], Bieler et al. [199], Kumar et al. [200], Patil et al. [201], Watanabe et al. [202], McDowell [66], Mayama et al. [203], Borg et al. [56]
Multiphase mechanics	Hartig and Mecking [204], Tjahjanto et al. [205], Mayeur et al. [131], Inal et al. [206], Vogler and Clayton [207]

CPFE simulations can be used both at microscopic and macroscopic scales [1]. Examples for small-scale applications are inter- and intra-grain mechanics, damage initiation, mechanics at interfaces, simulation of micromechanical experiments (e.g. indentation, pillar compression, beam bending), or the prediction of local lattice curvatures and mechanical size effects (see Table 1). Consequently,

CPFE methods gain momentum for the field of small-scale material testing where the experimental boundary conditions are difficult to control and/or monitor. In such cases the experimental results may sometimes be hard to interpret without corresponding CPFE simulations that allow an experimentalist to simulate the effects of details in the contact and boundary conditions. Miniaturization also

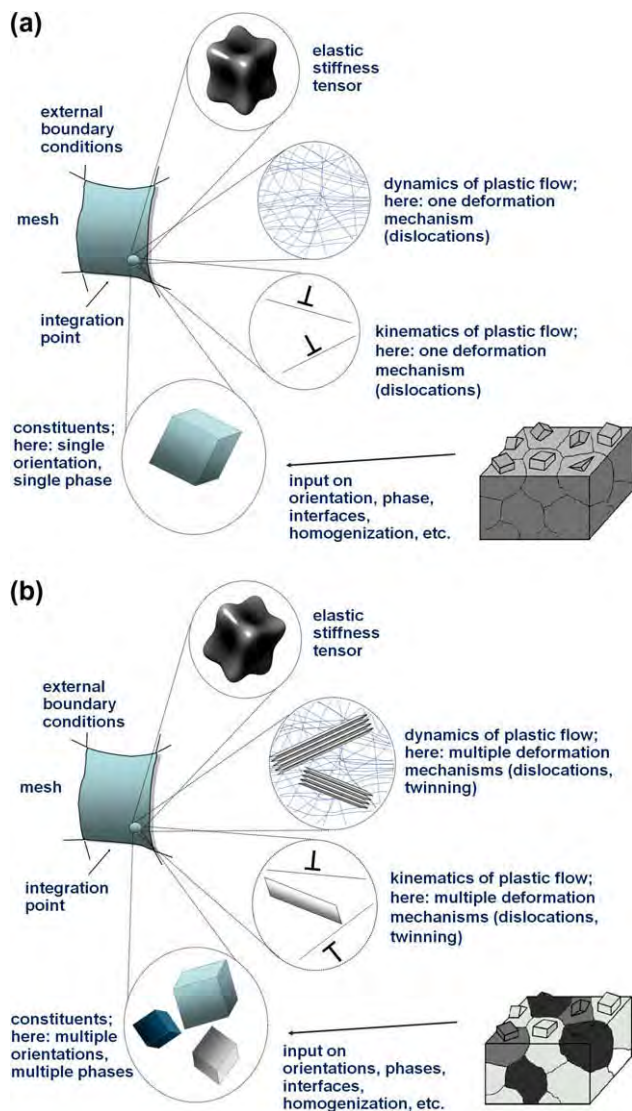


Fig. 4. Schematic presentation of the conceptual ingredients in CPFE simulations. (a) Example of a case with one type of deformation mechanism (lattice dislocations) and one phase. (b) Example of a case with different deformation mechanisms, phases, orientations and homogenization schemes at the same integration point.

occurs in engineering design. Many products nowadays have dimensions in the range of the grain scale, e.g. micro-electromechanical systems (MEMS), bonding wires and pillars, stents, and practically all materials in electronic components. Design of such parts increasingly requires consideration of grain-scale crystalline anisotropy. Some applications along these lines are discussed in Section 9.

Macroscopic applications of the CPFE method occur particularly in the fields of large-scale forming and texture simulations. These problems usually require appropriate homogenization schemes within a CPFE model since a larger number of crystals and/or phases must be considered in each representative volume element mapped at a FE integration point. Primary engineering objectives of CPFE applications in macroscopic forming simulations are the prediction of the precise material shape after forming,

thickness distribution, material failure, optimization of material flow, elastic spring-back, forming limits, texture evolution and the mechanical properties of the formed part [13,137–139,145,217]. Further related applications occur in tool design, press layout and surface properties (see references in Table 1). The latter aspect involves both macroscopic (e.g. wrinkling) as well as microstructural (e.g. roping, ridging, orange peel) mechanisms that influence the surface topography [15,28,29]. A recent development is the use of the CPFE method as a virtual mechanical laboratory. This approach uses crystal plasticity simulations instead of complicated mechanical tests that are required for fitting yield surface coefficients [217].

A further advantage of CPFE predictions is that they can be compared to experiments in a very detailed fashion probing a variety of quantities (Table 2). Corresponding studies compared shape changes, forces, strains, strain paths, rate effects, texture evolution, interface response, local stresses and size effects one-to-one at different scales (Table 2). Examples for applications and experimental validation procedures are given in Section 9.

Beyond these metallurgical and mechanical considerations numerical aspects also deserve attention. CPFE formulations can be either fully integrated into FE codes or implemented as user-defined subroutines into commercially available solvers. The latter point is important because engineering applications are often tackled using commercial platforms. The use of standard solvers also helps to make CPFE methods accessible to a broader community. Since details of the FE method, the mesh and the integration procedures also play a significant role in CPFE simulations, some of these aspects are discussed in Section 8.

In summary, this review intends to demonstrate that for micro- and macro-scale mechanical problems containing dyadic degrees of freedom for shear, the CPFE method is an effective modeling platform as it can deal with the delicate interplay of different effects such as complicated boundary conditions (e.g. imposed by the surrounding microstructure or by external fields), various deformation mechanisms and their interactions (e.g. dislocation mechanics at interfaces or twins and martensite), interface properties (e.g. structural superplasticity or the Hall–Petch effect) and details of slip localization (e.g. shear band formation) at reasonable computational costs and by using open source or commercial solvers.

## 2. Concise historical overview

The first FE simulation was performed by Courant in 1943 [218]. The breakthrough of the method came with the publication of “The Finite Element Method in Structural and Continuum Mechanics” by O.C. Zienkiewicz in 1967 [11]. The three succeeding volumes [12,219,220] are considered the most important monographs in the field to date.

Even though it has been known since 1934 [221–224] that crystalline materials deform plastically by the slip of dislocations on discrete slip systems, for a long time contin-



Table 2  
Examples of measurable quantities that can be predicted by CPFE models.

Prediction by CPFE methods	Experimental access
Surface roughening	Speckle interferometry, digital image correlation (photogrammetry), atomic force microscopy, white-light confocal microscopy
Elasticity, interface mechanics, grain size effects, grain interaction, size effects	Indentation testing, tensile and compression testing, mechanical tests at different sample sizes, digital image correlation, electron backscatter diffraction, scanning electron microscopy, ultrasonic testing, X-ray and synchrotron Bragg peak broadening and shifting
Creep, high temperature deformation, superplasticity	Tensile testing, texture measurement, in situ electron microscopy
Dislocation-based constitutive modeling	Flow stress measurement, transmission electron microscopy, lattice orientation measurements, electron channeling contrast imaging in the scanning electron microscope
Martensite mechanics, phase transformation, shape memory	Magnetic measurements, multiphase electron backscatter diffraction, X-ray and synchrotron Bragg diffraction
In-grain texture, grain-scale mechanics, non-uniform deformation, multiphase mechanics	Digital image correlation, indentation hardness testing, orientation determination (Kikuchi diffraction in the transmission or scanning electron microscope; X-ray Bragg diffraction), mechanical testing
Texture evolution, texture stability, in-grain texture formation, anisotropy	Texture measurements using Kikuchi diffraction in the transmission and scanning electron microscope or X-ray Bragg diffraction
Forming, deep drawing, process modeling, cup drawing, spring-back, earing, wire drawing, extrusion, anisotropy, design, fretting	Shape analysis, cup drawing experiments, spring-back measurements, ultrasonic measurement of elastic polycrystal constants
Crystal plasticity and recrystallization	Hardness testing, metallography, electrical resistivity, X-ray and synchrotron diffraction, electron backscatter diffraction, transmission electron microscopy, grain size determination, kernel average orientation determination, calorimetry
Deformation twinning	Metallography, X-ray and synchrotron diffraction, electron backscatter diffraction, transmission electron microscopy, electron channeling contrast imaging in the scanning electron microscope
Nanoindentation, micro-scale deformation, miniaturized mechanical testing	Hardness and stiffness analysis using nanoindenter or nanomanipulator tests, surface shape analysis using atomic force microscopy, electron microscopy

uum mechanical FE simulations used isotropic material models. The first CPFE simulations were performed by Peirce et al. in 1982 [27]. Due to computational restrictions they used a simplified set-up of two symmetric slip systems in order to study the tensile behavior of a single crystal. These simulations were later extended to a polycrystalline arrangement by Harren et al. [225,226] using a 2-D set-up with two or three slip systems. In 1991 Becker was the first to perform simulations on the basis of the 12 slip systems of a face-centered cubic (fcc) crystal. Using a 3-D model for the crystallographic degrees of freedom, he simulated channel–die deformation of a columnar polycrystal aggregate [106] and of a single crystal [107]. Since that time an ever-increasing number of CPFE simulations has been performed, enabled by the increase in computational power. In the field of direct or one-to-one crystal plasticity models numerous grain- and subgrain scale problems have been tackled using meshes with subgrain resolutions and, in part, complex 2-D and 3-D grain arrangements [14,32,34,86,88,110,179,185] (Section 9.2). On the macroscopic side, homogenization schemes were developed for the application of the CPFE method to large-scale forming operations. In this case the main problem was the correct representation of the (statistical) crystallographic texture of the material in the CPFE mesh. This can be achieved in different ways using, for example, texture components [138,142] or direct sampling of single orientations from the orientation distribution function (ODF) [184,227,228] (Sections 9.3 and 6.2).

All CPFE models mentioned so far used phenomenological constitutive equations (see Section 4.2) and considered dislocation slip as the only deformation mechanism. When applying the CPFE method in new areas such as small-scale deformation or interface mechanics existing phenomenological constitutive laws are often insufficient. Also, new classes of materials such as twinning-induced plasticity (TWIP) and transformation-induced plasticity (TRIP) steels or shape memory alloys show additional deformation and hardening mechanisms, i.e. twinning and/or deformation-induced phase transformations.

Size effects can be introduced into CPFE frameworks by using phenomenological strain gradient theories which were developed by Fleck et al. [229], Fleck and Hutchinson [230], and Nix and Gao [231]. However, as strain gradients can be associated with GNDs, new internal-variable constitutive formulations were developed that incorporate dislocation densities as physically based state variables [9,18,19,24,25,232] instead of strain measures, which were often used in phenomenological formulations (also see Section 4.3). This most recent class of constitutive models also allows one to incorporate additional metallurgical mechanisms such as grain boundary mechanics [25,233] (Section 4.3.3) or damage initiation [199] into the constitutive description. Concerning additional deformation mechanisms such as those that occur in TWIP or TRIP steels, extended CPFE formulations have been suggested by Kalidindi et al. [114,164], Salem et al. [169], Staroselskya and Anand [167] and Suiker and Turteltaub [234] (also see Section 5).

### 3. Flow kinematics

This section presents a detailed discussion of the different distortion measures that form the geometrical backbone of the CPFE framework. The review is given in terms of finite deformation measures as the small distortion case can always be derived from it. The kinematics of isothermal finite deformation describes the process where a body originally in a reference state (or “configuration”),  $\mathcal{B} \subset \mathbb{R}^3$ , is deformed to the current state,  $\mathcal{S} \subset \mathbb{R}^3$ , by a combination of externally applied forces and displacements over a period of time,  $\Delta t$ . In this treatment we choose the perfect single crystal as reference state. Other possible choices of a reference state would be the state just before deformation, or in an incremental formulation, the state at any time  $t$ . The latter has the disadvantage of a constantly changing reference state while the former might contain an undefined amount of crystal defects.

In crystal plasticity one has to distinguish three coordinate systems. The shape coordinate system is a curvilinear system, based on the physical shape of the body, which deforms congruently with the total changes in shape occurring during deformation. In contrast, the lattice coordinate system has coordinate axes fixed locally parallel to the crystallographic directions, i.e. the nodes of the coordinate network maintain a one-to-one correspondence with crystal lattice points during deformation except where singularities in the atomic array occur due to the defect cores. Therefore, the space defined by the deformed lattice coordinate system is connected to ordinary Euclidean space by functions that depend on the defect content and distribution [235]. The distinction between shape and lattice distortion is critical when internal stresses are to be calculated [236]. Since these stresses arise from internal reaction forces generated when atoms experience a relative displacement from their equilibrium positions, they can only be related to lattice deformations because shape deformations do not necessarily follow the deformation of the underlying crystal lattice. Deformations in the two types of coordinates are coincident only when no motion of crystal defects occurs, which is the usual assumption made for calculating elastic stresses from measurements of the small deformations of a coordinate system deposited on the surface or embedded within a body. Finally, it is often convenient to describe the deformations of the overall shape of a body and its associated lattice in terms of a third reference system, laboratory coordinates, that does not deform with the body. Computations of the deformation of both shape and lattice coordinate systems can be made in terms of their components in laboratory coordinates. This has the practical advantage of providing a reference system that is fixed throughout the deformation of the body.

To cast this in a formal way we represent the positions of neighboring material points relative to an arbitrary origin in the reference configuration by the vector  $\mathbf{dx}$ . As a result of deformation, this vector is mapped into its image in the current configuration,  $\mathbf{dy} = \mathbf{dx} + \mathbf{du}$ , where  $\mathbf{du}$  is the

differential total displacement vector. These vectors are related by the total, or shape, deformation gradient,  $\mathbf{F}$ :

$$\mathbf{dy} = \left( \frac{\partial \mathbf{y}}{\partial \mathbf{x}} \right) \mathbf{dx} = \left( \mathbf{I} + \frac{\partial \mathbf{u}}{\partial \mathbf{x}} \right) \mathbf{dx} = \mathbf{F} \mathbf{dx} \quad (1)$$

where  $\mathbf{I}$  is the second rank identity tensor. The second rank tensor formed from the partial derivatives of  $\mathbf{u}$  with respect to  $\mathbf{x}$  is known as the shape (also total) distortion tensor,  $\boldsymbol{\beta}$  and is a perfect differential if the deformations that produce it do not introduce any discontinuities, i.e. gaps or cleavages, in the global body. That is, there exists a one-to-one mapping of material points from the current state to the reference state. The Lagrangian and Eulerian (Almansi) finite strain tensors,  $\mathbf{E}$  and  $\mathbf{E}^*$ , associated with a deformation (defined by the deformation gradient  $\mathbf{F}$ ), respectively, are symmetric tensors defined by:

$$\mathbf{E} = \frac{1}{2} (\mathbf{F}^T \mathbf{F} - \mathbf{I}) \quad (2)$$

and

$$\mathbf{E}^* = \frac{1}{2} (\mathbf{I} - \mathbf{F}^{-T} \mathbf{F}^{-1}) \quad (3)$$

where the superscript (T and  $-T$ ) indicates the transpose and its inverse, respectively, and the superscript ( $-1$ ) indicates the inverse of the tensor. It is useful to note that any deformation gradient,  $\mathbf{F}$ , can be expressed as the product of a pure rotation,  $\mathbf{R}$ , and a symmetric tensor that is a measure of pure stretching. Two representations are possible, depending on which operation occurs first:

$$\mathbf{F} = \mathbf{R} \mathbf{U} = \mathbf{V} \mathbf{R} \quad (4)$$

where the symmetric tensors  $\mathbf{U}$  and  $\mathbf{V}$  are, respectively, the right and left stretch tensors.

The shape deformation can be decomposed into two components [7,211,213,237,238] (see also Fig. 5):

$$\mathbf{F} = \mathbf{F}_e \mathbf{F}_p. \quad (5)$$

The “elastic” deformation,  $\mathbf{F}_e$ , is the deformation component due to the reversible response of the lattice to external loads and displacements (as well as rigid-body rotations) while the “plastic” deformation,  $\mathbf{F}_p$ , is an irreversible permanent deformation that persists when all external forces and displacements that produce the deformation are removed. In this sense, transformation of the reference state

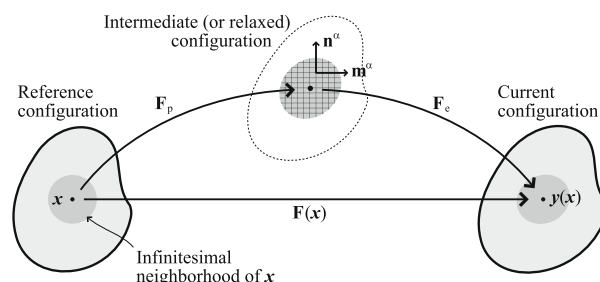


Fig. 5. Decomposition of the total deformation gradient,  $\mathbf{F} = \mathbf{F}_e \mathbf{F}_p$ .



by  $\mathbf{F}_p$  leads to an intermediate configuration which is free from external stresses and which is generally considered to maintain a perfect lattice. However, this state requires that none of the dislocations which produced the permanent shape change any longer reside within the material point neighborhood, but are located at its periphery. In reality, this assumption is typically not fulfilled, such that (balanced) internal stresses remain due to the (homogeneous) presence of dislocations within the neighborhood.

This decomposition differs from that proposed by Bilby et al. [239] in that their model requires that the stress-free deformation producing the intermediate state does not leave residual deformation in the lattice, hence does not change the thermodynamic state of the material. In their formulation, no residual dislocations are present in the intermediate state regardless of the vanishing of the net Burgers vector. Making this distinction, Bilby et al. [239] refer to  $\mathbf{F}_p$  as the “dislocation deformation” and  $\mathbf{F}_e$  as “lattice correspondence functions”. In this case  $\mathbf{F}_e$  also contains a component of lattice deformation due to sources of internal stress distributed throughout the body.

For example, consider the processes shown in Figs. 6 and 7 by which an initially perfect crystal undergoes the same change in shape by shear, though involving different contributions from dislocation slip. In Fig. 6 the crystal lattice is unchanged in the reference and current states, so all the work expended in the process is dissipated as heat and the material remains in the same thermodynamic state before and after the deformation. At the end of the process the external loads can be removed and no lattice deformation remains,  $\mathbf{F} = \mathbf{F}_p$ . In contrast, the crystal undergoes an purely elastic shape change in Fig. 7. In this

case there are no dislocations, the lattice is distorted congruently with the external shape of the body,  $\mathbf{F} = \mathbf{F}_e$ , and the external cause for the deformation must be maintained in order to preserve the change in shape; removal of the external boundary conditions causes the body to revert to the reference state. Also the thermodynamic states of the reference and current states are different because of the stored elastic energy due to the lattice deformation.

As for the total shape deformation,  $\mathbf{F}$ , given in Eq. (1), the elastic and plastic deformations can each be expressed as sums of the identity tensor and second-rank tensors,  $\beta_e$  and  $\beta_p$ , called the elastic distortion and plastic distortion, respectively. However these quantities need not be integrable derivatives of displacement vectors for the elastic and plastic deformations, since displacements associated with these deformations can be incompatible, i.e. may introduce discontinuities into the body.

When dislocation deformation occurs by slip on two or more systems, the spatiotemporal order in which deformation occurs seems important in the kinematic treatment. For example, Fig. 8 illustrates that a pure dislocation deformation of a volume element by slip on two-slip systems that lead to the same  $\mathbf{F}_p$  results in a different configuration of the reference volume. In Fig. 8a dislocation deformation initially causes the deformation component  $\mathbf{F}_{p21}$ , followed by  $\mathbf{F}_{p12}$ , resulting in a state of pure shear. In Fig. 8b the same final state is reached by reversing the order of the dislocation deformation. The resulting surface configuration of extra half planes results in two different types of surface dislocation configuration upon subsequent insertion into the original body. Denoting the dislocation deformation due to the  $k$ th slip event as  $\mathbf{F}_p^{(k)}$ , the appropriate expression for the multiplicative decomposition of  $n$  successive events is:

$$\mathbf{F} = \mathbf{F}_e \left( \mathbf{F}_p^{(n)} \mathbf{F}_p^{(n-1)} \dots \mathbf{F}_p^{(1)} \right). \quad (6)$$

In Eq. (6) the index refers to the order in which the slip event occurs. Different index values can apply to slip on the same system occurring with intervening deformation on other systems.

However, the distinction between different orders is generally not important, since the deformation carried by individual slip events is small unless atomic dimensions are concerned. This can be illustrated by expanding the plastic distortion into its components on the active slip systems:

$$\begin{aligned} \mathbf{F}_p &= \mathbf{F}_p^{(n)} \mathbf{F}_p^{(n-1)} \dots \mathbf{F}_p^{(1)} \\ &= \mathbf{I} + \sum_{k=1}^n \beta_p^{(k)} + \mathcal{O}(\beta_p^2) + \mathcal{O}(\beta_p^3) + \dots, \end{aligned} \quad (7)$$

where the trailing terms on the right-hand side refers to terms of order higher than 1. Since all components are small in the usual sense of linear approximations, these higher-order terms can be neglected, leaving only the sum of first-order terms in  $\beta_p^{(k)}$ . This sum of linear terms can

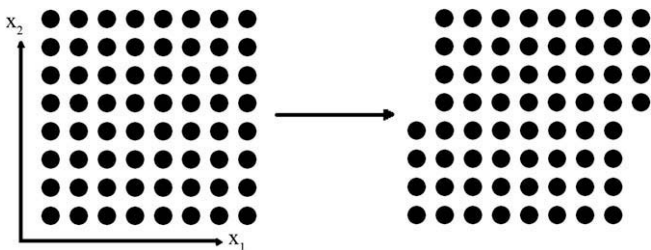


Fig. 6. Example of pure dislocation deformation,  $\mathbf{F} = \mathbf{F}_p$ .

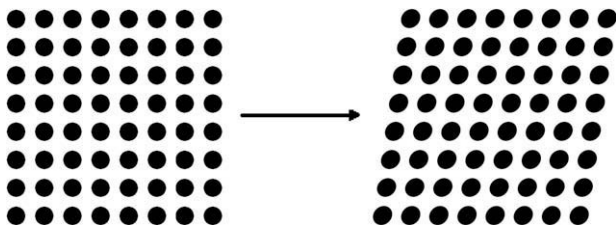


Fig. 7. Example of pure lattice deformation,  $\mathbf{F} = \mathbf{F}_e$ .

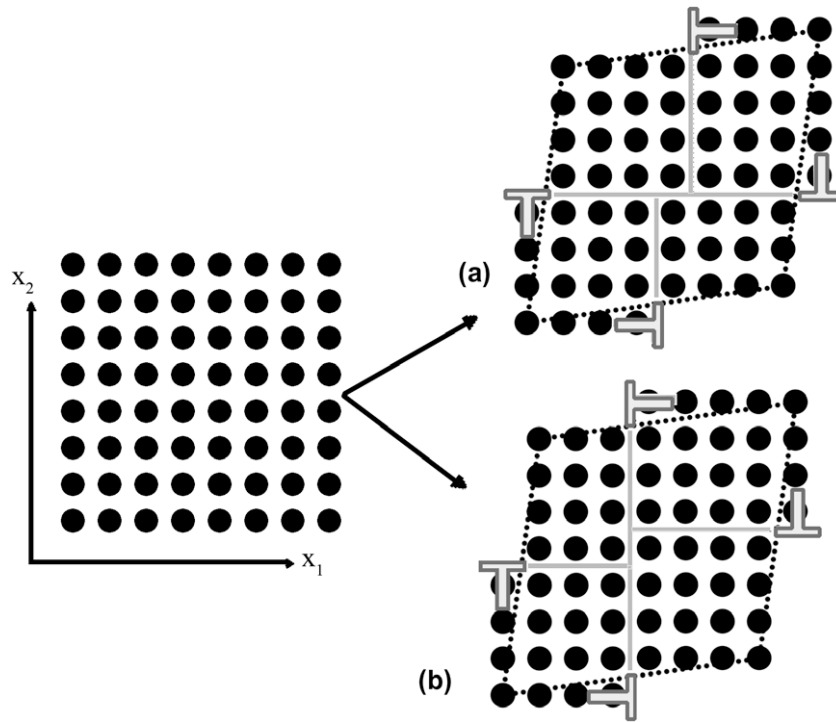


Fig. 8. When dislocation deformation occurs by slip on two or more systems, the order in which deformation occurs makes a difference in the kinematic treatment. The figure illustrates that a pure dislocation deformation of a volume element by slip on two slip systems that results in the same  $\mathbf{F}_p$  results in a different configuration of the reference volume. A dislocation deformation initially causes the deformation component  $\mathbf{F}_{p21}$ , followed by  $\mathbf{F}_{p12}$ , resulting in a state of pure shear. The same final state is reached by reversing the order of the dislocation deformation. The resulting surface configuration of extra half planes results in two different types of surface dislocation configuration upon subsequent insertion into the original body.

be rearranged to group the summands according to slip system, leading to an expression for  $\mathbf{F}_p$  that contains terms from all active slip systems regardless of the order in which slip on each occurs.

Development of the kinematics of finite deformations requires an expression for the time rate of change of  $\mathbf{F}$ . The velocity of each material point of a body in motion forms a vector field measured in the current state,  $\mathbf{v} = \dot{\mathbf{u}}$ , where the superimposed dot refers to the time derivative of the quantity. The spatial gradient of the total velocity,  $\mathbf{L}$ , is defined as:

$$\mathbf{L} = \mathbf{v} \otimes \nabla_{\mathbf{y}} = \dot{\mathbf{F}}\mathbf{F}^{-1}, \quad (8)$$

where the index,  $\mathbf{y}$ , of the gradient operator refers to the fact that it is evaluated at the current location of the material point. The relationship of  $\mathbf{L}$  to  $\mathbf{L}_e$  and  $\mathbf{L}_p$  can be obtained by combining Eqs. (5) and (8). Application of the product rule of differentiation to the former gives:

$$\dot{\mathbf{F}} = \dot{\mathbf{F}}_e\mathbf{F}_p + \mathbf{F}_e\dot{\mathbf{F}}_p, \quad (9)$$

which, when applied to Eq. (8), yields the velocity gradient:

$$\mathbf{L} = \dot{\mathbf{F}}_e\mathbf{F}_e^{-1} + \mathbf{F}_e\left(\dot{\mathbf{F}}_p\mathbf{F}_p^{-1}\right)\mathbf{F}_e^{-1} = \mathbf{L}_e + \mathbf{F}_e\mathbf{L}_p\mathbf{F}_e^{-1} \quad (10)$$

The term in parentheses in Eq. (10) is the plastic velocity gradient, which is evaluated in the intermediate configuration and must therefore be mapped into the deformed configuration by  $\mathbf{F}_e$ .

## 4. Constitutive models

### 4.1. Introduction

The preceding section on kinematics discussed the multiplicative decomposition of the deformation gradient  $\mathbf{F}$ :

$$\mathbf{F} = \mathbf{F}_e\mathbf{F}_p. \quad (11)$$

As shown there the plastic deformation evolves as:

$$\dot{\mathbf{F}}_p = \mathbf{L}_p\mathbf{F}_p \quad (12)$$

and in case of dislocation slip as the only deformation process, according to Eq. (7) and using first-order terms only,  $\mathbf{L}_p$  can be formulated as sum of the shear rates on all slip systems:

$$\mathbf{L}_p = \sum_{\alpha=1}^n \dot{\gamma}^{\alpha} \mathbf{m}^{\alpha} \otimes \mathbf{n}^{\alpha} \quad (13)$$

where vectors  $\mathbf{m}^{\alpha}$  and  $\mathbf{n}^{\alpha}$  are, respectively, unit vectors describing the slip direction and the normal to the slip plane of the slip system  $\alpha$ ;  $\dot{\gamma}^{\alpha}$  is the shear rate on that same system.  $n$  is the number of (active) slip systems.

This section is about the constitutive equations that define these shear rates as a function of the external stress,  $\boldsymbol{\sigma}$ , and the microstructural state of the material,  $S$ . In other words the kinematic formalism describes the geometrical aspects of the anisotropy of crystal mechanics without considering

stresses, while the constitutive equations capture the physics of the material behavior, in particular of the dynamics of those lattice defects that act as the elementary carriers of plastic shear. How the microstructural state of the material,  $S$ , is defined and how it evolves during loading depends on the kind of constitutive model used. In the following we present two classes of constitutive models, namely phenomenological models and physics-based models.

#### 4.2. Phenomenological constitutive models

Phenomenological constitutive models mostly use a critical resolved shear stress,  $\tau_c^\alpha$ , as state variable for each slip system  $\alpha$ . Therefore, the shear rate,  $\dot{\gamma}^\alpha$ , is formulated as a function of the resolved shear stress,  $\tau^\alpha = 0.5 \mathbb{C} [\mathbf{F}_c^T \mathbf{F}_c - \mathbf{I}] : \mathbf{m}^\alpha \otimes \mathbf{n}^\alpha$ , and that critical resolved shear stress:

$$\dot{\gamma}^\alpha = f(\tau^\alpha, \tau_c^\alpha) \quad (14)$$

and the evolution of the material state is formulated as function of the total shear,  $\gamma$ , and the shear rate,  $\dot{\gamma}^\alpha$ :

$$\tau_c^\alpha = g(\gamma, \dot{\gamma}^\alpha) \quad (15)$$

Prominent formulations along these lines were suggested by Rice et al. [16], Hutchinson [240], Peirce et al. [27,84] for fcc metallic crystals. In this framework the kinetic law on a slip system  $\alpha$  is:

$$\dot{\gamma}^\alpha = \dot{\gamma}_0 \left| \frac{\tau^\alpha}{\tau_c^\alpha} \right|^{\frac{1}{m}} \text{sgn}(\tau^\alpha) \quad (16)$$

where  $\dot{\gamma}^\alpha$  is the shear rate on slip system  $\alpha$  subjected to the resolved shear stress  $\tau^\alpha$  at a slip resistance  $\tau_c^\alpha$ ;  $\dot{\gamma}_0$  and  $m$  are material parameters that determine the reference shear rate and the rate sensitivity of slip, respectively. The influence of any set of slip system, index  $\beta$ , on the hardening behavior of a (fixed) slip system  $\alpha$  is given by:

$$\dot{\tau}_c^\alpha = \sum_{\beta=1}^n h_{\alpha\beta} |\dot{\gamma}^\beta| \quad (17)$$

where  $h_{\alpha\beta}$  is referred to as the hardening matrix:

$$h_{\alpha\beta} = q_{\alpha\beta} \left[ h_0 \left( 1 - \frac{\tau_c^\beta}{\tau_s} \right)^a \right] \quad (18)$$

which empirically captures the micromechanical interaction among different slip systems. In this formulation  $h_0$ ,  $a$  and  $\tau_s$  are slip hardening parameters, which are assumed to be identical for all fcc slip systems owing to the underlying characteristic dislocation reactions. The parameter  $q_{\alpha\beta}$  is a measure for latent hardening; its value is taken as 1.0 for coplanar slip systems  $\alpha$  and  $\beta$ , and 1.4 otherwise, which renders the hardening model anisotropic. In the literature a number of variations of Eqs. (16) and (17) can be found. Some authors [106] use the sinh function instead of a power-law in Eq. (16), while others [88] use modified hardening laws such as a generalized Voce equation [241,242] instead of Eq. (17).

These types of kinetic formulations are currently the most frequently used ones in CPFEE models although they

suffer from the drawback that the material state is only described in terms of the critical resolved shear stress,  $\tau_c$ , and not in terms of lattice defect populations [243,244]. The latter approach, however, is required to render crystal plasticity models path- and size-dependent as will be discussed in the following.

#### 4.3. Physics-based constitutive models

In contrast to the phenomenological constitutive models, the physically based ones rely on internal variables. In the case of plasticity the most important microstructural state variable certainly is the dislocation density as the dislocations are the carriers of plastic deformation.<sup>2</sup> Models that treat the evolution of dislocation densities and calculate the flow stress from them have been proposed by various authors [9,19,22,24,25,232]. In the following subsections we present the dislocation-based model by Ma et al. [23–25] in more detail. It should be noted that even though the dislocations are the most important internal variable measure, more parameters are required for a full characterization of the microstructure, e.g. grain size and shape, second phase fractions, precipitate morphology, etc. However, only a few of these additional parameters have been introduced into dislocation-based CPFEE models so far.

##### 4.3.1. Dislocation-based constitutive laws in CPFEE models

The dislocation density-based constitutive model introduced by Ma et al. [23–25] uses mobile dislocations,  $\rho_m^\alpha$ , gliding along the slip system  $\alpha$  to accommodate a part of the external plastic deformation. In order to do so they must overcome the stress field of the parallel dislocations,  $\rho_p^\alpha$ , which causes the passing stress. In addition, they must cut the forest dislocations,  $\rho_F^\alpha$ , with the aid of thermal activation. In this framework we define the parallel dislocation density,  $\rho_p^\alpha$ , and the forest dislocation density,  $\rho_F^\alpha$ , for each slip system  $\alpha$  in the following way:  $\rho_p^\alpha$  are the dislocations parallel to the slip plane, and  $\rho_F^\alpha$  are the dislocations perpendicular to the slip plane. Considering the immobile dislocation density,  $\rho_{SSD}^\alpha$  for fcc crystals, the following projections can be used:

$$\rho_F^\alpha = \sum_{\beta=1}^N \chi^{\alpha\beta} \rho_{SSD}^\beta |\cos(\mathbf{n}^\alpha, \mathbf{t}^\beta)| \quad (19)$$

$$\rho_p^\alpha = \sum_{\beta=1}^N \chi^{\alpha\beta} \rho_{SSD}^\beta |\sin(\mathbf{n}^\alpha, \mathbf{t}^\beta)|. \quad (20)$$

In these equations we introduce the interaction strength,  $\chi^{\alpha\beta}$ , between different slip systems, which includes the self-interaction strength, coplanar interaction strength,

<sup>2</sup> It should be noted that in some models dislocation densities are calculated by using the Taylor relation ( $\tau \propto \sqrt{\rho}$ ). These approaches must also be regarded as phenomenological models as they do not treat the evolution of the dislocation densities explicitly.



cross-slip strength, glissile junction strength, Hirth lock strength, and Lomer–Cottrell lock strength. In this formulation only edge dislocations are considered owing to their limited out-of-plane mobility. Their line direction is denoted by  $\mathbf{t}^\beta$ .

In a dislocation-based model the Orowan equation typically serves as kinetic equation instead of Eq. (16) as it couples shear rates to mobile dislocations, i.e. it allows one to translate a continuum mechanical term into the physics of dislocations

$$\dot{\gamma}^\alpha = \rho_m^\alpha b v^\alpha \quad (21)$$

where  $\rho_m$  is the density of mobile dislocations,  $b$  the magnitude of the Burgers vector and  $v$  the average velocity of the mobile dislocations. According to [23] the mobile dislocation density can be calculated from the statistically stored dislocation density by a simple scaling law:

$$\rho_m^\alpha = B T \sqrt{\rho_P^\alpha \rho_F^\alpha} \quad (22)$$

where  $T$  is the absolute temperature and  $B$  is given by:

$$B = \frac{2k_B}{c_1 c_2 c_3 G b^3}, \quad (23)$$

where  $k_B$  is the Boltzmann constant and  $G$  the shear modulus;  $c_1$  to  $c_3$  are constants introduced in the dislocation density evolution laws below.

Under the assumption of forest cutting as the rate-determining process, the velocity of the mobile dislocations can be calculated as:

$$v^\alpha = \lambda^\alpha v_{\text{attack}} \exp\left(-\frac{Q_{\text{slip}}}{k_B T}\right) \sinh\left(\frac{\tau_{\text{eff}}^\alpha V^\alpha}{k_B T}\right) \text{sgn}(\tau^\alpha) \quad (24)$$

where  $\lambda^\alpha$  is the jump width which is inversely proportional to the forest dislocation spacing,  $v_{\text{attack}}$  is the attack frequency,  $Q_{\text{slip}}$  is the effective activation energy for dislocation glide, and  $V^\alpha$  the activation volume, which can be calculated as:

$$V^\alpha = c_3 \lambda^\alpha b^2 \quad (25)$$

with  $c_3$  being a fitting constant of order unity.

Finally, the effective shear stress  $\tau_{\text{eff}}^\alpha$  can be calculated from the resolved shear stress and the passing stress as:

$$\tau_{\text{eff}}^\alpha = \begin{cases} |\tau^\alpha| - \tau_{\text{pass}}^\alpha = |\tau^\alpha| - c_1 G b \sqrt{\rho_P^\alpha + \rho_m^\alpha} & \text{for } |\tau^\alpha| > \tau_{\text{pass}}^\alpha \\ 0 & \text{for } |\tau^\alpha| \leq \tau_{\text{pass}}^\alpha \end{cases} \quad (26)$$

The phenomenological description of hardening in Eq. (17) is substituted by the evolution of the dislocation densities. For this purpose rate equations are formulated based on individual dislocation reactions. In Ref. [23] four such processes are taken into account, namely lock and dipole formation as processes increasing the dislocation density, and both athermal and thermally activated annihilation as recovery processes. Detailed derivations of these rate equations can be found in Ref. [23]. In the following we summarize the results:

- Lock formation

$$\dot{\rho}_{\text{SSD}}^{\alpha+} = \frac{c_4}{b} \sqrt{\rho_F^\alpha} \dot{\gamma}^\alpha \quad (27)$$

- Dipole formation

$$\dot{\rho}_{\text{SSD}}^{\alpha+} = \frac{c_5}{b} d_{\text{dipole}}^\alpha \rho_m^\alpha \dot{\gamma}^\alpha \quad (28)$$

$$d_{\text{dipole}}^\alpha = \frac{\sqrt{3} G b}{16\pi(1-\nu)} \left(|\tau^\alpha| - \tau_{\text{pass}}^\alpha\right)^{-1} \quad (29)$$

- Athermal annihilation

$$\dot{\rho}_{\text{SSD}}^{\alpha-} = -c_6 \rho_{\text{SSD}}^\alpha \dot{\gamma}^\alpha \quad (30)$$

- Thermal annihilation due to climb of edge dislocations

$$\dot{\rho}_{\text{SSD}}^{\alpha-} = -c_7 \frac{D_0 b^3}{k_B T} \exp\left(-\frac{Q_{\text{bulk}}}{k_B T}\right) \rho_{\text{SSD}}^{\alpha 2} |\tau^\alpha| \left(\frac{\dot{\gamma}^\alpha}{\dot{\gamma}_{\text{ref}}}\right)^{c_8} \quad (31)$$

where  $c_4, \dots, c_8$  are fitting constants,  $d_{\text{dipole}}$  the critical distance for dipole formation,  $D_0$  the diffusion coefficient,  $Q_{\text{bulk}}$  the activation energy for dislocation climb and  $\dot{\gamma}_{\text{ref}}$  a reference shear rate.

#### 4.3.2. Introduction of geometrically necessary dislocations

Most of the constitutive laws reported in the literature can be attributed to the group of local models in which the total deformation gradient has been multiplicatively decomposed into elastic and plastic parts, and where the constitutive behavior can be fully described from the loading history. For stress–strain curves and texture predictions of polycrystals, local models have been shown to be powerful and efficient [108]. However, when the simulation scale becomes smaller such as in studies focusing on nanoindentation [170,171,174], micropillar compression [172], or small-scale beam bending [176], local models can be insufficient due to their inability to describe mechanical size effects.

The grain size dependence of the flow stress was first described by Hall and Petch by an empirical equation [245,246]. Numerous studies have since then shown that the strengthening effect by a smaller grain size is due to a higher volume fraction of heterogeneous plastic deformation in the vicinity of grain boundaries. There are several explanations in the literature based on dislocation mechanisms such as pile-ups of mobile dislocations in front of the grain boundaries causing stress concentrations that increase the slip resistance or strain gradients near those interfaces. These strain gradients are assumed to produce an extra increment of dislocation densities which increase the slip resistance [20]. Beyond the grain size effect different types of micro-scale experiments (torsion, bending, indentation) have also revealed a length-scale dependence of the flow stress [232]. In these experiments typically non-uniform plastic deformation occurs which may lead to orientation and strain gradients in the vicinity of a material point. These gradients can be associated with GNDs [212]. In phenomenological models it is not straightforward

how to integrate GNDs into the constitutive model. In contrast, in dislocation density-based models GND concepts can be easily integrated as part of the constitutive framework [210].

However, the calculation of strain gradients renders a constitutive model non-local, which makes it more difficult to implement. The main reason for this is that in a non-local model a material point is strongly coupled with its neighboring points during the evolution of GNDs. This means that strain gradient calculations have to converge for a set of neighboring material points in the same time increment. In order to achieve this some authors [9,26] use the divergence theorem for formulating new differential equations using GNDs and SSDs as additional degrees of freedom for every node in an element. These algorithms require supplying additional boundary conditions for the dislocation density flux. While this is not complicated for simple calculations, it is difficult for complex load cases. An alternative and more general integration algorithm was therefore introduced by Ma et al. [24] to solve any non-local constitutive model in material subroutines such as offered by commercial finite-element solvers (e.g. Marc, Abaqus).

This section shows how GNDs can be introduced in the dislocation model presented above. As mentioned above, Nye's dislocation tensor [210] can be used to translate the strain gradient into GNDs:

$$\mathbf{\Lambda} = -\frac{1}{b} \left( \nabla_{\mathbf{x}} \times \mathbf{F}_p^T \right)^T \quad (32)$$

where the nabla operator  $\nabla_{\mathbf{x}}$  is defined as the derivative with respect to the reference coordinate  $\nabla_{\mathbf{x}} = \partial/\partial\mathbf{x}$ . Using Eq. (32), the resultant Burgers vector for an arbitrary oriented surface can be calculated. In general this tensor is non-symmetric with nine independent values. Therefore, the calculation of the exact GND content for every slip system requires additional assumptions as although there are 12 slip systems for the fcc crystal structure only 6 of them are geometrically independent [247].

Using the material time derivative of Eq. (32) in conjunction with Eqs. (12) and (13), the change of the GND density can be derived [24]:

$$\dot{\rho}_{\text{GND}}^{\alpha} = \frac{1}{b} \left\| \nabla_{\mathbf{x}} \times \left( \dot{\gamma}^{\alpha} \mathbf{F}_p^T \mathbf{n}^{\alpha} \right) \right\| \quad (33)$$

The integration of the GNDs into the constitutive model is now simply a matter of extending the projection into forest and parallel dislocations (Eqs. (19) and (20)). To render this projection more convenient  $\dot{\rho}_{\text{GND}}^{\alpha}$  is decomposed into three groups: one group of screw dislocations with tangent vector parallel to the slip direction  $\mathbf{d}^{\alpha}$ , the other two groups of edge dislocations with tangent vectors parallel to  $\mathbf{n}^{\alpha}$  and  $\mathbf{t}^{\alpha}$ , respectively

$$\dot{\rho}_{\text{GNDs}}^{\alpha} = \frac{1}{b} \left[ \nabla_{\mathbf{x}} \times \left( \dot{\gamma}^{\alpha} \mathbf{F}_p^T \mathbf{n}^{\alpha} \right) \right] \cdot \mathbf{d}^{\alpha} \quad (34)$$

$$\dot{\rho}_{\text{GNDet}}^{\alpha} = \frac{1}{b} \left[ \nabla_{\mathbf{x}} \times \left( \dot{\gamma}^{\alpha} \mathbf{F}_p^T \mathbf{n}^{\alpha} \right) \right] \cdot \mathbf{t}^{\alpha} \quad (35)$$

$$\dot{\rho}_{\text{GNDen}}^{\alpha} = \frac{1}{b} \left[ \nabla_{\mathbf{x}} \times \left( \dot{\gamma}^{\alpha} \mathbf{F}_p^T \mathbf{n}^{\alpha} \right) \right] \cdot \mathbf{n}^{\alpha} \quad (36)$$

which satisfy

$$\left( \dot{\rho}_{\text{GND}}^{\alpha} \right)^2 = \left( \dot{\rho}_{\text{GNDs}}^{\alpha} \right)^2 + \left( \dot{\rho}_{\text{GNDet}}^{\alpha} \right)^2 + \left( \dot{\rho}_{\text{GNDen}}^{\alpha} \right)^2. \quad (37)$$

Eqs. (34)–(36) are a set of evolution equations for  $\rho_{\text{GND}}$ , just like those for  $\rho_{\text{SSD}}$  derived in the previous section. Finally the extended projection reads:

$$\rho_F^{\alpha} = \sum_{\beta=1}^N \chi^{\alpha\beta} \left[ \rho_{\text{SSD}}^{\beta} |\cos(\mathbf{n}^{\alpha}, \mathbf{t}^{\beta})| + |\rho_{\text{GNDs}}^{\beta} \cos(\mathbf{n}^{\alpha}, \mathbf{d}^{\beta})| + |\rho_{\text{GNDet}}^{\beta} \cos(\mathbf{n}^{\alpha}, \mathbf{t}^{\beta})| + |\rho_{\text{GNDen}}^{\beta} \cos(\mathbf{n}^{\alpha}, \mathbf{n}^{\beta})| \right] \quad (38)$$

$$\rho_P^{\alpha} = \sum_{\beta=1}^N \chi^{\alpha\beta} \left[ \rho_{\text{SSD}}^{\beta} |\sin(\mathbf{n}^{\alpha}, \mathbf{t}^{\beta})| + |\rho_{\text{GNDs}}^{\beta} \sin(\mathbf{n}^{\alpha}, \mathbf{d}^{\beta})| + |\rho_{\text{GNDet}}^{\beta} \sin(\mathbf{n}^{\alpha}, \mathbf{t}^{\beta})| + |\rho_{\text{GNDen}}^{\beta} \sin(\mathbf{n}^{\alpha}, \mathbf{n}^{\beta})| \right] \quad (39)$$

where absolute values of GNDs are used, so that the signs of their Burgers vectors are neglected. A direct result of this treatment is that no kinematic hardening can be predicted, which is acceptable for single-phase material and unidirectional loading.

#### 4.3.3. Interface models

Grain boundaries act as obstacles to dislocation motion. At the onset of plastic deformation of polycrystals, mobile dislocations are first created on the slip system with the largest local resolved shear stress in the grain with the most favorable orientation. When encountering a grain boundary these mobile dislocations accumulate in front of that interface. Such events lead to stress concentrations at the interface that add to the external stress field at this material point. These microplastic effects, where the local arrangement of dislocations determines the local stress, cannot be treated one-to-one in a crystal plasticity continuum mechanical framework because such models map the underlying dislocation mechanics in a phenomenological statistical or even empirical form. However, homogenization is admissible at larger plastic strains where most of the slip activation processes can be captured by long-range stresses rather than by local ones [249]. This means that the dislocation mechanics can, beyond the microplastic regime, be homogenized in the form of statistical dislocation populations, which in turn can be embedded as constitutive rate equations in a crystal plasticity theory [19,20,25].

Two approaches for including grain boundary mechanics into dislocation-based constitutive CPFE models can be found in the literature. In the first type of models the grain boundaries are treated as being partially transparent to dislocations [25]. In the second type of models interfaces appear as perfect obstacles that do not allow dislocation penetration events [21]. The latter assumption can be implemented in FE simulations as an additional set of boundary conditions, namely as a zero shear condition perpendicular to interfaces. While the latter approach appears to be relatively straightforward at first view it can be rather

intricate when meshing complicated grain aggregates [14,38,85,95]. As shown by Evers et al. [21] these additional boundary conditions result in an increased hardening of the material, however, they do not result in an increase of the initial yield stress, i.e. the Hall–Petch effect is not captured. In order to overcome this drawback Evers et al. [21] suggested introducing grain boundary dislocations (GBDs) as an initial content of GNDs at the position of the grain boundaries. These GBDs are calculated by Evers et al. [21] from the crystallographic misorientation across the interface in the following way: When considering two crystals with orientations  $\mathbf{Q}_I$  and  $\mathbf{Q}_{II}$  with slip systems  $(\mathbf{d}^{\alpha,\beta}, \mathbf{t}^{\alpha,\beta}, \mathbf{n}^{\alpha,\beta})$ ,  $\alpha, \beta = 1, 2, \dots, 12$ ,<sup>3</sup> and a grain boundary with a normal vector  $\mathbf{n}_{GB}$ , which separates these two crystals (Fig. 9), one obtains the density of GBDs as:

$$\rho_{GBD}^{\alpha} = \text{sign}(\mathbf{n}_0^{\alpha} \cdot \mathbf{n}_{GB0}) \frac{(|\mathbf{n}^{\alpha} \cdot \mathbf{n}_{GB}| - |\mathbf{n}^{\beta} \cdot \mathbf{n}_{GB}|)^2}{b^2} \quad (40)$$

The slip system  $\beta$  has to be chosen to minimize  $\rho_{GBD}^{\alpha}$ .

In the second type of approach Ma et al. [25] assume partial transparency of the interface to dislocations. The transmission probability of incoming mobile dislocations to penetrate a grain boundary can be treated in terms of an activation concept. The enthalpy for this activation process stems from the elastic energy that is required for the formation of misfit dislocations which remain as debris in the interface upon slip penetration. This activation enthalpy enters as an additional contribution into the activation term for the slip of mobile dislocations (Eq. (24)). It is likely that each transmission event will occur at the smallest possible energy consumption. This condition provides a selection criterion for the slip systems involved. The main task in this model, therefore, consists in identifying the outbound slip system on the other side of the boundary, which provides the closest geometrical match to the inbound slip system. The smallest misalignment between the active inbound and the expected outbound slip systems leads to the smallest possible energy barrier.<sup>4</sup> For an arbitrary transmission event, it is obvious that some incoming slip system does not, as a rule, match a corresponding one on the outbound side exactly, i.e. the shear is usually not coherent on the two sides of a grain boundary. Therefore, in order to meet the conservation of the lattice defect vector sum when crossing an interface, misfit dislocations will be created in the grain boundary. The additional energy required to produce such an extra misfit dislocation acts as an energy barrier for the thermally activated slip transmission event. This barrier, hence, acts as a penalty energy for such a situation. However, it should be interpreted in a somewhat more statistical manner. This means that it is not required to yield a strict one-to-one correlation between

incoming and outgoing dislocations rather than a match in the overall shear on either side. Moreover, it is conceivable that the transmission event only rarely takes place owing to the local stiffening effect that it introduces. Along with this grain boundary hardening effect the accumulation of GNDs in front of the interfaces acts as an additional stiffness effect. The mathematical treatment of this dislocation-based approach to grain boundary effects in the CPFE framework shown in Ma et al. [25] leads to the following equation for the penalty energy  $\beta$  that minimizes the activation energy:

$$E_{GB}^{\alpha} = \min_{\beta} \left\{ c'_9 \frac{1}{2} G b^2 l^{\alpha} R^{\alpha} \right\}. \quad (41)$$

where  $c'_9$  is a fitting constant,  $l^{\alpha}$  is the length of the incoming dislocation and  $R^{\alpha}$  is a geometrical factor describing the correlation of the incoming system  $\alpha$  and the outgoing system  $\beta$ .

It is worth mentioning that while the absolute magnitude of  $E_{GB}^{\alpha}$  can be changed by the choice of  $c'_9$ , the ratio of the activation energies for different boundaries is not affected by this value.

As an example, the activation energies of an incoming dislocation with a length  $b$  are calculated for twist boundaries which are characterized by rotations about the [111] and [110] crystal directions, respectively, under the additional constraint that the grain boundary plane is perpendicular to the rotation axes. The calculations apply for the fcc crystal structure. The results are shown in Figs. 10 and 11, where the activation energy has been normalized by the factor  $\frac{1}{2} G b^3$  and the constant  $c'_9$  was chosen to be equal to 1. Both figures show also the average of the energy barrier for better comparison. From these curves it is clear that a grain boundary is a strong obstacle to dislocation motion, as the average activation energies for the formation of the misfit dislocations easily reach the order of magnitude of the activation energy for cutting forest lattice dislocations.

It is observed that the energies for slip penetration are periodic. This effect arises from the octahedral symmetry of the slip systems in the crystal. The activation energy for the penetration shows a complicated relationship with the misorientation, especially when the rotation angle is larger than about 20°. One can see that the energy barrier strongly depends on the misorientation of the two crystals. However, the average activation energies show a much more constant behavior, which implies that the strong effects for single slip systems will be averaged out to some extent in macroscopic experiments.

In most CPFE implementations grain boundaries coincide with element boundaries. In the dislocation-based approach discussed above, a special type of bimaterial element crossing the grain boundary is introduced. In this element one-half of the Gauss points belongs to one crystal, while the other half belongs to the other crystal, see Fig. 12. In this new type of element one can use a modified version of Eq. (24), namely:

<sup>3</sup> The indices  $\alpha$  and  $\beta$  always refer to crystals I and II, respectively.

<sup>4</sup> It is not actually checked whether or not this slip system can be activated by the local stress but it is anticipated as a likely situation as the outbound slip system orientation is close to the inbound one.



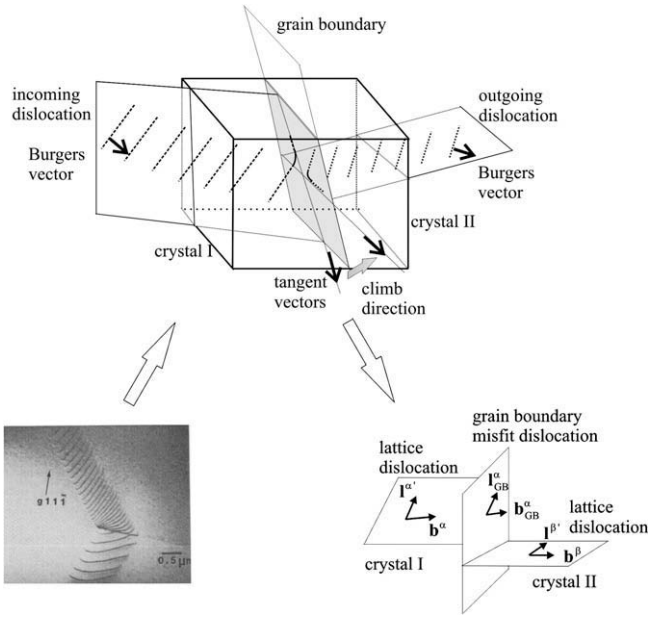


Fig. 9. Schematic drawing of penetration events for mobile dislocations through a grain boundary. The experimentally obtained micrograph is taken from the work of Shen et al. on steel [248]. Here  $\mathbf{l}^{\alpha'}$ ,  $\mathbf{l}^{\beta'}$  and  $\mathbf{l}_{GB}^z$  are the tangent vectors of the dislocations, and  $\mathbf{b}^z$ ,  $\mathbf{b}^{\beta}$  and  $\mathbf{b}_{GB}^z$  are their Burgers vectors.

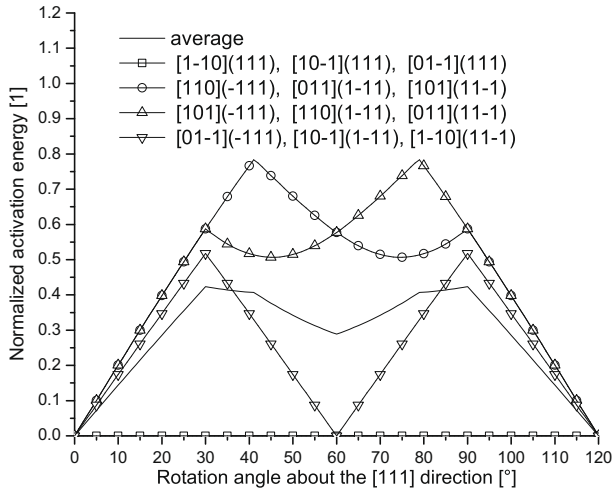


Fig. 10. Normalized activation energy for a twist grain boundary with rotations about the  $[111]$  direction using  $c'_9 = 1$  in Eq. (41). The normalization factor is  $\frac{1}{2}Gb^3$ .

$$v^z = \lambda^z v_{\text{attack}} \exp\left(-\frac{Q_{\text{eff}}^z}{k_B T}\right) \sinh\left(\frac{\tau_{\text{eff}}^z V^z}{k_B T}\right) \text{sgn}(\tau^z) \quad (42)$$

where  $Q_{\text{eff}}^z$  is the modified effective activation energy

$$Q_{\text{eff}}^z = Q_{\text{slip}} + Q_{\text{GB}}^z. \quad (43)$$

When comparing this equation with the one specified in Section 4.3.1, the only difference is the use of  $Q_{\text{eff}}^z$  instead of  $Q_{\text{slip}}$ . According to Eq. (41) the energy  $Q_{\text{GB}}^z$  is calculated by finding the outgoing slip system  $\beta$  that minimizes it:

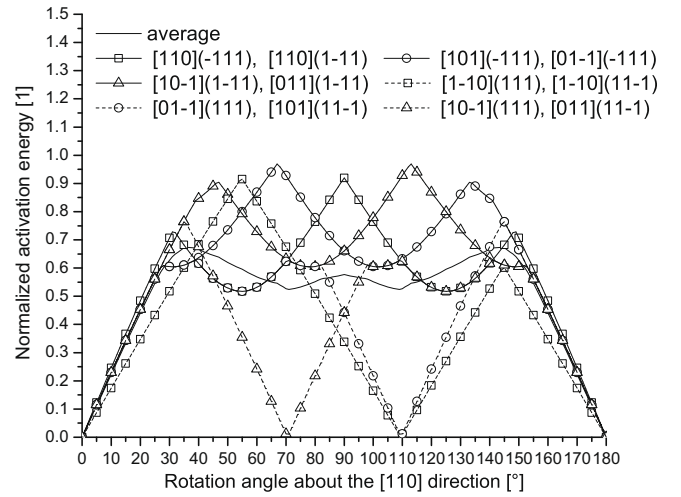


Fig. 11. Normalized activation energy for a twist grain boundary with rotations about the  $[110]$  direction using  $c'_9 = 1$  in Eq. (41). The normalization factor is  $\frac{1}{2}Gb^3$ .

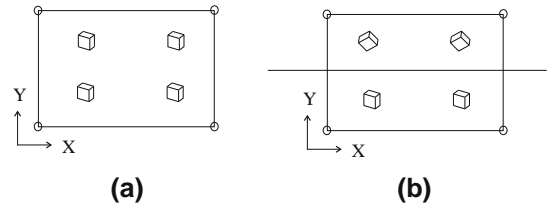


Fig. 12. Two-dimensional schematic drawing of the bulk element (a) and of the grain boundary element (b) for the initial case. During the deformation, for the bulk element GNDs should keep the continuity of the lattice in the  $X$  and  $Y$  directions, while for the grain boundary element the lattice continuity is only kept in the  $X$  direction. In the  $Y$  direction the penetration energy is introduced.

$$Q_{\text{GB}}^z = (E_{\text{GB}}^z)_{l^z=b} = \min_{\beta} c_9 \frac{1}{2} Gb^3 R^z. \quad (44)$$

where  $c_9$  is a dimensionless fitting parameter that is a function of  $c'_9$  and the grain boundary element thickness  $L_{\text{GB}}$ .

## 5. Displacive phase transformations in CPFE modeling

### 5.1. Introduction

The preceding sections focused on dislocations as carriers of plastic shear. However, materials such as austenitic steels, TRIP steels, brass, TWIP steels and shape memory alloys deform not only by dislocation slip but also by displacive deformation mechanisms (also referred to as displacive transformations). These mechanisms are characterized by a diffusionless collective motion of clusters of atoms where each atom is shifted by only a small distance relative to its neighbors. Such transformations create shears with kinematics similar to that of dislocations. Two such mechanisms and their incorporation into the CPFE framework will be discussed here, namely martensite formation [74,80] and mechanical twinning [164–166,169]. Martensite

formation takes place via a shear-induced change of the crystal structure which, as a rule, involves a volume change. Mechanical twinning proceeds by a shear mechanism, which reorients the volume affected into a mirror orientation relative to the surrounding matrix. We discuss how the CPFE approach can be modified to include these mechanisms and how the interactions among the competing shear carriers can be considered in the constitutive formulations.

### 5.2. Martensite formation and transformation-induced plasticity in CPFE models

The presence of metastable retained austenite grains is responsible for the strength–ductility characteristics of TRIP-assisted multiphase steels [250]. Upon mechanical and/or thermal loadings, retained austenite may transform into martensite and generate the TRIP effect. The investigation of the TRIP effect was initiated by Greenwood and Johnson [251] in 1965, where in a test specimen, irreversible plastic deformations were observed at a stress lower than the theoretical yield stress of the material. It has been suggested that the additional plastic deformation of the material is induced by the volumetric growth accompanying the transformation of retained austenite into martensite (e.g. Fischer et al. [252]). In the same year, Patel and Cohen [253] observed that during transformation, martensite develops in a preferred orientation that maximizes the transformation driving force.

Wechsler et al. [254] proposed a crystallographic model for the kinematics of martensitic transformations. This concept was refined by Ball and James [255], who further developed the modeling concept within the energy minimization landscape. During the last decades, various constitutive models for martensitic transformations have been proposed, such as the 1D model of Olson and Cohen [256], which was extended into a 3D model by Stringfellow et al. [257]. Lately, more complex micromechanical models have been proposed (e.g. [67–73,75,83,258–262]), which have been used in particular for simulating TRIP steels. However, the models mentioned above have some drawbacks, i.e. most of them were derived for a small-strain framework. This can lead to inaccurate predictions as mar-

tensite transformations induce locally large elastic and plastic deformations, even if the effective macroscopic deformation is relatively small. Furthermore, an isotropic elastoplastic response is often assumed. This constraint is quite strong, especially at the single-crystal scale, where the effect of crystallographic anisotropy cannot be neglected.

The following sections present the development of a crystallographically based thermomechanical model for simulating the behavior of multiphase TRIP-assisted steels. The austenitic phase is described by a single-crystal elastoplastic transformation model.

The phase transformation model of Suiker and Turteltaub [78,234,263] is applied to simulate the transformation of fcc austenite into body-centered tetragonal (bct) martensite. This model is developed within a multiscale framework and uses the results from the crystallographic theory of martensitic transformations [254,255]. The martensitic transformation model is coupled to a single-crystal plasticity model for fcc metals in order to account for plastic deformation in the austenite. The coupling between the transformation and plasticity models is derived using a thermodynamically consistent framework.

#### 5.2.1. Decompositions of deformation gradient and entropy density

The total deformation gradient  $\mathbf{F}$  and the total entropy density  $\eta$  can be decomposed into the elastic, plastic and transformation parts, in accordance with:

$$\mathbf{F} = \mathbf{F}_e \mathbf{F}_p \mathbf{F}_{tr} \quad \text{and} \quad \eta = \eta_e + \eta_p + \eta_{tr}, \quad (45)$$

where  $\mathbf{F}_e$ ,  $\mathbf{F}_p$  and  $\mathbf{F}_{tr}$  are, respectively, the elastic, plastic and transformation contributions to the total deformation gradient, while  $\eta_e$ ,  $\eta_p$  and  $\eta_{tr}$  are, respectively, the reversible part of the entropy density, the entropy density related to the plastic deformation and the entropy density associated with the phase transformation (see Fig. 13).

The transformation part of deformation gradient,  $\mathbf{F}_{tr}$ , and the transformation entropy density,  $\eta_{tr}$ , are, respectively, given by:

$$\mathbf{F}_{tr} = \mathbf{I} + \sum_{i=1}^M \zeta^i \mathbf{b}^i \otimes \mathbf{d}^i \quad \text{and} \quad \eta_{tr} = \sum_{i=1}^M \zeta^i \frac{\lambda_{tr}^i}{\theta_{tr}}, \quad (46)$$

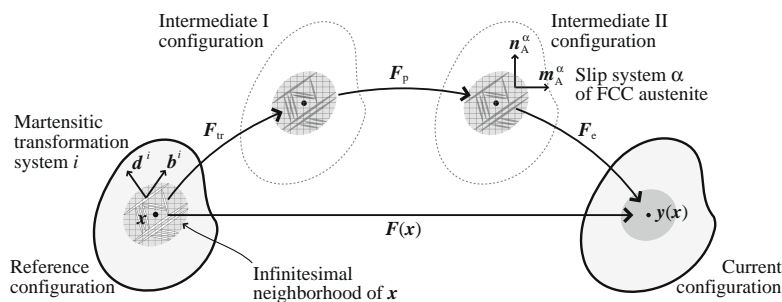


Fig. 13. Schematic representation of the four configurations and the corresponding decomposition of deformation gradient  $\mathbf{F}$  into the elastic, plastic and transformation parts.

where vectors  $\mathbf{b}^i$  and  $\mathbf{d}^i$  are, respectively, the transformation shape strain vector and the normal to the habit plane of transformation system  $i$  (measured in the reference configuration),  $\mathbf{I}$  is the second-order identity tensor,  $\theta_{tr}$  is the (theoretical) transformation temperature, at which transformation occurs instantaneously at zero stress (no energy barrier, no dissipation), and  $\lambda_{tr}^i$  is the latent heat of a transformation system  $i$ , which measures the heat required per unit mass during a complete transformation at the transformation temperature  $\theta_{tr}$ . In equation (46),  $\xi^i$  represents the volume fraction of martensitic transformation system  $i$  measured in the reference configuration, which satisfies the following requirements:

$$0 \leq \xi^i \leq 1, \quad 0 \leq \sum_{i=1}^M \xi^i \leq 1 \quad \text{and} \quad \xi_A = 1 - \sum_{i=1}^M \xi^i, \quad (47)$$

with  $\xi_A$  the volume fraction of the austenite measured in the reference configuration. In the case of the transformation from fcc austenite to bct martensite, the total number of possible transformation systems is  $M = 24$ .

It is assumed that dislocation plasticity only occurs in the austenite but not in the martensite owing to its high yield resistance. Furthermore, plastic deformations that occurred in the martensitic subdomains prior to transformation (if any) are assumed to be inherited to the martensitic phase. Accordingly, the evolution of the plastic deformation gradient  $\mathbf{F}_p$  (given in terms of the plastic velocity gradient  $\mathbf{L}_p$ ) and of the plastic entropy density  $\eta_p$  are, respectively, described by (in rate forms):

$$\mathbf{L}_p = \dot{\mathbf{F}}_p \mathbf{F}_p^{-1} = \sum_{\alpha=1}^{N_A} \dot{\gamma}^\alpha \mathbf{m}_A^\alpha \otimes \mathbf{n}_A^\alpha \quad \text{and} \quad \dot{\eta}_p = \sum_{\alpha=1}^{N_A} \dot{\gamma}^\alpha \phi_A^\alpha, \quad (48)$$

where the vectors  $\mathbf{m}_A^\alpha$  and  $\mathbf{n}_A^\alpha$  are, respectively, unit vectors describing the slip direction and the normal to the slip plane of the corresponding system in the fcc austenite, measured in the second intermediate configuration, and  $\phi_A^\alpha$  is interpreted as the entropy density related to plastic deformation per unit slip in system  $\alpha$ . In the above expressions,  $\dot{\gamma}^\alpha$  can be interpreted as the “effective” plastic slip rate of the austenitic slip system  $\alpha$ , which is given by  $\dot{\gamma}^\alpha = \xi_A \dot{\gamma}_A^\alpha / J_{tr}$ , with  $\dot{\gamma}_A^\alpha$  the rate of slip on a system  $\alpha$  in the austenite and  $J_{tr} = \det \mathbf{F}_{tr}$ .

### 5.2.2. Constitutive relations of stress–elastic strain and temperature-reversible entropy

The constitutive relations between conjugated variables, i.e. stress–elastic strain and temperature-reversible entropy, are defined by:

$$\mathbf{S} = \mathbb{C} \mathbf{E}_e \quad \text{and} \quad \eta_e = h \ln \left( \frac{\theta}{\theta_{tr}} \right) + \eta_{rev}, \quad (49)$$

where  $\mathbf{S}$  is the second Piola–Kirchhoff stress in the second intermediate configuration, which is conjugated to the elastic Green–Lagrange strain,  $\mathbf{E}_e$ ,  $\theta$  is the temperature and  $\eta_{rev}$  is the reversible entropy measured at the transforma-

tion temperature, i.e.  $\theta = \theta_{tr}$ . Furthermore, the effective elasticity tensor  $\mathbb{C}$  and the effective specific heat  $h$  comprise the contributions from the elastic stiffness and the specific heat of the individual austenitic and martensitic phases:

$$\mathbb{C} = \frac{1}{J_{tr}} \left( \xi_A \mathbb{C}_A + (1 + \delta_{tr}) \sum_{i=1}^M \xi^i \mathbb{C}^i \right) \quad \text{and} \quad h = \xi_A h_A + \sum_{i=1}^M \xi^i h^i, \quad (50)$$

where  $\delta_{tr} = \mathbf{b}^i \cdot \mathbf{d}^i$  gives the volumetric growth associated with each transformation system  $i$ , which is constant for all  $i = 1, \dots, M$ . Note that the effective elasticity tensor  $\mathbb{C}$  and the effective specific heat  $h$  evolve with the martensitic volume fractions  $\xi^i$  during transformation.

### 5.2.3. Driving forces and kinetic relations for transformation and plasticity

The driving force for the phase transformation, denoted as  $f^i$ , can be written as:

$$f^i = f_m^i + f_{th}^i + f_d^i + f_s^i, \quad (51)$$

where  $f_m^i$ ,  $f_{th}^i$ ,  $f_d^i$  and  $f_s^i$  summarize, respectively, the mechanical, thermal, defect and surface energy contributions to the transformation driving force. The mechanical part of the transformation driving force,  $f_m^i$ , is computed as:

$$f_m^i = J_{tr} \mathbf{F}_p^T \mathbf{F}_e^T \mathbf{F}_e \mathbf{S} \mathbf{F}_p^{-T} \mathbf{F}_{tr}^T \cdot (\mathbf{b}^i \otimes \mathbf{d}^i) + \frac{1}{2} (\mathbb{C}_A - (1 + \delta_{tr}) \mathbb{C}^i) \mathbf{E}_e \cdot \mathbf{E}_e, \quad (52)$$

which comprises the contribution of the resolved stress and the elastic stiffness mismatch between the martensite product phase and the austenite parent phase with stiffness  $\mathbb{C}_A$ . The thermal part of the transformation driving force,  $f_{th}^i$ , describes the contribution of the transformation latent heat as well as the mismatch of the specific heat between martensite and austenite:

$$f_{th}^i = \rho_0 (h_A - h^i) \left( \theta - \theta_{tr} - \theta \ln \left( \frac{\theta}{\theta_{tr}} \right) \right) + \rho_0 \frac{\lambda_{tr}^i}{\theta_{tr}} (\theta - \theta_{tr}), \quad (53)$$

with  $\rho_0$  being the mass density in the reference configuration. The defect and surface energies contributions are, respectively, given by:

$$f_d^i = \frac{\omega_A}{2} (\mu_A - (1 + \delta_{tr}) \mu^i) \beta^2 \quad \text{and} \quad f_s^i = \frac{\chi}{\ell_0} (2\xi^i - 1), \quad (54)$$

with  $\omega_A$  a scaling factor for the defect energy,  $\beta$  the micro-strain parameter related to the density of dislocations in the austenitic/martensitic region,  $\chi$  an interfacial energy per unit area and  $\ell_0$  a length-scale parameter representing the volume-to-surface ratio of a circular platelet of martensite within a spherical grain of austenite. In Eq. (54)<sub>2</sub>,  $\mu_A$  and  $\mu^i$  represent the (equivalent) shear moduli of the austenite and



martensitic system  $i$ , respectively. The evolution of the martensite fraction during transformation follows the rate-dependent kinetic formulation:

$$\dot{\zeta}_i = \begin{cases} \dot{\zeta}_0 \tanh\left(\frac{f^i - f_{cr}^i}{v f_{cr}^i}\right) & \text{if } f^i > f_{cr}^i, \\ 0 & \text{otherwise,} \end{cases} \quad (55)$$

where  $f_{cr}^i$  stands for the critical value of the transformation driving force. The parameters  $\dot{\zeta}_0$  (maximum transformation rate) and  $v$  (viscosity-like parameter) determine the rate dependence of the transformation kinetic law.

The driving force,  $g_A^\alpha$ , for plastic slip in the austenitic phase is obtained from the thermodynamic formulation as:

$$g_A^\alpha = \mathbf{F}_e^T \mathbf{F}_e \mathbf{S} \cdot (\mathbf{m}_A^\alpha \otimes \mathbf{n}_A^\alpha) + \rho_0 \theta \phi_A^\alpha - \omega_A \mu \beta w^\alpha, \quad (56)$$

where  $\mu$  is the effective shear modulus, which is computed using a similar technique as used for the effective elasticity tensor:

$$\mu = \frac{1}{J_{tr}} \left( \zeta_A \mu_A + (1 + \delta_{tr}) \sum_{i=1}^M \zeta^i \mu^i \right). \quad (57)$$

Furthermore,  $w^\alpha$  is a function that relates the rate of micro-strain  $\dot{\beta}$  to the plastic slip rates  $\dot{\gamma}^\alpha$  as  $\dot{\beta} = \sum_{\alpha=1}^N w^\alpha \dot{\gamma}^\alpha$ . Finally, the evolution of plastic slip in the austenitic phase is described using a power-law kinetic relation in the form:

$$\dot{\gamma}_A^\alpha = \begin{cases} \dot{\gamma}_0^A \left( \left( \frac{g_A^\alpha}{s_A^\alpha} \right)^{1/m_A} - 1 \right) & \text{if } g_A^\alpha > s_A^\alpha, \\ 0 & \text{otherwise,} \end{cases} \quad (58)$$

where  $s_A^\alpha$  is the resistance against plastic slip in system  $\alpha$ . The evolution of the slip resistance is described through a hardening law where  $\dot{\gamma}_0^A$  and  $m_A$  are the reference slip rate and the rate-sensitivity exponent, respectively. More details on the austenite elastoplastic transformation model can be found elsewhere [82].

In order to simulate the behavior of multiphase TRIP-assisted steels, a rate-dependent crystal plasticity model is additionally applied for the ferritic phase. Similar to the austenite elastoplastic transformation model, the kinematics of the model is constructed within a large deformation framework where the total deformation gradient is multiplicatively decomposed into elastic and plastic deformation gradients. Most of the formulation for the ferrite can be derived in a similar way as for the elastoplastic transformation model of the austenite, but without the transformation contribution.

Moreover, at the atomic scale, the plastic deformation in bcc metals involves complex mechanisms due to the non-planar spreading of the screw dislocation cores [264,265]. In order to take these effects into account, the approach of Bassani et al. [266] and Vitek et al. [267] is adopted, where the effect of non-glide stress is incorporated in the model by modifying the critical resolved shear stress according to:

$$\tilde{\tau}_F^\alpha = s_F^\alpha - \tilde{a}^\alpha \tilde{\tau}_F^\alpha. \quad (59)$$

where  $\tilde{a}^\alpha$  is a coefficient that gives the net effect of the non-glide stress on the effective resistance, and  $\tilde{\tau}_F^\alpha$  is the non-glide stress of slip system  $\alpha$ , given by:

$$\tilde{\tau}_F^\alpha = \mathbf{F}_e^T \mathbf{F}_e \mathbf{S} \cdot (\mathbf{m}_F^\alpha \otimes \tilde{\mathbf{n}}_F^\alpha). \quad (60)$$

The kinetic law is constructed through inserting the modified critical Schmid stress instead of the classical slip resistance into a power-law expression for the plastic slip rate. More details on the model for the bcc ferrite are in [82,268].

### 5.3. Mechanical twinning in CPFE models

Arbitrary permanent changes of shape of a single crystal require the operation of any five linearly independent shear systems [4]. However, the number of easily activated slip systems of a given crystal structure may be insufficient to fulfill this requirement. Thus alternative displacive modes, e.g. mechanical twinning, can also participate in the overall plastic deformation. Low-symmetry crystal structures, e.g. hexagonal crystals with large  $c/a$ , are typical examples for this situation. Also, cubic metals may exhibit mechanical twinning due to a relatively strong increase in the critical shear stress at low temperatures and the rate dependence of slip in the case of bcc materials and due to the low value in the stacking fault energy in the case of fcc materials [269]. A mechanical twin formally corresponds to a sheared volume for which the lattice orientation is transformed into its mirror image across a so-called twin/composition/habit plane (Fig. 14). A vector of the initial lattice is moved into its new position in the twin through a transformation/rotation matrix  $\mathbf{Q}$ . The same expression for  $\mathbf{Q}$  was derived for bcc and fcc twins [269,270], exploiting the equivalence of rotating half of the crystal by an angle  $\pi$  either around the twin direction or around the twin normal

$$\mathbf{Q} = 2\mathbf{n} \otimes \mathbf{n} - \delta_{ij} \quad (61)$$

where  $\mathbf{n}$  is the twin plane unit normal and  $\delta_{ij}$  is Kronecker's symbol. Alternatively, twinning can be viewed as unidirectional shear on the habit plane, i.e. formally similar to bidirectional dislocation slip. In this framework, fcc twins are of type  $\{111\}\langle 112 \rangle$ , bcc twins of type  $\{112\}\langle 111 \rangle$  and hcp twins of type  $\{10\bar{1}2\}\langle 10\bar{1}1 \rangle$ . Although strain-induced twinning has been investigated for years [271], most of its governing physical mechanisms still remain unclear. Numerous studies have aimed at identifying the influence

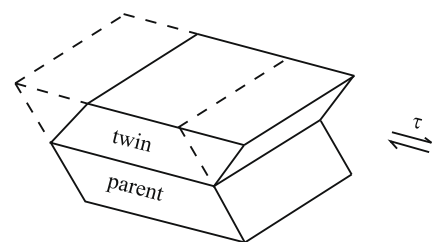


Fig. 14. Under an applied stress, one-half of the initial volume (dashed lines) shears to form a twin (solid lines) (after Hirth and Lothe [269]).

of the boundary conditions on mechanical twinning, focusing on temperature, grain size and stacking fault energy and their respective influence on twin nucleation and growth. Some of the results which are required for deriving corresponding micromechanical models are summarized in the following.

- *Temperature and strain rate.* In most crystal structures twinning gains relevance as the temperature is lowered and/or the strain rate increased. The temperature dependence is often explained by the fact that the flow stress increases steeply with decreasing temperature (in bcc metals), so that finally the twin stress is reached [269]. The temperature dependence of the twin stress is under debate in the literature. Bolling and Richmann [272] and Koester and Speidel [273] found a negative temperature dependence of the twinning stress in fcc crystals, while Mahajan and Williams [274] suggested for the same structure the opposite trend. Contradictory observations have also been reported for other crystal structures, so that the current state of knowledge seems insufficient to reach a definitive conclusion, as pointed out by Venables [275]. Only a few investigations have addressed the strain rate dependence on the twinning stress [276–278].
- *Grain size.* Armstrong and Worthington [279] were the first to propose a link between the increase in the twinning stress and the decrease in the grain size by means of a Hall–Petch-type relation. Later experimental studies on different materials and structures [280–283] supported this suggestion. It is worth noting that the so-called twin slope, i.e. the dependence of twin activation on the grain size, is often found to be much higher than the corresponding slope for dislocation slip [279].
- *Stacking fault energy.* It is well established that twinning occurs preferentially in low stacking fault energy materials. With decreasing stacking fault energy it is easier to separate partial dislocations from each other. This leads to a wider stacking fault, which may eventually trigger a deformation twin. Concerning the effect of other parameters, it was proposed that the stacking fault energy increases with increasing temperature [284]. This might explain the apparent temperature dependence of mechanical twinning. Alternatively, the notion of an effective stacking fault energy was introduced in order to consider the effect of the orientation on the splitting length between partial dislocations [285,286].

The preceding list of relevant parameters affecting mechanical twinning is, of course, not complete since other factors, such as chemical composition, strain and stress state, and precipitates, also influence strain-induced twinning [271].

The motivation for modeling mechanical twinning in a CPFE framework echoes practical as well as fundamental demands. Interest in TWIP steels has grown rapidly over the last years as these grades simultaneously provide high strength and good ductility. Similar aspects hold for stain-

less steels, magnesium alloys and some intermetallic compounds where deformation twinning plays a role. In each of these cases there is an interest in predicting the mechanical response, the microstructure evolution and the texture by using advanced CPFE models.

To our knowledge, the first phenomenological introduction of mechanical twinning into the CPFE framework was accomplished by Doquet [287], followed by Schlögl et al. [288] and Mecking et al. [289]. The corresponding implementation into a FE scheme was proposed by Kalidindi [114,164] and further developed in [290].

### 5.3.1. A modified CPFE framework including deformation twinning

The CPFE framework discussed in this section follows the outline introduced above. However, adding mechanical twinning as a possible plastic shear mode requires introduction of some additional model ingredients. The activation of a twin system  $\beta$  implies that a fraction  $df^\beta$  of the single-crystalline parent volume (matrix) reorients by  $\mathbf{Q}^\beta$ . Fig. 15 illustrates the decomposition of the global deformation gradient  $\mathbf{F}$  when a twin system operates. Considering the formal similarity between slip and mechanical twinning, the velocity gradient  $\mathbf{L}_p$  is extended by the contribution due to the characteristic twin shear  $\gamma_{\text{twin}}$ , e.g.  $\sqrt{2}/2$  for fcc and bcc crystal structures:

$$\mathbf{L}_p = \left(1 - \sum_{\beta=1}^{N_{\text{twin}}} f^\beta\right) \sum_{\alpha=1}^{N_{\text{slip}}} \dot{\gamma}^\alpha \mathbf{m}^\alpha \otimes \mathbf{n}^\alpha + \sum_{\beta=1}^{N_{\text{twin}}} \dot{\gamma}_{\text{twin}}^\beta f^\beta \mathbf{m}_{\text{twin}}^\beta \otimes \mathbf{n}_{\text{twin}}^\beta, \quad (62)$$

where  $N_{\text{slip}}$  is the number of slip systems and  $N_{\text{twin}}$  the number of twin systems. It should be noted that the present description does not explicitly account for the morphology and topology of the deformation twins. Instead a twinned region is specified by its volume fraction and by the boundary condition that no explicit plastic deformation gradient is prescribed within twinned regions. The Cauchy stress  $\bar{\sigma}$  of the composite, i.e. matrix plus twins, is related to the volume average of the stress over all constituents:

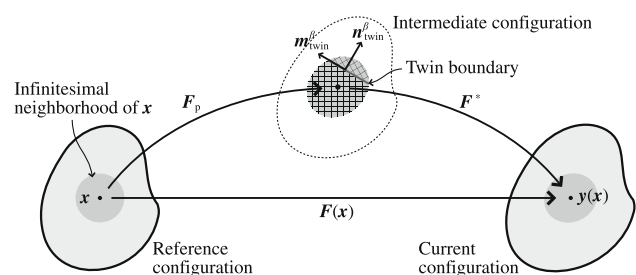


Fig. 15. Schematic representation of the three configurations and the corresponding decomposition of the deformation gradient  $\mathbf{F}$  into elastic and plastic contributions, modified by Kalidindi to account for mechanical twinning [114,164].

$$\bar{\sigma} = \frac{\mathbf{F}_e}{J_e} \left[ \left( 1 - \sum_{\beta=1}^{N_{\text{twin}}} f^{\beta} \right) \mathbb{C} + \sum_{\beta=1}^{N_{\text{twin}}} f^{\beta} \mathbb{C}^{\beta} \right] \mathbf{E}_e \mathbf{F}_e^T, \quad (63)$$

where  $\mathbb{C}_{ijkl}^{\beta} = Q_{im}^{\beta} Q_{jn}^{\beta} Q_{ko}^{\beta} Q_{lp}^{\beta} \mathbb{C}_{mnop}$  is the elasticity tensor of the matrix rotated into the respective twin orientation and  $\mathbf{E}_e$  the Green–Lagrange strain derived from the non-plastic deformation gradient  $\mathbf{F}_e$ . It is worth noting that a small homogenization error may occur when following this procedure, which is due to the generation of an orientation dispersion in the twinned fraction. This deviation occurs whenever the plastic spin of a twin variant is not equal to the plastic spin of the matrix. In the current case this effect does indeed take place because no plastic velocity gradient is given in the twinned regions.

The present expression for  $\mathbf{L}_p$  does not consider subsequent dislocation slip within twins. This approximation is often suitable for extremely thin fcc and bcc twins. However, experimental evidence for dislocation activity in mechanical twins has been reported when twins are larger, e.g. in high-Mn TWIP steels [291] (due to large strains) and in hexagonal metals (Mg, Zr due to small twin shear). It may, therefore, be useful to allow for dislocation slip in twinned regions. In that case, Kalidindi [114] proposed modifying the plastic velocity gradient as follows:

$$\begin{aligned} \mathbf{L}_p = & \left( 1 - \sum_{\beta=1}^{N_{\text{twin}}} f^{\beta} \right) \sum_{\alpha=1}^{N_{\text{slip}}} \dot{\gamma}^{\alpha} \mathbf{m}^{\alpha} \otimes \mathbf{n}^{\alpha} + \sum_{\beta=1}^{N_{\text{twin}}} \gamma_{\text{twin}}^{\beta} \dot{f}^{\beta} \mathbf{m}_{\text{twin}}^{\beta} \\ & \otimes \mathbf{n}_{\text{twin}}^{\beta} + \sum_{\beta=1}^{N_{\text{twin}}} f^{\beta} \sum_{\alpha=1}^{N_{\text{slip}}} \dot{\gamma}^{\alpha} Q^{\beta} \mathbf{m}^{\alpha} \otimes \mathbf{n}^{\alpha} Q^{\beta T}. \end{aligned} \quad (64)$$

Furthermore, secondary twinning, i.e. the twinning of primary twins, might be considered as well. At first sight the modification of  $\mathbf{L}_p$  appears rather straightforward. However, difficulties arise from the increase in the number of shear rates or twin volume fractions that have to be handled in this approach, rendering the model highly impractical. The time-integration scheme, presented in Section 8, remains essentially unchanged. The non-linear equation is still expressed in terms of the second Piola–Kirchhoff stress tensor, written in the intermediate configuration, for a given microstructure, i.e. for state variables that refer to both slip and twinning. Details on the numerical implementation can be found elsewhere [109].

### 5.3.2. Phenomenological approach to mechanical twinning

The plastic velocity gradient is defined in terms of all shear rates  $\dot{\gamma}^{\alpha}$  and all volume fractions created by the twinning rates  $\dot{f}^{\beta}$ . Phenomenological expressions of the shear rate on a slip system have been introduced above. However, no theory is currently available to provide a clear function for the evolution of the twinned volume fraction for an active twin system. For this reason Kalidindi [164] proposed to use the analogy between slip and twin systems while preserving the unidirectionality of the twinning mechanism. The twin volume fraction of a system  $\beta$  then

evolves according to a phenomenological power-law equation:

$$\dot{f}^{\beta} = \begin{cases} \dot{f}_0 \left( \frac{\tau}{\tau_c^{\beta}} \right)^{\frac{1}{m_t}} & \text{if } \tau^{\beta} > 0, \\ 0 & \text{otherwise.} \end{cases} \quad (65)$$

The computation of this flow rule requires the specification of a critical twinning shear stress (shear resistance)  $\tau_c^{\beta}$  for each twin system. This is a critical point since experimental observations support the idea that mechanical twins have a “double” impact on the global strain hardening of the material. First, an increasing amount of twins leads to an increasing hardening effect on slip systems since moving dislocations stop at twin–matrix interfaces. This concept is illustrated in Fig. 16 for the fcc case. A moving matrix dislocation will most likely encounter twins that lie on planes that are non-coplanar with its glide plane, i.e. only non-coplanar twin systems act as obstacles for dislocation motion. Second, the production of new twins is impeded by already existing twins, which is referred as the hardening behavior for the respective twin systems. Following the first idea, Kalidindi proposed modifying the phenomenological slip hardening rule according to:

$$\dot{\tau}_c^{\tilde{\alpha}} = h_{\alpha\tilde{\alpha}} |\dot{\gamma}^{\tilde{\alpha}}| \quad (66)$$

where the hardening matrix  $h_{\alpha\tilde{\alpha}}$  now depends on the twin volume fractions through the saturation value  $\tau_s^{\tilde{\alpha}}$ :

$$\begin{aligned} h_{\alpha\tilde{\alpha}} = & q_{\alpha\tilde{\alpha}} \left[ h_0 \left( 1 - \frac{\tau_c^{\tilde{\alpha}}}{\tau_s^{\tilde{\alpha}}} \right)^a \right] \\ \text{with } \tau_s^{\tilde{\alpha}} = & \tau_0 + \tau_t \left( \sum_{\beta \text{ non-coplanar with } \tilde{\alpha}} f^{\beta} \right)^{\frac{1}{2}} \end{aligned} \quad (67)$$

Dislocations tend to accumulate in front of twin boundaries, which justifies the changes in the saturation value for the slip resistances. The Hall–Petch-like formulation that quantifies the contribution due to deformation twinning in the saturation value is derived naturally from the analogy with grain boundary hardening. It is worth noting that some later works [169] suggest not only modifying the saturation values but also  $h_0$  in order to account for the Basinski effect [169,292]. The second idea refers to a kind of “twin–twin” hardening behavior of the material and originates from the sequential activation of twin variants during deformation. It was often observed that in fcc metals only

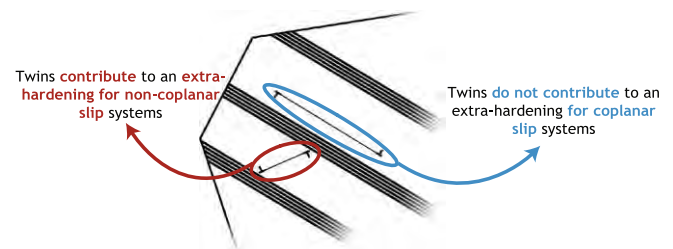


Fig. 16. Illustration of the selective role of twin boundaries during dislocation motion for fcc structures, as proposed by Kalidindi.



coplanar twins initially form in a grain. Upon a strain threshold, deformation twins, that are non-coplanar with the first ones, form, leading to a ladder-like microstructure. This sequential activation, described in Fig. 17, is phenomenologically translated in terms of two monotonic mathematical power functions depending on either strain rate [169] or twin volume fraction rates [114]. The two functions cross at a given point. Below that point, existing twins preferentially harden non-coplanar twin systems. Beyond that point, existing twins preferentially harden coplanar twin systems. This model approach is easy to handle and has been successfully applied to  $\alpha$ -brass [114],  $\alpha$ -Ti [169], and TiAl [288].

#### 5.4. Guidelines for implementing displacive transformations in CPFE constitutive models

This section discussed the basic constitutive and kinematic ingredients for implementing displacive shear mechanisms as additional carriers of crystallographic plastic deformation in CPFE frameworks. The challenges of rendering such models physically sound and at the same time numerically tractable seem to lie in two areas: (i) the appropriate formulation of nucleation and growth models and (ii) the identification of appropriate homogenization methods. The first point means that nucleation and growth models should be designed in a way to capture the basic dependence of displacive transformations on thermodynamic and microstructural parameters such as temperature, grain size, strain rate and stacking fault energy. The second point refers to the desired level of discretization. This means that in some cases multiple and repeated transformations may occur at the same integration point. This requires defining an adequate approach for tracking and homogenizing the volume portions and interaction mechanisms for different twin or martensite lamellae or corresponding higher-order transformations (e.g. twinning of twins)—see Fig. 4b.

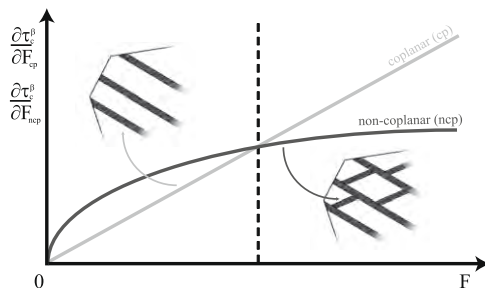


Fig. 17. Sequential activation of twin systems and its mathematical/numerical treatment for fcc structures: at small strains, the hardening evolution of existing twins is mainly governed by the activity of non-coplanar twins. Beyond a critical point, existing twins are strongly hardened by coplanar twins, phenomenologically triggering formation of non-coplanar twins. ( $\tau_c^\beta$  critical twinning shear stress,  $F$ ,  $F_{cp}$ ,  $F_{ncp}$ : cumulative twin volume fraction of all twin systems, only those systems which are co-planar, and those which are non-coplanar to system  $\beta$ , respectively.

## 6. Homogenization methods in CPFE analysis

### 6.1. Introduction

In contrast to the direct crystal plasticity method of modeling aggregates of grains one-to-one, FE analysis is often used to predict the mechanical behavior of engineering structures. This is typically done at the component or design scale using homogenized material properties (indicated by an overbar). At the continuum scale, material points  $\bar{\mathbf{x}}$  in the reference configuration  $\bar{\mathcal{B}} \subset \mathbb{R}^3$  are projected by the non-linear deformation map  $\bar{\mathbf{y}}(\bar{\mathbf{x}}) : \bar{\mathbf{x}} \in \bar{\mathcal{B}} \rightarrow \bar{\mathbf{y}} \in \bar{\mathcal{S}} \subset \mathbb{R}^3$  onto points  $\bar{\mathbf{y}}$  in the current configuration  $\bar{\mathcal{S}} \subset \mathbb{R}^3$ . The corresponding tangent map or deformation gradient is then given by  $\bar{\mathbf{F}} = \nabla_{\bar{\mathbf{x}}} \bar{\mathbf{y}}$ . In order to derive the work-conjugate stress  $\bar{\mathbf{P}}$  (first Piola–Kirchhoff stress) and solve the equilibrium conditions within the FE analysis, a constitutive law which connects  $\bar{\mathbf{P}}$  to  $\bar{\mathbf{F}}$  is required. However, a direct formulation of  $\bar{\mathbf{P}}(\bar{\mathbf{F}})$  and  $\partial \bar{\mathbf{P}} / \partial \bar{\mathbf{F}}$  is in general difficult to impossible, since the mechanical response of (metallic) materials is determined by their underlying microstructure. This microstructure cannot be regarded as a homogeneous continuum but it typically contains grains with differing properties. As a rule, in engineering parts the grain scale is orders of magnitude smaller than the component scale, thus ruling out the possibility of including all degrees of freedom presented by a huge grain aggregate. Therefore, a two-level approach is pertinent. Each material point  $\bar{\mathbf{x}}$  is linked to a domain  $\mathcal{B} \subset \mathbb{R}^3$  containing a finite number of microstructure constituents, e.g. grains, for which the individual constitutive behavior can be modeled, i.e. the constitutive relation between  $\mathbf{P}$  and  $\mathbf{F}$  is known. This constitutive relation is in general dependent on the state of the material, most notably on its thermomechanical history. Since the macroscopic quantities  $\bar{\mathbf{F}}$  and  $\bar{\mathbf{P}}$  are related via the volume averages:

$$\bar{\mathbf{F}} = \frac{1}{V} \int_{\mathcal{B}} \mathbf{F} dV \quad \text{and} \quad \bar{\mathbf{P}} = \frac{1}{V} \int_{\mathcal{B}} \mathbf{P} dV, \quad \text{with } V = \int_{\mathcal{B}} dV, \quad (68)$$

to the corresponding microscopic quantities  $\mathbf{F}$  and  $\mathbf{P}$  inside  $\mathcal{B}$ , this “numerical zoom” shifts the constitutive assumptions between  $\bar{\mathbf{F}}$  and  $\bar{\mathbf{P}}$  from the macro-scale to the micro-scale.

The term “homogenization” now refers to the transition between the micro-scale and the macro-scale defined in a general fashion by Eq. (68). In physics such procedures are also referred to as coarse graining. In the next section we first review methods of how to select grain aggregates in each domain  $\mathcal{B}$  such as to ensure that they reflect the overall crystallographic texture of the material in question in a statistically representative way. After this, the following sections outline three routes which are mainly followed when it comes to the homogenization of viscoplastic polycrystalline materials in the framework of component scale FE analysis.

## 6.2. Statistical representation of crystallographic texture

Crystallographic texture is quantified by the crystallite orientation distribution function (CODF) which defines the probability  $f(\mathbf{Q})$  that a volume fraction,  $dV/V$ , of the polycrystalline aggregate is taken up by crystallites falling into an infinitesimal neighborhood around orientation  $\mathbf{Q}$ :

$$v \equiv \frac{dV}{V} = f(\mathbf{Q}) dQ. \quad (69)$$

The crystal orientation is described by a proper orthogonal matrix  $\mathbf{Q}_{ij} = \mathbf{g}_i \mathbf{e}_j \in SO(3)$  which maps the reference basis  $\mathbf{e}$  onto the crystal basis  $\mathbf{g}$ . Using the notation introduced by Bunge [293], i.e. parameterizing  $\mathbf{Q}$  by Euler angles  $\{\varphi_1, \phi, \varphi_2\}$ , the infinitesimal volume,  $dQ$ , of orientation space follows as:

$$dQ = \frac{1}{8\pi^2} d\varphi_1 d\varphi_2 d\cos\phi. \quad (70)$$

The normalization factor of  $1/8\pi^2$  arises due to the requirement that  $\oint dV/V \equiv 1$ . (Note that  $f(\mathbf{Q}) \equiv 1$  for a random texture.)

The orientation distribution reflects any symmetry present in the crystal lattice and/or the sample geometry. This implies the following symmetry relations:

$$f(\mathbf{Q}) = f(\mathbf{QH}_L) \quad \forall \mathbf{H}_L \in \mathbf{S}_L \subseteq SO(3) \quad (71)$$

$$f(\mathbf{Q}) = f(\mathbf{H}_S \mathbf{Q}) \quad \forall \mathbf{H}_S \in \mathbf{S}_S \subseteq SO(3) \quad (72)$$

with  $\mathbf{S}_L$  and  $\mathbf{S}_S$  being the symmetry group of the lattice and sample, respectively. Therefore, the CODF is fully determined from  $f(\mathbf{Q})$  within any one of the independent regions of Euler space (also addressed as fundamental zones) resulting from Eqs. 71 and 72.

For practical reasons, the CODF is frequently stored in a discrete fashion by subdividing the fundamental zone  $Z$  of Euler space into  $N$  boxes of equal angular extension—typically  $5 \times 5 \times 5$  cubic degrees—and recording discrete values,  $f^i$ , for each box. Ideally,

$$f^i = \int_{\text{box}^i} f(\mathbf{Q}) dQ / \int_{\text{box}^i} dQ = v^i / \int_{\text{box}^i} dQ, \quad (73)$$

i.e. the  $f^i$  values correspond to the CODF average within the  $i$ th box with volume  $v^i$ .

The task now consists of selecting a finite number,  $N^*$ , of discrete orientations such that the overall texture is still represented as accurately as possible by the limited set. Depending on the requirements of the intended simulation, the individual volume fractions assigned to each selected orientation may be either equal or differ from one another.

With respect to the first option, Eisenlohr and Roters [228] recently combined a deterministic scheme with a probabilistic scheme to sample a given number of equally weighted orientations from a discrete CODF. While the probabilistic scheme accepts a randomly chosen orientation in proportion to the respective value of  $f^i$ , the deterministic part is based on the integer:

$$n^i = \text{round}(Cv^i) \quad (74)$$

which gives the number of times the orientation  $i$  should be selected into the representative set. To yield an overall set of  $N^*$  samples the constant  $C$  has to be iteratively adjusted to fulfill:

$$\sum_{i=1}^N n^i \stackrel{!}{=} N^*. \quad (75)$$

This iterative procedure is easily solved, for instance, with a binary search algorithm in a matter of seconds on a standard single-CPU computer. Regarding reconstruction quality, it could be demonstrated that for  $N^* > N$  the set resulting from Eqs. (74) and (75) is much closer to the original CODF than probabilistic sets using  $v^i$  as the probability to include orientation  $i$  (see Eq. (73)). However, for  $N^* < N$  a systematic overweighting of the large original  $v^i$ , and thus pronounced sharpening of the reconstructed texture, is observed. To overcome this inherent problem, the deterministic method is modified as follows: if the requested number,  $N^*$ , of sampled orientations is less than the number of boxes in the (fundamental zone of the) original CODF, i.e. if  $N^* < N$ , one nevertheless generates a population of  $N$  discrete orientations according to Eqs. (74) and (75) but then selects a random subset containing only the requested  $N^* < N$  orientations from the population of  $N$  orientations. By this modification the achieved reconstruction quality is always at least as good as probabilistic sampling but it becomes clearly superior with increasing  $N^*/N$ .

Melchior and Delannay [184] tackled the problem of assigning orientations to an aggregate of  $N^*$  differently sized grains which constitute a representative volume element. They started from a large set of probabilistically selected, equally weighted orientations [227] and introduced an algorithm to divide this set into  $N^*$  collections of similar orientations. Each collection represents a single grain (of average orientation) and comprises as many orientations as is required to match the respective volume fraction of this grain. By allowing this additional degree of freedom in the relative weight of assigned (average) orientations, the reconstruction quality resulting from a fixed number of orientations can be dramatically increased in comparison to equal-weight probabilistic sampling.

Böhlke et al. [294] presented a possible solution to the problem of approximating the CODF by a random background plus a small and fixed number of texture components of variable weight. First, a grid of equal angular extension in  $\{\varphi_1, \phi, \varphi_2\}$  is constructed within the fundamental zone. An approximation then results from superposition of (at most)  $N^*$  von Mises–Fisher distributions,  $g(\mathbf{Q}, \mathbf{Q}^z, w)$ , each centered on a distinct grid point  $\mathbf{Q}^z$  with fixed half-width  $w$ :

$$\bar{f}(\mathbf{Q}) = \sum_{z=1}^{N^*} v^z g(\mathbf{Q}, \mathbf{Q}^z, w). \quad (76)$$

The difficulty arises from selecting appropriate  $\mathbf{Q}^z$  out of the available grid points and assigning respective variable weights  $v^z$  such that the distance

$$D = \int_Z (f(\mathbf{Q}) - \bar{f}(\mathbf{Q}))^2 dQ \quad (77)$$

between the original CODF and its approximation is minimized. This corresponds to a mixed integer quadratic programming (MIQP) problem for which robust solvers exists.

### 6.3. Computational homogenization

Within each region  $\mathcal{B}$  containing a microstructure attached to a certain material point  $\bar{\mathbf{x}}$  one defines the deformation map  $\mathbf{y}(\mathbf{x}) : \mathbf{x} \in \mathcal{B} \rightarrow \mathbf{y} \in \mathcal{S}$  which translates the reference configuration  $\mathcal{B}$  of that microstructure to its current configuration  $\mathcal{S}$ . The associated deformation gradient is given by  $\mathbf{F} = \nabla_{\bar{\mathbf{x}}} \mathbf{y}$ . The deformation map is expressed as the homogeneous deformation  $\bar{\mathbf{F}}\mathbf{x}$ , inherited from the material point, and a superimposed fluctuation field  $\tilde{\mathbf{w}}$ :

$$\mathbf{y} = \bar{\mathbf{F}}\mathbf{x} + \tilde{\mathbf{w}}. \quad (78)$$

Thus the microscopic and macroscopic deformation gradients are related by:

$$\mathbf{F} = \bar{\mathbf{F}} + \tilde{\mathbf{F}} \quad \text{with } \tilde{\mathbf{F}} = \nabla_{\bar{\mathbf{x}}} \tilde{\mathbf{w}}. \quad (79)$$

Combining Eqs. (79) and (68) results in the constraint that the deformation gradient of the fluctuation field vanishes on average:

$$\begin{aligned} \int_{\mathcal{B}} \tilde{\mathbf{F}} dV &= \int_{\partial\mathcal{B}} \tilde{\mathbf{w}} \otimes \mathbf{N} dA \\ &= \int_{\partial\mathcal{B}^-} \tilde{\mathbf{w}}^- \otimes \mathbf{N}^- dA + \int_{\partial\mathcal{B}^+} \tilde{\mathbf{w}}^+ \otimes \mathbf{N}^+ dA = \mathbf{0} \end{aligned} \quad (80)$$

The three equivalent integral terms of Eq. (80) indicate the three possible boundary conditions of different rigorosity. One might rule out any fluctuations at all, i.e.  $\tilde{\mathbf{w}} = \mathbf{0}$  in  $\mathcal{B}$  (i). However, homogeneous boundary conditions, i.e.  $\tilde{\mathbf{w}} = \mathbf{0}$  on  $\partial\mathcal{B}$  (ii), also satisfy Eq. (80). Still more relaxed (periodic) boundary conditions are possible if the boundary is decomposed into two opposite parts  $\partial\mathcal{B} = \partial\mathcal{B}^- \cup \partial\mathcal{B}^+$  with  $\partial\mathcal{B}^- \cap \partial\mathcal{B}^+ = \emptyset$ . Periodicity of the domain  $\mathcal{B}$  is then assured by requiring for each point  $\mathbf{x}^+ \in \partial\mathcal{B}^+$ , that the associated point  $\mathbf{x}^- \in \partial\mathcal{B}^-$  has an opposite normal  $\mathbf{N}^+ = -\mathbf{N}^-$  and equal values of the fluctuation field  $\tilde{\mathbf{w}}^- = \tilde{\mathbf{w}}^+$  (iii). Thus the degrees of freedom offered to the microstructure inside  $\mathcal{B}$ , and hence its compliance, increase from condition (i) to (iii). For the microcontinuum a static equilibrium is assumed, which, in the absence of body forces, is governed by the field equation:

$$\text{div } \mathbf{P} = \mathbf{0} \quad \text{in } \mathcal{B}. \quad (81)$$

Computational homogenization now refers to the numerical solution of the boundary value problem in  $\tilde{\mathbf{w}}$  posed by Eqs. (79) and (81) in connection with a constitutive relationship  $\mathbf{P}(\mathbf{F})$  per individual phase. For this solution, in general, a number of techniques can be employed. The

majority of recent contributions discretized the boundary value problem by means of the FE method, see e.g. [113,295–298], or by using a Fourier series approach on a regular grid [299,300]. In addition, the boundary element method or meshless schemes are equally applicable.

### 6.4. Mean-field homogenization

Within the mean-field approach the microstructure present in the domain  $\mathcal{B}$  is considered as a system of inclusion(s) in a matrix. Here, the boundary value problem outlined in the preceding section is not solved rigorously, but only in a volume-averaged sense. This means that the spatial variation in  $\mathbf{P}$  and  $\mathbf{F}$  is no longer resolved, and thus only spatially averaged quantities per phase  $\alpha$  are considered. Hence, macroscopic quantities valid for the material point equal the volume-weighted sum of the respective quantities over all microstructural constituents. The mean-field counterpart of Eq. (68) then reads:

$$\begin{aligned} \bar{\mathbf{F}} &= \frac{1}{V} \sum_{\alpha} \int_{\mathcal{B}^{\alpha}} \mathbf{F} dV = \frac{1}{V} \sum_{\alpha} V^{\alpha} \langle \mathbf{F} \rangle^{\alpha} \\ \bar{\mathbf{P}} &= \frac{1}{V} \sum_{\alpha} \int_{\mathcal{B}^{\alpha}} \mathbf{P} dV = \frac{1}{V} \sum_{\alpha} V^{\alpha} \langle \mathbf{P} \rangle^{\alpha} \quad \text{with } V^{\alpha} = \int_{\mathcal{B}^{\alpha}} dV \end{aligned} \quad (82)$$

The most basic assumptions regarding the partitioning of stress or strain would be either uniform stress  $\langle \mathbf{P} \rangle^{\alpha} = \bar{\mathbf{P}}$  or uniform deformation gradient  $\langle \mathbf{F} \rangle^{\alpha} = \bar{\mathbf{F}}$  among all phases/grains  $\alpha = 1, \dots, N$  present in the microstructure. These extremal cases were introduced by Reuss [301] and Voigt [302] for elasticity. The fully constrained Taylor [4] assumption corresponds to uniform strain in the case of plasticity. Both assumptions disregard the shape and local neighborhood of the inclusions and generally violate compatibility and equilibrium, respectively. More sophisticated assumptions make use of the solution to the problem of an elastic ellipsoidal inclusion in an infinite elastic matrix given by Eshelby [303]. A recent review of the now well-established laws that govern strain partitioning in a linear elastic composite has been given by Nemat-Nasser and Hori [304]. Out of those, the most frequently employed are the self-consistent approach originally suggested by Kröner [305], and the scheme introduced by Mori and Tanaka [306] (see also [307]). In the former, each inclusion is treated like an isolated one within a matrix having the (unknown) overall stiffness of the composite. The latter embeds each inclusion into the original matrix but considers the average matrix strain to act as far-field strain on the overall composite.

However, extension of such homogenization schemes from the linear to the non-linear case faces difficulties, most significantly because the stiffness, i.e. strain(rate)-sensitivity of stress, is typically inhomogeneous for a given phase due to its heterogeneous strain. The stiffnesses are usually homogenized by using the average strain per phase as a reference input into the respective constitutive law. In order to

establish a link between stress and strain per phase, secant (connecting total stress to total strain) and tangent (connecting stress increments to strain increments) formulations for the moduli are employed. The latter has some advantages since it is not restricted to monotonic loading and generally performs better for anisotropic material behavior. Hill [308] originally introduced this incremental scheme together with a self-consistent approach. Lebensohn and Tomé [309] later proposed a self-consistent integral formalism which links total stress to strain rate. Further self-consistent schemes are, for example, due to Berveiller and Zaoui [310], who employed a secant modulus tensor, while Masson et al. [311] proposed an affine formulation. Recent developments in the incremental tangent formalism can be found, for instance, in [312,313].

### 6.5. Grain-cluster methods

Grain-cluster models are an intermediate approach between the mean-field schemes and spatially resolved solutions of a representative volume element outlined above. They reduce the high computational cost of the latter by restricting the degrees of freedom to a small number of regions with (typically) homogeneous strain inside each zone. Those regions are identified with grains or parts of grains, thus extending the mean-field approaches by taking into account direct neighbor–neighbor interactions among the constituents of a (multiphase) polycrystal. The introduction of grain aggregates now allows relaxation of the assumption of homogeneous strain in each constituent (Taylor)—which generally led to an overestimation of the polycrystalline strength and rate of texture evolution—by enforcing compatibility only in an average sense for the aggregate as a whole.

The basic concept of a partial relaxation of the Taylor hypothesis has been presented in the works of Van Houtte [314,315], Honneff and Mecking [316] and Kocks and Chandra [317].

In his LAMEL model Van Houtte [314,315] considers a stack of two grains subjected to an imposed velocity gradient:

$$\nabla_y \dot{\gamma} = \mathbf{L} = \mathbf{W}_L + \sum_{\alpha} \dot{\gamma}^{\alpha} \hat{\mathbf{b}}^{\alpha} \otimes \mathbf{n}^{\alpha} \quad (83)$$

which is accommodated through lattice rotation  $\mathbf{W}_L$  and crystallographic slip on systems  $\alpha$  slipping at shear rates of  $\dot{\gamma}^{\alpha}$ .  $\hat{\mathbf{b}}^{\alpha}$  is the unit vector along the slip direction of system  $\alpha$ . In each of the two grains—connected by an interface with normal  $\mathbf{n}$ —the local (homogeneous) velocity gradients  $\mathbf{l}^a$  and  $\mathbf{l}^b$  are allowed to deviate from the global one by a number of “relaxation” (shear) modes  $\mathbf{K}^r$  that do not alter  $\mathbf{n}$ :

$$\mathbf{l}^a = \mathbf{L} + \sum_r \mathbf{K}^r \dot{\gamma}^r \quad (84)$$

$$\mathbf{l}^b = \mathbf{L} - \sum_r \mathbf{K}^r \dot{\gamma}^r. \quad (85)$$

Depending on assumptions of the grain shape, typically one or two relaxation modes are considered. In the case

of an interface normal along the macroscopic  $x_3$  direction and for grains which are flat along  $\mathbf{n} = (001)$ , two relaxation modes are considered where the only non-zero component in  $\mathbf{K}^1$  is  $K_{31}^1 = 1$  and in  $\mathbf{K}^2$  is  $K_{32}^2 = 1$ . By distributing the shear relaxation in a symmetric fashion (see Eqs. (84) and (85)), the bicrystal as a whole fulfills the Taylor hypothesis; however, locally different slip systems can be active.

The activity of the real slip systems  $\alpha$  and those attributed to the relaxation modes  $r$  are determined by minimizing the plastic dissipation

$$P = \sum_{\alpha} \tau^{\alpha} |\dot{\gamma}^{\alpha}| + \sum_r \tau^r |\dot{\gamma}^r| \quad (86)$$

with suitably chosen penalty terms for each  $\tau^r$ .

A certain drawback of the original LAMEL model consists in its restriction to deformation modes which are compatible with the presumed grain aspect ratio, e.g. pancake-like grains in rolling. This restriction is overcome by two recent models [20,318] that focus on the boundary layer in between two neighboring grains. Both models apply a relaxation in the plane of the grain boundary (having normal  $\mathbf{n}$ ). The ALAMEL model, introduced by Van Houtte et al. [318], symmetrically relaxes two local velocity gradient components among the neighboring grains such that  $\sum_r \mathbf{K}^r = \mathbf{a} \otimes \mathbf{n}$  with  $\mathbf{a} \perp \mathbf{n}$ . This is identical to the LAMEL case of pancake grains discussed above. As a result, stress equilibrium at the boundary is maintained except for the normal component [318]. The relaxation proposed by Evers et al. [20] is slightly different, as they, firstly, symmetrically relax the deformation gradient on both grains by  $\Delta \mathbf{F} = \pm \mathbf{a} \otimes \mathbf{n}$ , and secondly, determine the components of  $\mathbf{a}$  by prescribing full stress equilibrium at the grain boundary, which is equivalent to a minimization of deformation energy. A real grain structure can then be mimicked by enclosing each grain with bicrystalline contacts towards its neighbors. The distribution of interface orientations reflects the (evolving) grain morphology thus decoupling grain shape from the deformation mode under consideration.

An extension of the monodirectional, thus anisotropic, two-grain stack considered in above-mentioned LAMEL model to a tridirectional cluster of  $2 \times 2 \times 2$  hexahedral grains is due to Crumbach et al. [319] based on work by Wagner [320]. In this scheme, termed the grain interaction (GIA) model, the overall aggregate is subdivided into four two-grain stacks with the stacking direction aligned with the shortest grain direction  $j'$  and another set of four stacks with the stacking direction aligned with the second-shortest grain dimension  $j''$ . Relaxation of  $\epsilon_{ij'}$  ( $i = 1, 2, 3$ ) and  $\epsilon_{ij''}$  ( $i \neq j'$ ) is performed in the spirit of LAMEL, i.e. via mutually compensating shear contributions of both stacked grains, such that each two-grain stack fulfills the external boundary conditions—and in consequence the cluster as a whole. To maintain inter-grain compatibility—possibly violated by different strains in neighboring stacks—a density of GNDs is introduced, which forms the basis for the evaluation of the mismatch penalty energy



in Eq. (86). The profound advance of the GIA approach is that it connects the inter-grain misfit penalty measure to material quantities such as the Burgers vector, shear modulus, work-hardening behavior and grain size. The GIA model formulation is compatible with arbitrary deformation modes and is, hence, not confined to plane strain. It was recently used in conjunction with a FE solver where it served as a texture-dependent homogenization model [321].

#### 6.6. Guidelines for implementing homogenization models in CPFE frameworks

This section presented different types of homogenization concepts. They all have the common aim of describing the local mechanical interaction of clusters of crystals (including also different phases if required) that are jointly exposed to fixed boundary conditions. Relaxations may occur inside these clusters depending on model complexity.

It must be emphasized that no homogenization model is principally correct or incorrect. For instance, the use of an equal-stress hypothesis (same stress in all grains) can be sensible when two sequentially arranged crystals are stressed, and a Taylor–Bishop–Hill hypothesis (same strain in all grains) may be adequate when two crystals are arranged parallel to each other and are jointly exposed to the same displacement. This means that the homogenization model may be chosen according to the expected boundary conditions. Even simple homogenization models can provide decent results for certain loading situations while failing for others.

Another important aspect in selecting the right homogenization model is the property that is to be predicted. For instance, the simulation of certain microstructure features such as grain misfit quantities (e.g. GNDs), internal strains or crystallographic textures typically require a higher level of detail in the underlying homogenization model than the prediction of a polycrystal flow curve.

An essential step in the development and implementation of homogenization models is the validation procedure. According to the experience of the authors the best way to test homogenization models lies in the prediction of crystallographic textures. The reason for this recommendation is that, first, deformation-induced texture changes are very sensitive to model and boundary condition details, and second, textures can be quantitatively measured and compared one-to-one with corresponding predictions. Homogenization models that predict wrong textures will most likely also predict wrong mechanical properties. In contrast, a model providing satisfying mechanical results does not necessarily predict correct textures.

Finally, it is an obvious requirement that the chosen homogenization model must be suited for the size of the simulated part in order to reduce computation time to a reasonable level.

## 7. CPFE approaches to local damage analysis

### 7.1. Continuum approaches to modeling damage

Continuum damage and fracture mechanics have provided a wealth of methodologies for modeling the evolution of damage, but these methods all depend on knowing where the damage nucleated; hence a pre-existing void or crack is normally introduced. Although this offers no cognizance of micro-scale processes, it has been effective in modeling stochastic aspects of failure for problems involving multiple phases. When damage sites are randomly distributed in a continuum material, isotropic FE models can predict how shear localization develops within a particular arrangement of damage sites: holes close together and align with directions of maximum shear stresses coalesced by shear localization at small strains, subsequently developing into a crack path. For example, for voids or hard particles located in random positions, Becker [106], Nicolaou and Semiatin [326,327], Horstemeyer et al. [328] and Pardoen et al. [329] investigated the effects of damage location on shear localization that precedes crack propagation. Given that shear localization can be simulated in continuum models, it is important to identify the locations of damage nucleation with respect to microstructural features and slip systems (e.g. Fig. 18).

While this approach can model the effect of specific damage sites on the surrounding material, damage can also be embedded into the material constitutive model without modeling damage sites explicitly. The effects of clustering of hard phases in metal matrix composites, and deformation of porous materials, have been modeled using Eshelby inclusions [330].

Another well-developed way to model homogenized damage is based on the observation that damage reduces the bulk elastic modulus [331], hence damage is introduced into the elastic part of the problem:

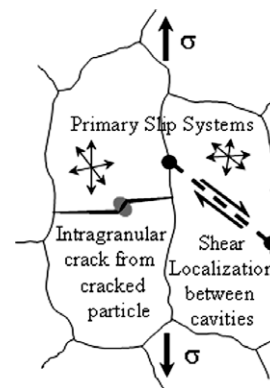


Fig. 18. Influence of crystal orientation on grain or phase boundary damage nucleation. The grain on the right has two widely spaced damage sites that are favorably oriented for shear localization between them. In contrast, the grain on the left has two closely spaced damage sites that are not favorably oriented for shear localization, but an intragranular crack can develop from the cracked particle.

$$\sigma = \mathbf{C} : \epsilon^e (1 - D) \quad (87)$$

where  $D$  is a scalar quantity ranging from 0 (no damage) to 1 (fully damaged) (the plastic response follows as a consequence). Many authors have recognized that damage represented by the parameter  $D$  is not isotropic, and have introduced vectorial and tensorial modifications to this idea to simulate failure processes associated with crystallographic planes, intergranular fracture or distortion and growth of voids—see e.g. Luccioni and Oller [332], Menzel et al. [333] or Voyiadjis and Dorgan [334].

As continuum approaches are valuable for design and modeling at the component scale, it is desirable to develop a method by which the continuum anisotropic damage formulations can be informed by physically modeled plastic processes. Thus, if models of microstructures using CPFE methods can identify how dislocation-based deformation processes cause damage nucleation and evolution, then these can be expressed in forms that are ready for use in continuum scale models.

## 7.2. Microstructurally induced damage

Micromechanics studies imply that shear localization at the micro-scale occurs as a result of microstructure characteristics such as inclusion morphology and distribution, grain boundary character, texture, grain shape, and the operation of slip systems coupled with damage site locations. Fig. 18 illustrates how two cavities that are close together may not coalesce preferentially if the slip systems are not favorably oriented. Thus, shear localization, and hence the toughness, will depend upon anisotropic microstructural details. This anisotropic effect is observed at the macro-scale by 25% variations in  $K_{Ic}$  with respect to direction in rolled sheet material [335]. However, there has been limited study of how the crystallographic processes lead to failure mechanisms that depend on local grain and grain boundary orientations, making damage modeling using CPFE approaches an important area for future study. In particular, CPFE allows the direct modeling of experimentally characterized microstructures where damage has been observed, in order to evaluate theories of damage nucleation and early growth stages.

Grain boundaries are often sources of critical damage nucleation, even when pre-existing cracks may be present within a grain. In Al alloys, the primary mechanisms for grain boundary crack nucleation are void coalescence between grain boundary precipitates [336,337]. In fatigue conditions, subcritical short cracks either pre-exist due to cracked inclusions (such as constituent particles, see Fig. 18) or from cracking early during fatigue cycling, but do not propagate past a limiting grain boundary or past a triple line [338,339]. When short cracks are able to penetrate a grain boundary, they make the transition to longer cracks that can then be modeled with established continuum fracture mechanics. This penetration event often takes place late in the cycling process, indicating that

crack penetration of the grain boundary may control fatigue life.

### 7.2.1. Heterogeneous plastic deformation

Both experimental and computational studies suggest that damage nucleation occurs in locations of large strain concentrations, which develop in locations of substantial heterogeneous deformation near microstructural features such as grain or phase boundaries. However, if a large local strain is effective in accommodating a required local geometry change (due to boundary conditions imposed by differential deformation amounts in the local neighborhood) a locally large strain may prevent damage nucleation. In contrast, damage may nucleate where an insufficient amount of strain occurs to accommodate a locally required shape change, such that opening a free surface may require less energy than further intragranular deformation. Clearly, not all large strain sites are damage sites, and damage may develop where strains are modest.

It is well known that strain varies from grain to grain due to the effects of differing deformation processes in neighboring grains (Fig. 3). The spread of deformation within a grain does not only depend on the orientations of the neighboring grains, but also on the constraints provided by neighboring grains that diminish but are still significant several grains away [106,197,340]. Within a given grain, slip traces of deformation systems with high Schmid factors may extend across grains, while planes with moderate Schmid factors may reveal slip traces that extend part way from a boundary into the grain interior. Experimentally measured surface strain maps on high-purity copper polycrystals show that heterogeneous strains extend 20–100  $\mu\text{m}$  into the grain interior [322,341]. Local lattice rotations have been measured using orientation imaging microscopy, which has allowed direct comparisons between experiment and CPFE models [14,38,90,342,343]. Simulations of local rotations measured using high-resolution strain mapping and local strain accumulation effects can be better understood at the grain scale when a local micromechanical Taylor factor is used to identify the activated slip systems [38].

Because damage originates from strain incompatibilities in specific sites, it is most appropriate to investigate conditions that lead to damage nucleation using CPFE methods that model experimentally realistic microstructures (e.g. Hao et al. [344], Clayton and McDowell [322], Bhattacharyya et al. [90], Raabe et al. [38], Ma and Roters [23], Ma et al. [24,25], Zaafarani et al. [171], Cheong and Busso [22], Dawson et al. [345], Kalidindi and Anand [346]). As damage events reflect interactions between the microstructure scale and the atomic scale, they are intrinsically nanoscopic. Thus, multiscale modeling approaches that include atomistic scale computations are under development by a number of groups [322,347–350].

### 7.2.2. Interfaces

Interfaces represent a profound challenge to modeling heterogeneous deformation and damage nucleation. The

cohesive strength of the boundary in real polycrystals varies according to the atomic scale arrangement; some boundaries have more disorder than others [351], leading to lower interfacial cohesive strength. Many studies have correlated properties of boundaries with their interfacial structure through coincident site lattice (CSL, or low  $\Sigma$ ) boundaries. Because low  $\Sigma$  boundaries have less free volume due to better packing efficiency, these boundaries are assumed to be strong. Materials with large numbers of low  $\Sigma$  boundaries [352–354] that are well connected as networks [355] exhibit higher flow stress and ductility than materials with few low  $\Sigma$  boundaries (a weak boundary percolation can occur if there are less than 78% low  $\Sigma$  boundaries [356]). Because low  $\Sigma$  boundaries are less able to absorb lattice dislocations than random boundaries [357], many researchers have attributed material strength, and/or resistance to damage nucleation, to the presence of low  $\Sigma$  boundaries [358]. This characterization of the boundary state is useful in computational modeling, as the grain boundary energy used in a Griffith criterion provides a criterion for nucleating a crack.

### 7.2.3. Cohesive zone boundary modeling

The energy-based definition of the grain boundary character has been modeled in CPFEM modeling using the cohesive force model first presented by Needleman [359,360], who described the cohesive energy as an empirical scalar function that relates displacement to normal and shear traction evolution in the boundary plane (Fig. 19). Such formulations have been adopted in damage nucleation models [361,344]. Clayton and McDowell [322] used non-

local models to accurately predict local stress–strain history, and hence tractions, on the boundary. From this analysis, they identified a parameter which could be used to predict damage nucleation locations, based upon how much accommodation by void damage is required by the material to deform to a given strain level. This model assumed isotropic interfacial energy for all boundaries (molecular dynamics modeling can overcome this, but at a much smaller scale). Such models have been evaluated to identify how nucleation and growth of voids affects subsequent deformation processes (e.g. Fig. 20). Cohesive interface energy models are appealing in that they are two-dimensional, but they do not use the available information regarding operating slip systems to examine or analyze damage evolution.

Low  $\Sigma$  boundary attributes are not a sufficient definition of a strong or weak boundary. First, the beneficial effect of low  $\Sigma$  boundaries cannot be exclusively ascribed to lower solute content, because solute atoms can also strengthen grain boundaries, e.g. B doping in aluminides. Second, even though the benefit of low  $\Sigma$  boundaries is statistically convincing, some low  $\Sigma$  boundaries do develop damage, while many more random boundaries do not, e.g. Lehockey and Palumbo [325], Fig. 21, suggest that additional criteria for identifying strong and weak boundaries exist, such

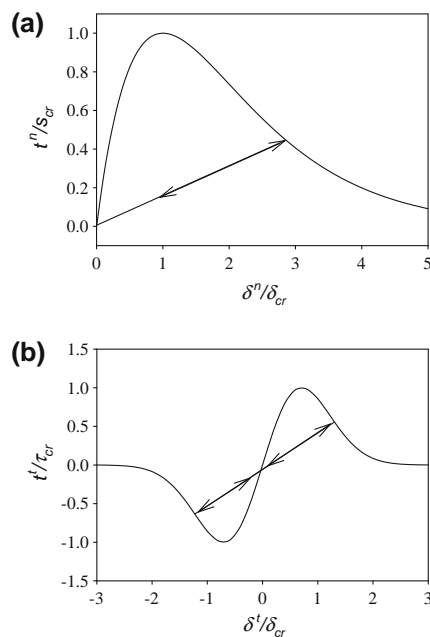


Fig. 19. Cohesive zone interfacial strength models: the vertical axis is a normalized tensile (a) or shear (b) strength, and the horizontal axis is a normalized displacement. The arrows indicate unloading/reloading paths [322].

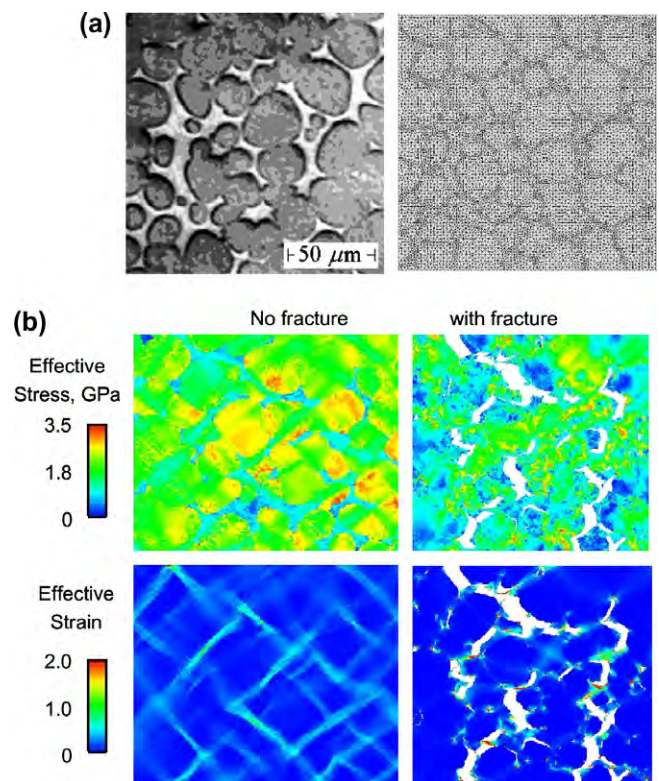


Fig. 20. Influence of cohesive zone interfacial strength models coupled with non-local CPFEM microstructure models on plastic strain development with and without use of boundary strength models; representative 2-D plane strain microstructure (experimental, left) and mesh for a two-phase W-(Ni, Fe) alloy (a), and effects of fracture criteria on stress and strain obtained in simulations (b) Clayton [323,324].



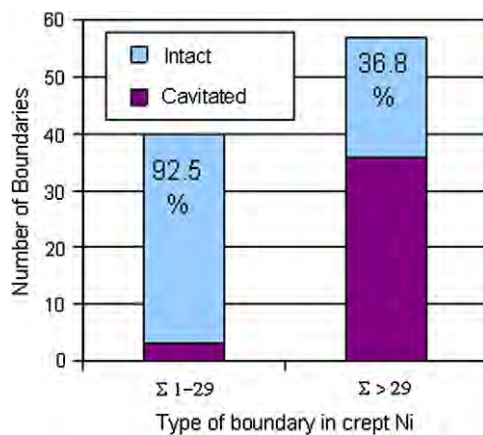


Fig. 21. While the intact boundary fraction is very high in the low  $\Sigma$  boundaries, many higher  $\Sigma$  boundaries are also intact [325].

as the influence of active deformation systems. Third, some general boundaries have special properties based upon the rotation axis [362], or “plane-matching boundaries”, which are statistically more common than low  $\Sigma$  boundaries [363]. Fourth, the benefit of low  $\Sigma$  boundaries has rarely been examined in non-cubic materials, even though the structure of low  $\Sigma$  boundaries is known (e.g. hcp, [364]; L1<sub>0</sub>, [365]). Finally, grain boundary dislocations are also important, as they are interrelated with the structure of the boundary, and they affect how slip can be transferred across a boundary, as discussed in the next section. Much of the grain boundary engineering literature is more focused on creating networks of low-angle boundaries with heat treatments than examining why they are effective.

#### 7.2.4. Grain boundary slip transfer

The analysis of heterogeneous strain near boundaries was initiated by Livingston and Chalmers [366], who observed that more slip systems are active near bicrystal grain boundaries than in the grain interiors. However, bicrystals with arbitrarily oriented grains generally activate only one slip system in the grain interior (unless orientations are chosen that have the same Schmid factor for multiple slip systems), unlike polycrystals that generally require activation of two or more slip systems due to compatibility constraints. While bicrystal deformation provides insights about mechanisms of deformation transfer, the results cannot be directly transferred to general grain boundaries in polycrystals.

Studies of deformation transfer have led to identification of some rules by which a dislocation in one grain can penetrate into a neighboring grain [249,367]. These rules have been confirmed with atomistic scale simulations by de Koninck et al. [368]. The slip transmission process often leaves residual dislocations in the boundary and requires a change in direction of the Burgers vector along with a change in the plane orientation, resulting in two intersecting lines in the grain boundary plane. This geometry is illustrated in Fig. 22, and the three “rules” that summarize conditions for slip transfer are:

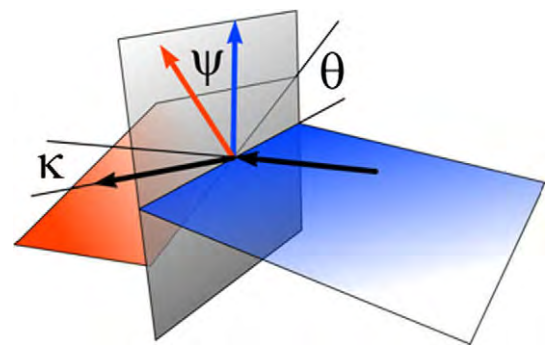


Fig. 22. Angles and vectors used to evaluate the geometrical efficiency of strain transfer at a grain boundary [199].

- The angle between the lines of intersection between the grain boundary and each slip system ( $\Theta$ ) must be a minimum.
- The magnitude of the Burgers vector of the dislocation left in the grain boundary (correlated to the magnitude of  $\kappa$ ) must be a minimum.
- The resolved shear stress on the outgoing slip system must be a maximum.

Semi-quantitative geometrical expressions describing the likelihood of a slip transmission event have been developed. Luster and Morris [369] noted that large values of  $\cos \psi \cos \kappa$ , were correlated with observed instances of slip transmission. Slip transmission criteria depend strongly on the degree of coplanarity of slip systems engaged in deformation transfer ( $\Theta$  will be small if  $\psi$  is small). Other studies of deformation transfer have focused more on the misalignment of the Burgers vector *colinearity* ( $\cos \kappa$  in Fig. 18), such as Gibson and Forwood [370], who found that twin impingement at boundaries in TiAl is accommodated by  $a/2[110]$  ordinary dislocation slip on a variety of planes on both sides of the boundary, with residual dislocations left in the boundary.

The process of slip transfer is also dependent on grain boundary dislocations. Grain boundary dislocation Burgers vectors may or may not reside in the boundary plane, making them mobile or sessile, respectively. Even if boundary dislocations are mobile, they face barriers at triple lines, where they may or may not be able to continue to propagate. Triple lines are often described as I- or U-lines [371], where I-lines are typically intersections of  $\Sigma$  boundaries. Dislocation transmission without development of dislocation debris is possible through I-lines, so that they permit slip transfer, whereas U-lines providing sources or sinks for lattice dislocations during deformation. Thus, triple line characteristics affect properties [371,372], e.g. cavitation and cracking are more likely at U-lines [373].

There is an interesting disconnect between the slip transparency of I-lines, and the fact that networks of such boundaries may even increase the strength [374,375]. Clearly, the influence of low  $\Sigma$  boundaries and associated I-lines on damage nucleation mechanisms is only partially



understood. However, it appears important to focus attention on damage nucleation mechanisms in high  $\Sigma$  and random boundaries that are more likely to develop damage, because there will always be a significant number of random boundaries in polycrystals.

Consideration of the geometry of slip transfer suggests that there are three classes of boundaries with respect to their mechanical behavior:

- (I) The grain boundary acts as an impenetrable interface which leads to the operation of additional intragranular (self-accommodating) slip systems that generate localized rotations [95] in order to maintain boundary continuity.
- (II) The boundary is not impenetrable, and slip in one grain can progress into the next grain with some degree of continuity (leaving residual boundary dislocations, and perhaps only partial ability to accommodate a shape change).
- (III) The boundary is transparent to dislocations, and (near) perfect transmission can occur (e.g. low  $\Sigma$  boundaries related to I-lines, [376] or low-angle boundaries [95,375], this type of boundary is most naturally modeled with CPFEE methods).

Further complications are suggested from experimental observations. From nanoindentation experiments it is known that grain boundaries impose a threshold stress effect, such that strain bursts through a boundary occur with increasing stress–strain due to achieving a stress sufficient to activate a grain boundary source [377]. The misorientations of boundaries, and hence their properties, change with strain [378]. For example, a change in boundary character that affects dislocation absorption or emission from the boundary will affect the localized rotation gradients arising from GNDs.

This discussion clearly shows that before damage nucleation can be predicted, deformation transfer mechanisms must be modeled in a reasonable manner. Further, if a relationship between deformation transfer and damage nucleation can be developed, this would provide an effective bridge between atomistic and continuum scale models.

To make computational modeling of damage nucleation possible in the CPFEE paradigm, grain boundary elements that allow physically realistic deformation transfer are necessary. Two approaches of modeling grain boundary deformation have been proposed by Ma et al. [25] and Ashmawi and Zikry [379]. In both cases, grain boundary elements with finite thickness were used. Ashmawi and Zikry [379] used the grain boundary element to track the evolution of dislocation density in elements in an envelope fanning into the grain interior on either side of the boundary. The most active slip system in this envelope was evaluated, and then this density was tracked. Grain boundary elements accumulated the impinging dislocation density as a damage factor in a continuum element similar to  $D$  in Eq. (87) above; this is interpreted as a pile-up that causes

cavitation to develop, and hence the reduction in stress-carrying capability. The density was reduced if slip transfer occurred, i.e. if  $\Theta < 15^\circ$  and  $\kappa < 35^\circ$  in Fig. 22 (based upon experimental observations of Werner and Prantl [367]), then slip transfer was permitted in proportion to the geometrical factor  $\cos \Theta \cos \kappa$  to reduce the accumulated dislocation density in the grains on either side. This formulation used arbitrary square crystal plasticity elements in square grains with thinner grain boundary elements using the continuum-based damage nucleation model, so it was not examined using practical microstructures.

In contrast, Ma et al. [25] developed a boundary element with crystal plasticity components with an increased resistance to flow stress based upon the fractional dislocation debris left in a boundary when slip transfer occurs (see details in Section 4.3.2). This increase in flow resistance is expressed as an increase in the activation energy barrier for dislocation slip within the grain boundary element, and hence the deformation process in the boundary is kept crystallographic. However, in both cases, the process of what happens to dislocations that retain some sense of their identity as they penetrate into the neighboring grain is neglected for simplicity in the interest of capturing at least some of the physics of the process. There is clearly an opportunity for further insightful development of a practical grain boundary element that can capture both the dislocation slip transfer and the damage nucleation processes in practical and realistic ways.

#### 7.2.5. Experimental studies of fracture initiation criteria

While much research in CPFEE has focused on ductile cubic metals, damage nucleation is much more critical in low-ductility metals and intermetallics, at both ambient and high-temperature conditions. Due to more limited slip, it is easier to experimentally identify relationships between slip, twinning and damage nucleation in slip-limited materials. After making unsuccessful attempts to correlate damage with slip transfer using only geometric parameters, Simkin and Bieler [380] developed a fracture initiation parameter (*fip*) that is based upon the activity of slip and twinning systems in a stressed condition for adjacent grains in TiAl. The *fip* is analogous to a probability statement about how likely it is that a given grain boundary will crack when subjected to a stress field. A *fip* consists of several physical/geometrical factors that could enhance crack nucleation due to localized shear strain concentrated at the boundary. Variations of this idea are presented in equations as  $F_i$ , where  $i$  is a label [380–384]. For example, the *fip* parameter  $F_1$  is the product of three terms:

$$F_1 = m_{tw} |\hat{\mathbf{b}}_{tw} \cdot \hat{\mathbf{t}}| \sum_{ord} |\hat{\mathbf{b}}_{tw} \cdot \hat{\mathbf{b}}_{ord}| \quad (88)$$

The first term is the Schmid factor of the most highly stressed twinning system in a grain pair,  $m_{tw}$ , which identifies twins that cause the largest shear discontinuity at a grain boundary. The second term is the scalar product of the unit vector of this twin's Burgers vector direction,

$\hat{\mathbf{b}}_{\text{tw}}$ , and the unit vector pointing in the direction of the maximum tensile stress  $\hat{\mathbf{t}}$ , i.e.  $\hat{\mathbf{b}}_{\text{tw}} \cdot \hat{\mathbf{t}}$ , which identifies the strength of a mode I opening component at the boundary. This term is the part of the Schmid factor related to the slip direction. The third term,  $\sum_{\text{ord}} |\hat{\mathbf{b}}_{\text{tw}} \cdot \hat{\mathbf{b}}_{\text{ord}}|$ , is the sum of scalar products between the Burgers vector of a highly stressed twin system in the initiating grain (with Schmid factor  $m_{\text{tw}}$ ) and the Burgers vector of available ordinary slip systems in either the same grain or the neighboring (responding) grain. This term describes how well the local shear direction at the boundary can be accommodated by dislocation activity in the neighboring or initiating grain, i.e. the scalar product defined by the angle  $\kappa$  in Fig. 22. This quantitatively expresses one of the three requirements identified by Clark et al. [249] for slip transfer. The sum term is maximized when two or more slip systems have a modest value of  $\kappa$ , because when the scalar product is near 1 for one slip system, the scalar product is much smaller for the rest. Thus, the sum is large when the opportunity for imperfect slip transfer is large.

From experimental measurements, the *fip* is larger for cracked boundaries than intact boundaries, implying that imperfect slip transfer (which leaves residual dislocation content in the boundary) is strongly correlated with crack nucleation. This approach has been shown to be statistically significant in two different materials under different loading and temperature conditions: ambient temperature deformation in equiaxed (duplex) TiAl, and during creep in high stress creep of a Co-based superalloy [384]. While this suggests that the *fip* concept may be a robust predictor of damage nucleation, further examination of this concept in other material systems is needed.

#### 7.2.6. Strain energy as a criterion for damage

Strain energy is a commonly used criterion for damage. A recent example that illustrates this approach in crystal plasticity studies is in the work of Dunne et al. [340], who used cumulative plastic slip as a means to predict damage sites in CPFE studies of Ni and Ti alloys in low-cycle fatigue studies. In the maximum stress region of a continuum model of a three-point bend specimen, they inserted a crystal plasticity section with the same grain configuration as a carefully analyzed experiment. Planes with highly active slip corresponded to planes with high Schmid factors and observed slip bands in the experiment. With a one-dimensional damage model similar to Eq. (87), they were able to simulate the locations of persistent shear bands and crack positions in a three-point fatigue bending specimen. However, the details of the crack nucleation differed between the experiment and simulation. This was in part due to simplifying assumptions regarding the stress state. This work showed that shear bands and cracks are very sensitive to the actual local geometry of grains.

The importance of local geometry was further emphasized in a systematic computational study of fatigue facet (crack) formation in hard orientations of titanium in polycrystals [340]. Particular orientations of adjacent crystals

and particular grain boundary inclinations were found to be most likely to generate slip penetration from the adjacent soft grain into the hard grain such that tensile stresses developed normal to basal planes. Such conditions facilitate formation of facets that develop into fatigue cracks. This computational study was consistent with features in deeply characterized experiments of Sinha et al. [385] and Bieler et al. [386].

CPFE is particularly valuable for identifying microstructural conditions where strain incompatibility develops (this is exaggerated in slip-limited materials). These incompatibilities develop due to activation of slip systems that cause shears in very different direction in adjacent grains, leading to significant local triaxial stress states and load shedding to harder orientations. Self-consistent modeling of generic microstructural characteristics have been used to estimate plausible stress states (e.g. [386]), but as the prior examples show, the actual grain geometry leads to very significant variations around such estimates. It is clear that strain energy is an important metric for predicting locations where damage is possible, but clearly there are additional criteria that must be considered (and identified) to account for the fact that not all sites with potentially dangerous characteristics actually develop damage.

#### 7.3. Assessment of current knowledge about damage nucleation

CPFE modeling is an enabling tool for examining conditions that lead to damage nucleation. However, the physical understanding that is needed to develop computationally efficient and robust criteria is relatively undeveloped. Rather than stating what only may be true on the basis of recent studies, relationships between heterogeneous strain and damage nucleation can be provided as a list of hypotheses that can be explored in combined experimental and CPFE computational modeling research programs.

1. Damage nucleation always occurs at locations of maximum strain energy density (maximum area under the local stress–strain curve).
2. Large local strains can provide geometric accommodation that can prevent damage nucleation.
3. Damage nucleation arises from slip interactions resulting from imperfect slip transfer through a boundary, which leaves residual dislocation content in the boundary plane.
4. Damage nucleation occurs in particular boundaries where unfavorable slip interactions take place at the boundary to weaken the boundary.
5. Slip interactions at the boundary are more (or less?) important than the magnitude of local strain for predicting damage nucleation.
6. Damage nucleation occurs in locations where there is maximum geometric incompatibility arising from highly activated slip systems that cause dominant shears in very different directions (e.g. [387]).

7. Damage nucleation is highly correlated with severe local strain heterogeneity, e.g. lattice curvature.
8. Dislocation density-based (non-local) formulations of crystal plasticity models are necessary to adequately predict the local strains, and hence the slip system activity needed to predict damage nucleation.
9. Damage nucleation depends upon the cohesive strength of the boundary, i.e. the energy needed to separate an existing interface—Griffith criterion.
10. Damage nucleation probability is proportional to local hydrostatic tensile stress.
11. Damage nucleation is more likely at triple lines than along boundaries, especially along U-lines.
12. Slip directions are more influential on damage nucleation than slip planes.
13. Low  $\Sigma$  boundaries are less likely to accumulate damage than random boundaries.
14. Twin boundaries resist damage because they repel dislocations from the boundary.
15. Twin boundaries resist damage because they allow efficient slip transfer.
16. Twin boundaries are schizophrenic (sometimes resistant, sometimes susceptible to damage nucleation).
17. Fatal flaws are located where there is the highest density of local damage sites.
18. Fatal flaws are located where the size of nucleated damage grows the fastest.

## 8. Numerical aspects associated with the CPFE method

### 8.1. General remarks

As far as the FE method is concerned, CPFE approaches can be regarded as a class of constitutive material models. Therefore, they can be implemented directly into an FE code when it is available in source form. In the case of commercial FE codes, CPFE constitutive laws are implemented in the form of a user subroutine, e.g. HYPELA2 in MSC.Marc [388] or UMAT/VUMAT in Abaqus [389]. Depending on whether the FE code is implicit or explicit, the purpose of a material model is one- or twofold: (i) calculate the stress  $\sigma$  required to reach the final deformation gradient (implicit and explicit); (ii) calculate the Jacoby matrix  $\mathbf{J} = d\sigma/d\mathbf{E}$  (implicit only,  $\mathbf{E}$  is the symmetric strain tensor).

The stress calculation is usually implemented using a predictor–corrector scheme. Fig. 23 visualizes the set-up of the clockwise loop of calculations to be performed. In principle, one could start predicting any of the quantities involved, follow the circle and compare the resulting quantity with the predicted one. Subsequently the prediction would be updated using, for instance, a Newton–Raphson scheme. Various implementations were suggested, using either the elastic deformation gradient  $\mathbf{F}_e$  [390], the plastic deformation gradient  $\mathbf{F}_p$  [391], the second Piola–Kirchhoff stress  $\mathbf{S}$  [109] or the shear rates  $\dot{\gamma}^\alpha$  [84] as a starting point.

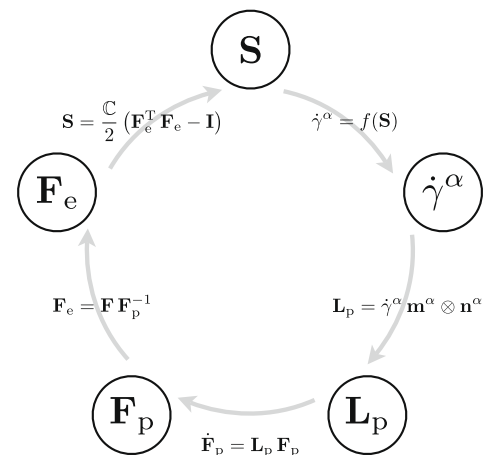


Fig. 23. Clockwise loop of calculations during stress determination. ( $\mathbf{S}$  second Piola–Kirchhoff stress,  $\dot{\gamma}^\alpha$  shear rate,  $\mathbf{L}_p$  plastic velocity gradient,  $\mathbf{m}^\alpha$  slip direction,  $\mathbf{n}^\alpha$  slip plane normal,  $\mathbf{F}_p$  plastic deformation gradient,  $\mathbf{F}_e$  elastic deformation gradient,  $\mathbf{C}$  elasticity tensor,  $\mathbf{I}$  identity matrix).

While they certainly all should lead to the same results, there are two numerical aspects to consider: (i) the inversion of the Jacoby matrix occurring in the Newton–Raphson algorithm; (ii) the character of the equations to evaluate.

Regarding the first point, one has to realize that the dimension of the Jacoby matrix is equal to the number of independent variables of the quantity that is used as predictor. These are nine variables for  $\mathbf{F}_e$ , eight for  $\mathbf{F}_p$  (due to volume conservation) and six for  $\mathbf{S}$  (due to the symmetry of the stress tensor). However, if the  $\dot{\gamma}^\alpha$  are chosen, there are at least 12 variables (slip systems in fcc crystals), up to 48 (slip systems in bcc crystals), or even more in the case of additional twinning. Inverting such large matrices (i.e.  $48 \times 48$ ) is numerically quite demanding, which is the reason why such implementations require some effort in reducing the number of (active) slip systems [392].

The second point concerns the numerical convergence behavior of the overall system. When starting an iteration from any other quantity than  $\dot{\gamma}^\alpha$ , the procedure involves calculating the slip rates from the stress. This is usually done using a power or exponential law. The slope of these functions is rapidly increasing, i.e. small variations in stress lead to increasingly larger deviations in the strain rate. Therefore, for large deformations, where convergence becomes a main issue, the iteration behavior of the stress loop becomes worse. However, when starting from  $\dot{\gamma}^\alpha$ , the inverse tendency applies, i.e. stress variations with varying shear rates get smaller and smaller. This is why the second approach promises a better numerical stability at large strains, at the cost, however, of dealing with a large Jacoby matrix.

### 8.2. Explicit vs. implicit integration methods

When discussing explicit vs. implicit integration schemes one has to distinguish between two aspects. Firstly, the FE

solver can follow an explicit or implicit approach, and secondly the material model can be iterated using explicit or implicit integration schemes. Concerning the first point, Harewood and McHugh [182] recently compared the efficiency of both methods when applying crystal plasticity models to forming problems. As could be expected, to some extent the outcome of this comparison is problem-dependent. As a rule the explicit scheme generally seemed favorable when contact is involved.

Regarding the material model itself, e.g. the material subroutine in the case of commercial FE solvers, anything from explicit to fully implicit integration methods is possible. The task of the material model is twofold. Firstly, the stress necessary to achieve the prescribed deformation has to be determined. Secondly, the material state has to be updated. In most codes first the stress is determined implicitly for a fixed state of the material and in a subsequent step the material state is updated. In the case of a fully implicit implementation the stress then has to be determined again until convergence is achieved, while in a semi-implicit code the calculation is stopped after the state was updated. An advantage of the fully implicit scheme is that it truly converges to the correct solution (if it converges at all), whereas the explicit solution converges generally but not necessarily to the correct solution. Since explicit schemes typically use very small time steps, semi-implicit integration schemes should generally work satisfactorily with respect to precision, while they are at the same time faster than a fully implicit scheme.

### 8.3. Element types

CPFE constitutive models as introduced in Section 4 are formulated in a tensorial way to account for material anisotropy. Therefore, they are based on a 3-D stress tensor. In terms of FE design this means that crystal plasticity works best for 3-D models and, when used for 2-D models, is restricted to plane strain boundary conditions. However, it does not work for plane stress boundary conditions.

Most CPFE simulations use linear elements, i.e. elements using linear interpolation functions for the displacements. Therefore, these elements cannot describe strain gradients within one element. When the resolution of the FE mesh is reasonably fine, this can be tolerated for single-phase materials. However, when strong strain gradients occur, either due to boundary conditions or due to the presence of multiple phases, linear elements are usually not sufficient to correctly capture these strong gradients. In such cases higher-order elements should be used.

In cases with advanced CPFE material models, such as introduced in Section 4.3.2, that include strain gradients, the situation becomes more complicated. The standard element formulations are only continuous in the displacements ( $C_0$ -continuous). This implies that strains can be calculated as displacement gradients, but strain gradients might be undefined. To overcome this problem one has to use enhanced element formulations as in Evers et al.

[26], Arsenlis et al. [9]. However, the definition of boundary conditions becomes rather complicated in the case of complex loadings for such element formulations. Therefore, many authors still use standard elements for such simulations and derive the necessary gradients from multi-element patches as described, for example, in Han et al. [393].

## 9. Experimental validation and application

### 9.1. Introduction

CPFE simulations can be validated by experiments in a detailed way, with respect to both mechanical and microstructure observables. Measures of the former group can be monitored in terms of forces, elastic stiffness (including spring-back effects), stresses, mechanical size effects, mechanical anisotropy, shape changes, hardness, strain paths, strain rates, and strains including local strain maps obtained by digital image correlation or speckle methods. Quantities based upon microstructure observations can be mapped in terms of crystallographic texture, grain shapes, dislocation substructures and densities, internal stresses, and surface roughness. Many such comparisons can be conducted one-to-one and at different scales (Table 2). In addition to these well-established methods, novel tomographic experiments allow one to compare CPFE predictions to real microstructures also in three dimensions, for instance by synchrotron orientation tomography [214,394], and EBSD tomography (3-D EBSD) [171,174,177,216,395,396]. Other new techniques to validate CPFE predictions are microscopic mechanical tests conducted on micrometer- or nanometer-sized samples prepared by electrochemical or focussed ion beam methods [397–400]. In this section we review a selection of some literature examples which document applications of the CPFE method from microscopic to macroscopic scales.

### 9.2. Microscopic and mesoscopic examples

#### 9.2.1. Orientation stability in aluminum under plane strain deformation

During plastic deformation crystals can gradually build up in-grain orientation scatter under gradient-free boundary conditions [92,110]. This phenomenon depends on the orientation, on neighbor grains and on the external boundary conditions (e.g. friction, tool alignment) [119,172,401,402]. Basically, the tendency for orientation stability can be expressed in terms of the divergence behavior of the reorientation field (which is sometimes also referred to as flow field) for an orientation under a given load [92]. Using CPFE simulations and classical homogenization theory it was found that the orientation stability (under plane strain loading) in aluminum (as an example of fcc material with high stacking fault energy) can fall into one out of three basic categories. The first group of orientations is stable and does not build up substantial in-grain orientation scatter even for minor variations in the initial orientation spread or in the



boundary conditions (e.g. change in the friction coefficient). Typically, such orientations show a very symmetric arrangement of the active slip systems. Their reorientation behavior is characterized by negative divergence of their reorientation field (for a given load tensor). They are stable and not prone to build up internal orientation scatter. Examples are the  $\{001\} [110]$  orientation in bcc crystals or the Goss orientation  $\{011\} [100]$  in fcc crystals under plane strain load (rolling, mid-thickness layer). Under shear load both texture components become unstable (warm rolling, subsurface layer or torsion). The second group is extremely unstable and builds up strong in-grain orientation scatter. These orientations show positive divergence of the reorientation field. Examples are the Goss orientation  $\{011\} [100]$  in bcc crystals and the rotated cube orientation  $\{001\} [110]$  in fcc crystals under plane strain load. When subjected to simple shear loads both texture components become stable and are hence referred to as shear components for the respective crystal structure [92,119,403]. Crystals that fall into the third category reveal very small divergence of their reorientation field which means that they have the same tendency for orientations changes as their neighborhood. Figs. 24 and 25 show an example of the stability of the cube orientation in fcc material exposed to plane strain load for different boundary conditions and different initial orientation spread. Similar CPFE simulations on the stability of cube grains were also conducted by Bate [155].

### 9.2.2. Texture and dislocation density evolution in a bent single-crystalline copper-nanowire

This section presents an investigation of a bending test using experiments and CPFE simulations. A 23  $\mu\text{m}$  long single-crystalline copper nanowire was produced by focused ion beam fabrication (FIB) [176]. The average cross-section of the specimen was  $750 \times 750 \text{ nm}^2$ . The nanowire was bent in situ using a micromanipulator. Char-

acterization was done using scanning electron microscopy (SEM) and electron backscatter diffraction (EBSD). The experiment was compared to simulations conducted by a CPFE analysis using a dislocation density-based constitutive hardening law [23,24,174]. The simulations were required for studying the influence of the boundary conditions on the results since they can have substantial influence on the evolution of the texture during bending. The simulations and the experimental results reveal good agreement in terms of texture evolution and elastic spring-back as long as the boundary conditions were reflected accurately. The model provides information about the microstructure evolution in terms of particular material parameters such as the evolution of the dislocation density (Fig. 26). Similar CPFE simulations on the deformation of pillars by micro-scale compression tests were presented by Raabe et al. [172]. The motivation for selecting this example is to document the capability of the CPFE approach to yield good texture predictions even at small scales where the constitutive law, which is built on a statistical dislocation model [23,24,404], reaches its limits due to the small size of the elements.

### 9.2.3. Texture and microstructure underneath a nanoindent in a copper single crystal

This example concerns the origin of deformation-induced orientation patterns below nanoindents in a  $\{111\}$ -oriented copper single crystal. The experiments and the simulations were conducted using a conical indenter with spherical tip [170,171]. The patterns were characterized by neighboring crystalline zones with opposite rotations rates. The approach to analyze and understand the phenomenon was as follows. First, the deformation-induced orientation patterns were investigated in 3-D using a high-resolution tomographic EBSD technique [174,177]. This method works by a fully automated alternating serial sectioning

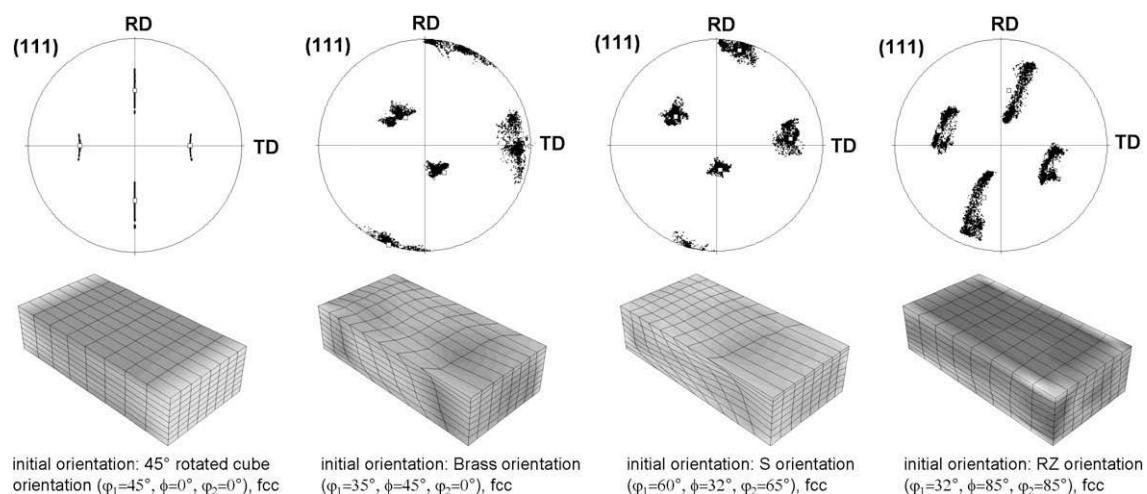


Fig. 24. Accumulated misorientations in gray scale coding (light values indicate large misorientations) for aluminum grains together with  $\{111\}$  pole figures after 50% plane strain deformation for different orientations. The simulations used 12 slip systems. The open squares in the pole figures show the initial orientation (which was the same at all integration points) and the black dots show the orientations after the deformation.

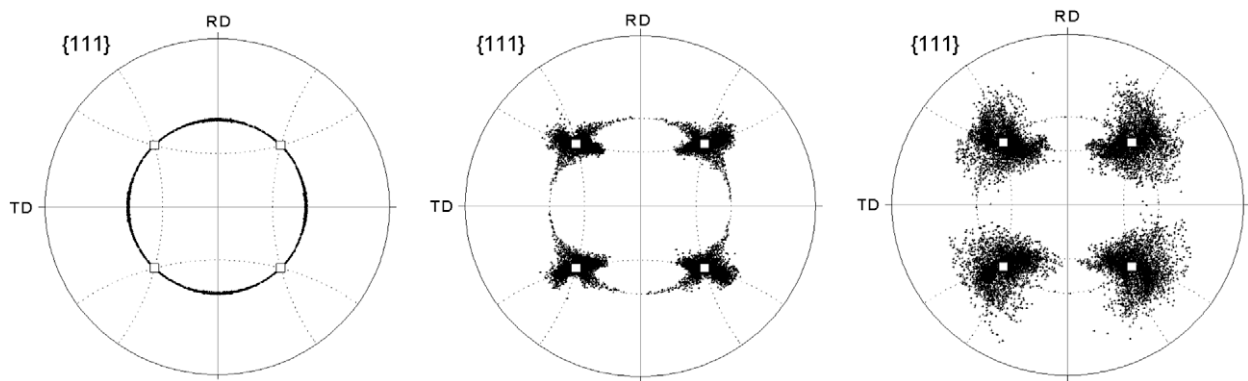


Fig. 25. Orientation stability of cube orientation after 50% plane strain compression for different internal and external boundary conditions predicted by CPFE simulations. Left: starting condition—exact cube orientation without initial orientation scatter, Coulomb friction coefficient 0.1. Center: starting condition—cube orientation with 2.5° initial orientation scatter, Coulomb friction coefficient 0.1. Right: starting condition—cube orientation with 2.5° initial orientation scatter, Coulomb friction coefficient 0.3.

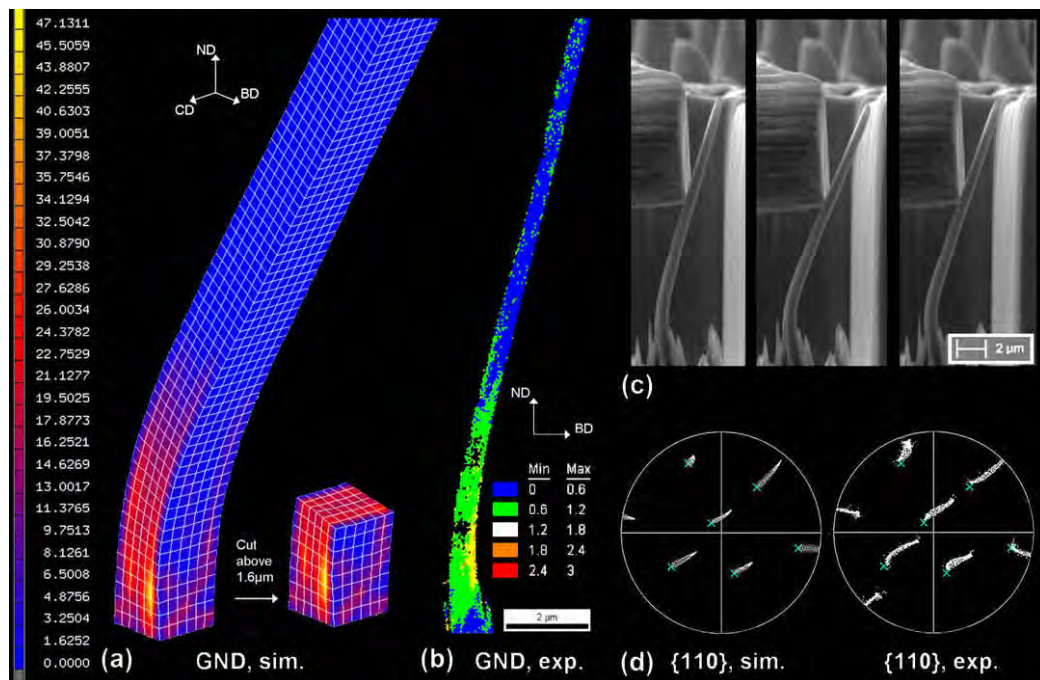


Fig. 26. (a) Predicted density of the GNDs during nanowire bending in units of  $\mu\text{m}^{-2}$ . (b) Experimentally determined GND density, quantified in terms of the average local orientation gradient determined via high-resolution EBSD. (c) Subsequent scenes taken during bending. (d) Pole figures of the bent nanowire obtained from experiment and simulation. The predictions were used to determine the exact boundary conditions that occurred during testing. The crosses indicate the initial orientation. CD, cross direction; BD, bending direction.

and EBSD mapping procedure in a SEM-FIB set-up (3-D EBSD) [216,395,396]. Second, the problem was modeled using a CPFE method which is based on a constitutive model that uses dislocation densities as state variables [23,405]. It was found that the rotation pattern induced during indentation were well predicted by the CPFE model. The change of the crystal rotation directions could be explained by the different slip system combinations that were activated due to the geometry of the indenter causing a gradual change in the loading axis that evolved differently at different locations during indentation (Fig. 27).

#### 9.2.4. Application of a non-local dislocation model including GNDs to shear tests of aluminum single crystals

The non-local dislocation-based CPFE constitutive model presented in Section 4.3 was implemented in the commercial FE code MSC.Marc200x using the subroutine HYPELA2 [388]. The model includes GNDs. The predictions of this non-local model were compared to simple shear experiments on commercially pure aluminum single crystals and to conventional viscoplastic CPFE simulations (Fig. 28) [24,98,406].

In the experiments the maximum equivalent deformation is always observed in the lower left corner of the single

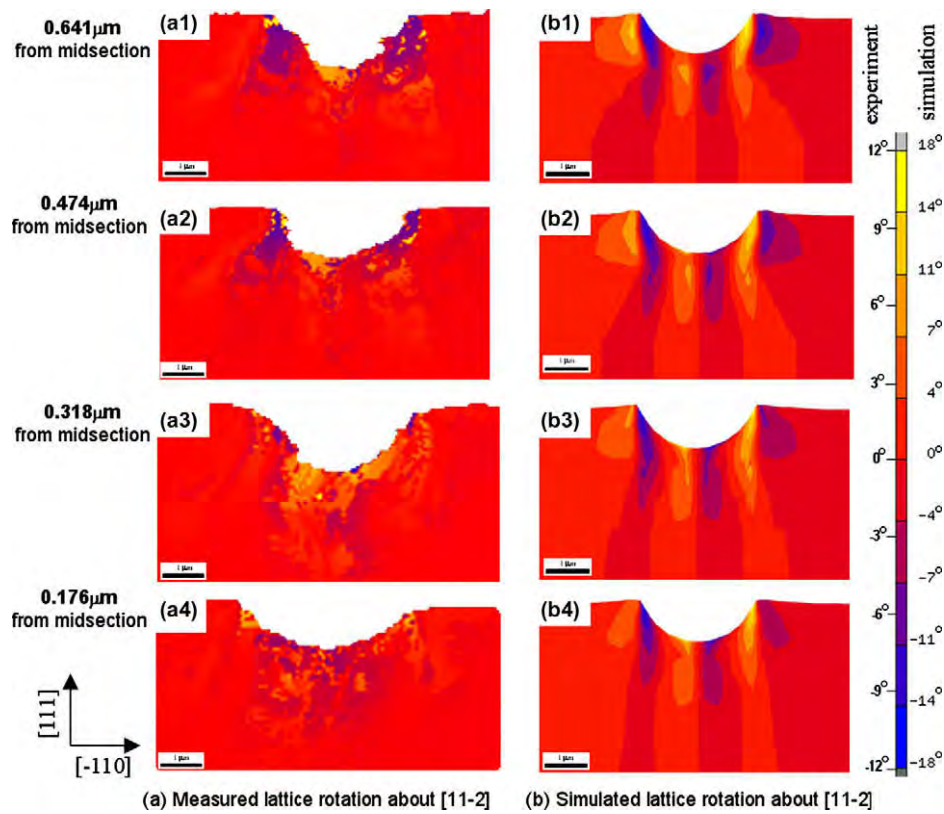


Fig. 27. Comparison between crystal rotation about the direction  $[1\ 1\ \bar{2}]$  in the sample reference system underneath the indent at different sections between experiment and simulation (positive values indicate counter-clockwise rotation) [171,174,177].

crystal and extends diagonally across the crystal. While this behavior is correctly reproduced by the non-local approach the phenomenological viscoplastic model predicts the highest strains in the upper left corner of the specimen. One can assume that the better prediction yielded by the non-local model is mainly a consequence of the physically based latent hardening law and the introduction of the GNDs. This assumption is supported by the data presented in Fig. 30b which reveal that substantial densities of GNDs are generated close to the sample borders. For better comparison of the relative contributions of the two types of dislocations, Fig. 30b and c show both the distributions of the GNDs and the densities of statistically stored dislocations on the crystal surface.

Another advantage of the use of GNDs in a CPFE constitutive law is that the model is rendered length scale dependent. Therefore, the shear simulation presented above was repeated for a set of three cases which were characterized by different height-to-length ratios. For this purpose the height  $H$  of the sheared sample was changed to one-half and one-tenth of the original height  $H_0$ , respectively. The resulting shear stress–shear strain curves are shown in Fig. 29. Eqs. (26), (27), (38), (39) reveal that the GND density contributes to the passing stress and to the multiplication term of the immobile dislocation. For this reason one would expect higher predicted stresses for the thinnest sample owing to the relative increase of zones

which are mechanically affected by the presence of interfaces. This is indeed confirmed by Fig. 29. Fig. 30b, e, and h show how the relative size of the zone that is influenced by the GNDs increases with decreasing sample height. This increased GND density leads also to an increase in the statistically stored dislocation density as expected and shown in Fig. 30c, f, and i. Additionally, Fig. 30a, d, and g reveal that the predicted texture evolution of the crystal is affected by the non-local model. This results in an intersection of the stress–strain curves for  $H = H_0$  and  $H = H_0/2$  in Fig. 29. The strong influence of incorporating GNDs into the CPFE framework on the predicted reorientation rates is due to the penalty effect they impose. This means that each reorientation step which introduces an orientation divergence with respect to the neighborhood [117] is impeded owing to the corresponding introduction of additional GNDs.

#### 9.2.5. Evolution of crystallographic dislocation density in a crystal plasticity modeling framework

Arsenlis and Parks implemented dislocation-based constitutive laws into a CPFE simulation framework [19]. The basics and further developments along these lines were published in a sequence of works where the recent emphasis is placed on extracting constitutive information, for instance, on strain hardening from discrete dislocation modeling [9,18,19,65]. They suggested a constitutive for-



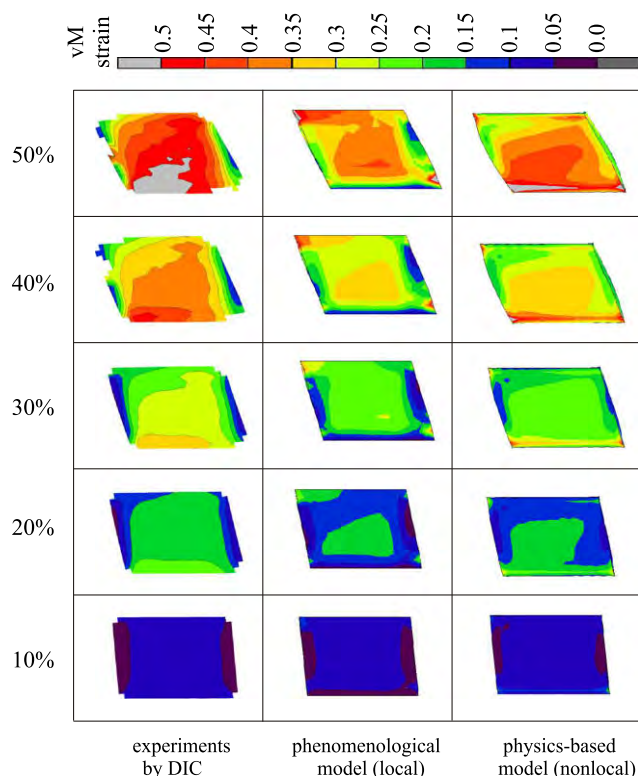


Fig. 28. Comparison of the von Mises equivalent strain on the surface of an aluminum single crystal (3.1 mm long, 2.0 mm thick and 2.2 mm high) for a simple shear test. The left column shows experimental results obtained by strain measurements via digital image correlation (DIC). The central column shows results obtained by using a conventional viscoplastic formulation. The right column shows results obtained by using an enhanced non-local model (see Section 4.3) which considers GNDs.

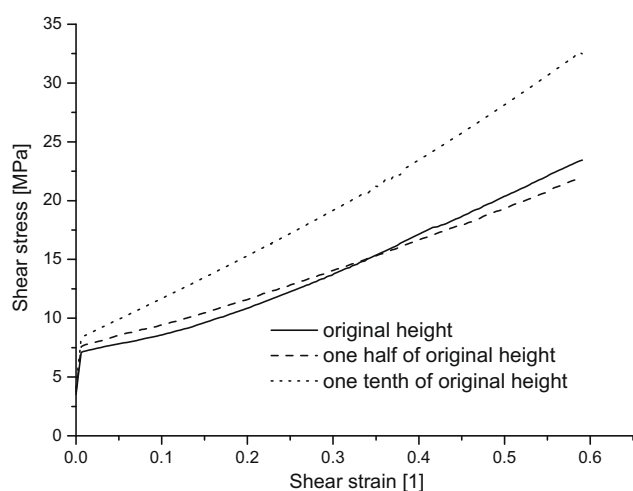


Fig. 29. Simulated shear stress–strain curves for samples with different height-to-length ratios, demonstrating the size sensitivity of the non-local dislocation model.

mulation where dislocation density variables gradually evolve from initial conditions according to a set of structure evolution formulations considering basic dislocation mechanics, such as the continuity of dislocation line and

Burgers vector conservation in a set of generic multiplication and annihilation processes [19]. The density evolution equations use three classes of internal variables, namely the average dislocation mobility, the average segment length and the capture radii. The model used a set of 18 discrete dislocation densities comprising 12 edge and 6 screw components.

The model was implemented in a CPFE framework to study the polyslip behavior of aluminum single crystals of different initial crystallographic orientation under tensile loading (Fig. 31). The results do not only yield reasonable mechanical stress–strain response for the differently oriented crystals, but also provided insight about the development of the dislocation structure responsible for the respective plastic behavior observed. A similar approach where conventional viscoplastic hardening rules were replaced by dislocation density evolution laws including also GNDs was suggested by Ma et al. [23–25,404].

#### 9.2.6. Application of a grain boundary constitutive model in CPFE bicrystal simulations

This example presents the use of a dislocation-based constitutive model to incorporate the mechanical interaction between mobile dislocations and grain boundaries into the CPFE framework. The approach is based on the introduction of an additional activation energy into the rate equation for mobile dislocations in the vicinity of grain boundaries. The energy barrier is derived by using an elastic model for thermally activated dislocation penetration events through grain boundaries. The model was presented in detail in Section 4.3.3 and in [24,25]. The approach is applied to the case of 50% (frictionless) simple shear deformation of three aluminum bicrystals with a small-, intermediate- and high-angle grain boundary, respectively, parallel to the shear plane. The simulations are compared to experiments with respect to equivalent surface strain and texture. The constitutive parameters were fitted by using the stress–strain response of a single-crystal simple shear test illustrated in Figs. 28 and 29.

Figs. 32–34 show the comparison of the von Mises strain patterns obtained from the experiment (left column), from the simulation with a viscoplastic law (no interface model; center column), and from the dislocation-based CPFE simulation including GNDs and a geometrical model for the grain boundary resistance as introduced in section 4.3.3 (right column). The figures show the von Mises strain distributions for five stages of shear with a constant increase of 10% per load step. The experiments reveal in all cases the strong constraint imposed by the grain boundary. Even for the small-angle grain boundary (7.4°) the experiment indicates strain separation among the two crystals. With increasing grain boundary misorientation, the heterogeneous distribution of the strain between the grains becomes more pronounced. The corresponding viscoplastic CPFE simulation (local law, central column of Figs. 32–34) does not adequately reproduce the influence of the grain boundaries on the strain distribution. This applies in particular



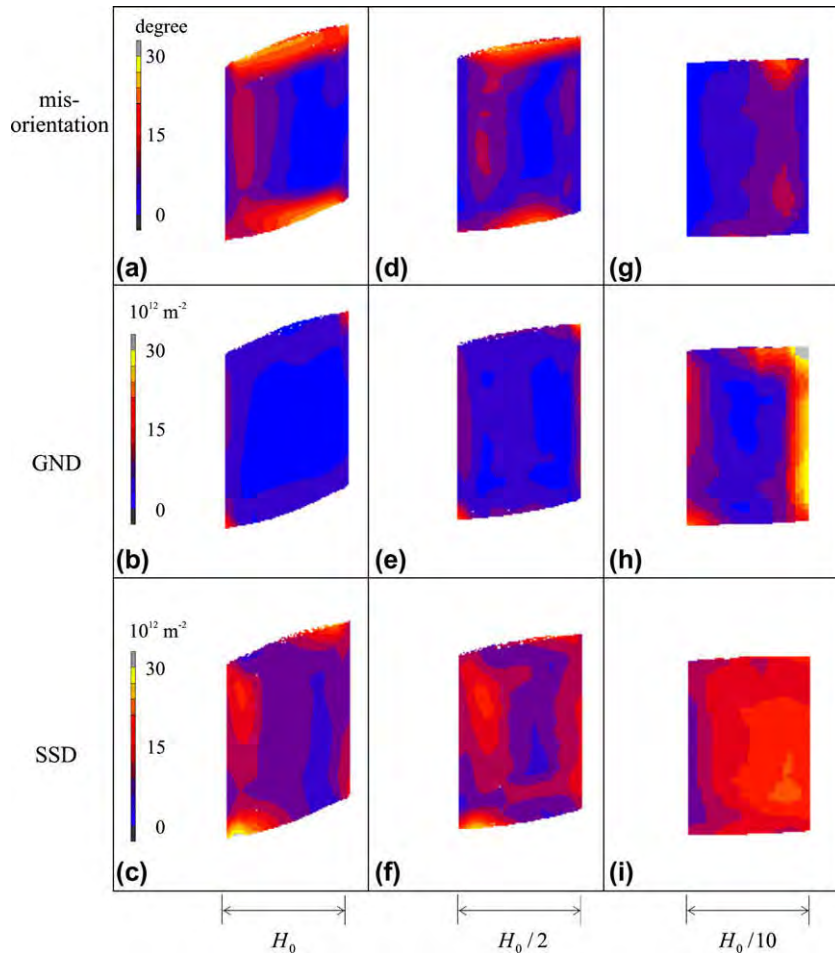


Fig. 30. Comparisons of dislocation densities and misorientation for different samples after a 30% shear deformation. Heights of samples are  $H = H_0$ ,  $H = H_0/2$  and  $H = H_0/10$  (all plots are scaled to the same height for a better comparison), respectively. GND, geometrically necessary dislocation density; SSD, statistically stored dislocation density.

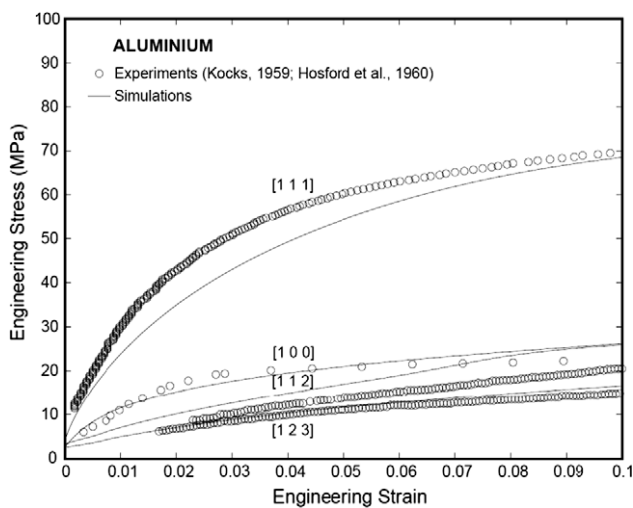


Fig. 31. CPFE simulated and experimentally observed orientation dependence of the stress-strain profile of aluminum single crystals during tensile loading [19].

for the two bicrystals which have a small- and intermediate-angle grain boundary, respectively. For the bicrystal

with the high-angle grain boundary (Fig. 34), the empirical (local) model is capable of predicting some, although not all, characteristics of the strain separation between the two crystals. The partial success of the simulation with the empirical viscoplastic hardening law in the case of the high-angle grain boundary is attributed to the strong effect of the change in the Schmid factor across the interface, i.e. kinematic effects prevail over dislocation density effects in this case.

Bate [155] conducted a similar CPFE simulation of bicrystal deformation. He observed not only orientation splitting and strain separation among the abutting grains but also severe deformation banding in both crystals at an oblique angle to the grain boundary. This work demonstrates very nicely the far reaching effect of a grain boundary causing substantial deformation heterogeneity in the grain interior.

#### 9.2.7. Modeling of the grain size dependence of polycrystal mechanics

The group of Evers, Brekelmans and Geers investigated the way that size dependent effects are associated with

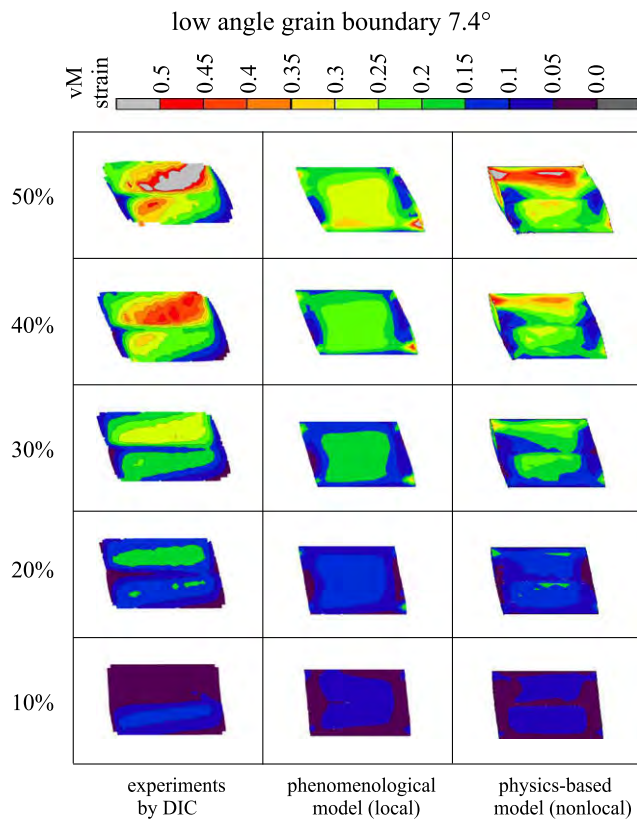


Fig. 32. Simple shear test of a bicrystal with a  $7.4^\circ$  low-angle grain boundary (3.1 mm long, 2.0 mm thick and 2.2 mm high). Comparison of the von Mises strain patterns as obtained from the experiment via digital image correlation (DIC, left column), from the simulation with a conventional viscoplastic constitutive law (central column), and from the simulation which uses an advanced dislocation-based non-local model (see Section 4.3) (right column).

interfaces and GNDs in CPFE and Taylor-type homogenization frameworks [20,21,26,83]. For instance in [20], a local plastic strain-gradient-dependent crystal plasticity model was suggested which is capable of describing the grain-size-dependent mechanical response of polycrystals.

This approach consists of assigning GND populations to intragranular incompatible deformations that arise as a result of the existence of grain boundaries between abutting crystals. The polycrystal appears in this model as a statistical set of bicrystal aggregates which altogether provide an orientation-dependent density of misfit dislocations, which in turn provide extra hardening to the system. As the intragranular heterogeneous deformation is related to the grain size, the amount of GND-enhanced hardening grows as the crystal size drops (Fig. 35).

The conventional slip system hardening through statistically stored dislocations is described by a system of phenomenological equations that capture the influence of self- and latent hardening. The model provides a crystallographically and physically motivated hardening dependence in polycrystals based on their grain size. The morphological texture can be incorporated through the inclination and crystallographic distribution of the grain boundaries and their mutual weights.

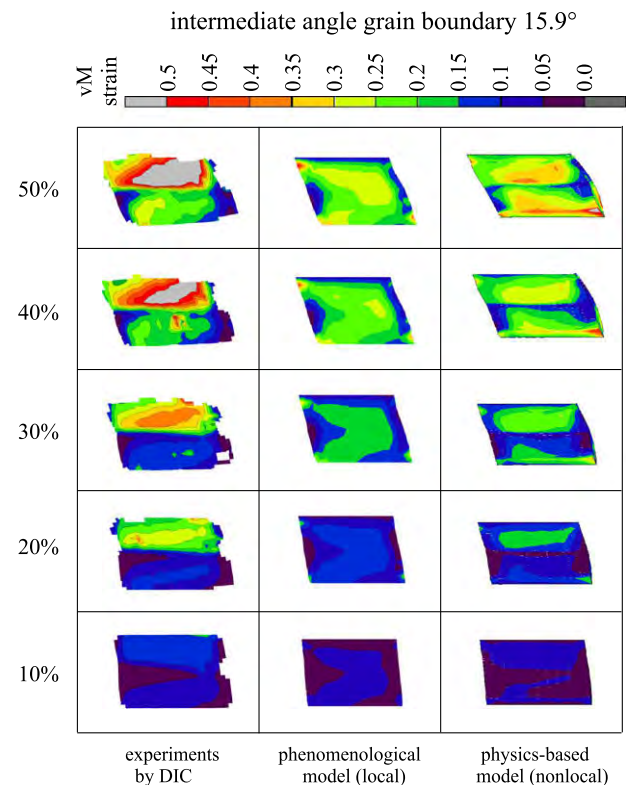


Fig. 33. Simple shear test of a bicrystal with a  $15.9^\circ$  intermediate-angle grain boundary (3.1 mm long, 2.0 mm thick and 2.2 mm high). Comparison of the von Mises strain patterns as obtained from the experiment via digital image correlation (DIC, left column), from the simulation with a conventional viscoplastic constitutive law (central column), and from the simulation which uses an advanced dislocation-based non-local model (see Section 4.3) (right column).

### 9.2.8. Three-dimensional aspects of oligocrystal plasticity

Zhao et al. [32] conducted a study of plastic strain localization and deformation-induced surface roughening in an aluminum polycrystal consisting of a small set of coarse grains (oligocrystal). A dog-bone specimen is plastically deformed under uniaxial tensile loading. During deformation, the history of strain localization, surface roughening, microstructure and in-grain fragmentation is recorded. Using a CPFE model, corresponding one-to-one high-resolution simulations are conducted (Fig. 36). The study reveals that the grain topology and microtexture have a significant influence on the origin of strain heterogeneity. Moreover, it suggests that the final surface roughening profiles are related both to the macrostrain localization and to the intra-grain interaction. Finally slip lines observed on the surface of the samples are used to probe the activation of slip systems in detail.

Particular attention in the analysis is placed on the ability of the CPFE model to capture the fine details of the surface roughening effects, orientation-dependent strain localization, and the pattern of activation of slip systems in the grains. It was observed that the grain stretching over the whole width of the dog-bone specimen was remarkably soft. The absence of dislocation barriers provided by grain

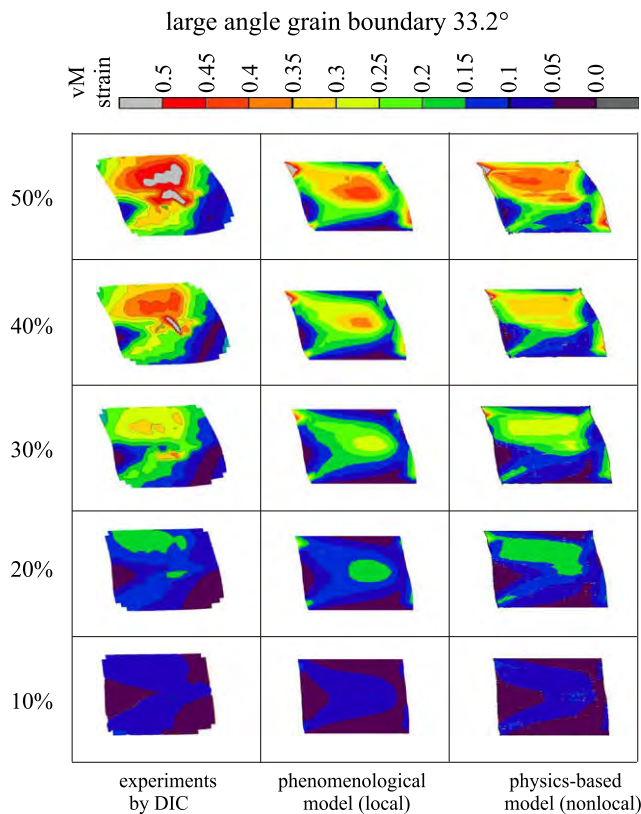


Fig. 34. Simple shear test of a bicrystal with a  $33.2^\circ$  high-angle grain boundary (3.1 mm long, 2.0 mm thick and 2.2 mm high). Comparison of the von Mises strain patterns as obtained from the experiment via digital image correlation (DIC, left column), from the simulation with a conventional viscoplastic constitutive law (central column), and from the simulation which uses an advanced dislocation-based non-local model (see Section 4.3) (right column).

boundaries promotes strain localization owing to a single isolated soft grain. Due to the significant thickness reduction, a severe surface roughening is particularly observed in the soft region of the sample.

Similar studies on the mechanical heterogeneity and the texture evolution in coarse-grained samples were presented by [14,110]. Common to these works is that they show,

depending on grain orientation, substantial in-grain orientation fragmentation and strain localization.

Beaudoin et al. [110] idealize in their study a simple polycrystal as a 3-D arrangements of eight grains, each consisting of many elements per crystal. Non-uniform deformations within individual grains lead to the development of domains that are separated by boundaries of high misorientation. Also, localized shearing is seen to occur at the microscopic grain scale. The authors also discuss the importance of such plastic and orientation localization phenomena for recrystallization nucleation (see also next section). In particular, the landmark paper of Beaudoin et al. [110] motivated further investigations on in-grain orientation scatter (grain fragmentation) and corresponding approaches to classify grains according to their kinematic stability upon loading. The aim of these works was to systematically learn which types of grains (texture components) tend to build up large orientation gradients under certain loading states [92,117] (Fig. 37).

#### 9.2.9. Simulation of recrystallization using CPFE micromechanical results

In this section we present approaches for predicting primary static recrystallization and related grain-coarsening phenomena by combining CPFE simulations with Monte Carlo, cellular automaton or network models [148,155,156,159,162,163,407]. Such combined methods can predict microstructures and texture evolution during thermomechanical treatment. The advantage of the approach is that they consider the material heterogeneity of the deformation microstructure and recrystallization phenomena as opposed to classical statistical approaches which are based on the assumption of material homogeneity.

Bate [155] assumed that the von Mises stress obtained from a CPFE bicrystal model is linearly related to the substructure density in deformed metals that undergo extensive dynamic recovery. From the CPFE results he constructed a cell structure and used it as input to a 2-D network model for recrystallization simulation. Cell centers are included at random coordinates, with specific exclusion rules to ensure that the cell size is inversely proportional to

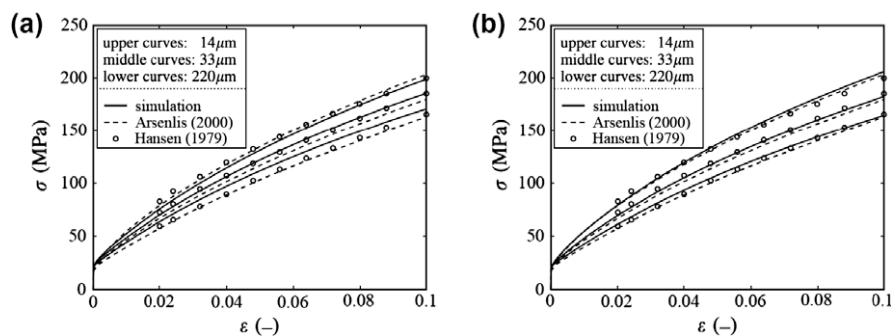


Fig. 35. Stress–strain curves for average grain diameters of 14, 33 and  $220\ \mu\text{m}$ , represented by the upper, middle and lower slide line curves (of each type), respectively. The dashed lines indicate results from earlier FE calculations of Arsenlis and Parks [18] and the bullets are experimental results from Hansen [1979]. (a) Results using the assumption of SSD and GND strength addition. (b) Results using the assumption of SSD and GND density addition [20], showing a closer agreement with experimental data.



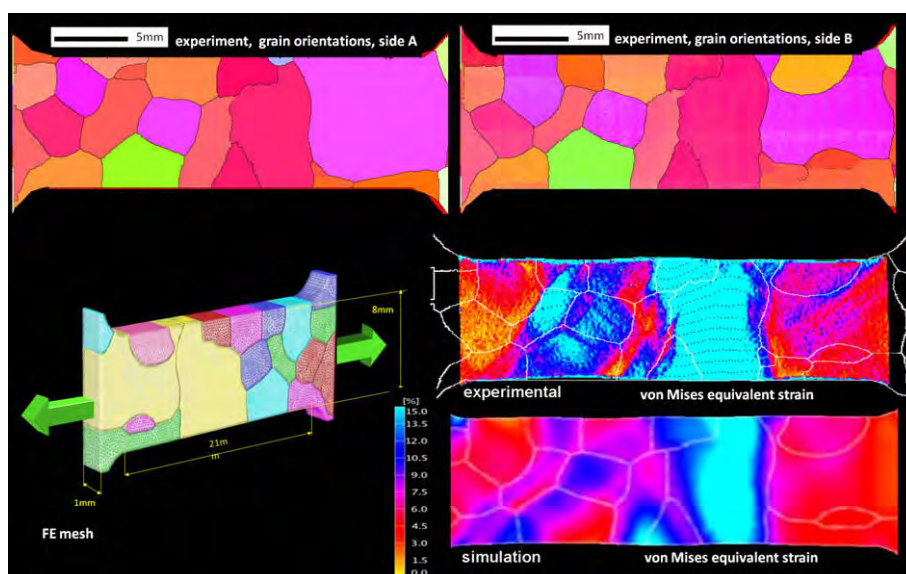


Fig. 36. Study by Zhao et al. on plastic strain localization and deformation-induced surface roughening in a 3-D aluminum polycrystal consisting of a small assembly of coarse grains (oligocrystal) [32].

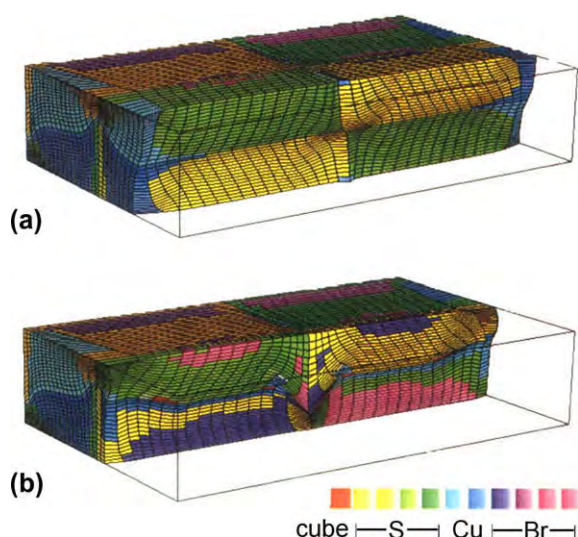


Fig. 37. Simulation of Beaudoin et al. of a grain cluster consisting originally of S-oriented crystals (fcc). Results are shown after a thickness reduction of 85%: (a) section with stable S orientations; (b) section with cube bands. Images are scaled by a factor of 10 in the thickness ( $N$ ) direction [110].

the local von Mises stress. Cell orientations are interpolated from the CPFE results and the initial network is set up via Dirichlet tessellation. Fig. 38 reveals two stages in the simulation. At an early phase of annealing, the essential features of the deformed structure remain apparent. The crystallite size is larger, and more high-angle grain boundaries emerge, near the original grain boundary. There are some high-angle boundaries associated with the deformation inhomogeneity in the upper grain. At the later stage, considerable strain-induced boundary migration has occurred. Some of the new grains have orientations corresponding to a cube texture rotated by  $15^\circ$  about the extension direction (circled points in Fig. 38).

Raabe and Becker used a method in which the results of a CPFE simulation serve as a starting microstructure for a subsequent discrete cellular automaton recrystallization simulation. The CPFE model simulated plane strain compression of aluminum with a columnar coarse grain structure to a total logarithmic strain of 0.434 [156,408]. The values of the state variables (dislocation density, crystal orientation) given at the integration points of the FE mesh were mapped on the cellular automaton lattice. The original size of the specimen which provided the input microstructure to the CPFE simulation gave a lattice point spacing of  $61.9 \mu\text{m}$ . The maximum driving force in the region arising from the stored dislocation density was about 1 MPa. The annealing temperature was 800 K. High-angle grain boundaries were characterized by an activation energy for the mobility of 1.3 eV. Small-angle grain boundaries were assumed to be immobile. The nucleation process during primary static recrystallization has been explained for pure aluminum in terms of discontinuous subgrain growth. According to this model nucleation takes place in areas which reveal high misorientations among neighboring subgrains and a high local driving force for curvature-driven discontinuous subgrain coarsening. The present simulation approach works above the subgrain scale, i.e. it does not explicitly describe cell walls and subgrain coarsening phenomena such as the approach of Bate [155]. Instead, it incorporates nucleation on a more phenomenological basis using the kinetic and thermodynamic instability criteria of classical recrystallization theory. Kinetic instability means that nucleation leads to the formation of a mobile high-angle grain boundary which can sweep the deformed matrix. Thermodynamic instability means that the stored energy changes across the new high-angle grain boundary give a net driving force. Nucleation in this simulation is performed in accord with these



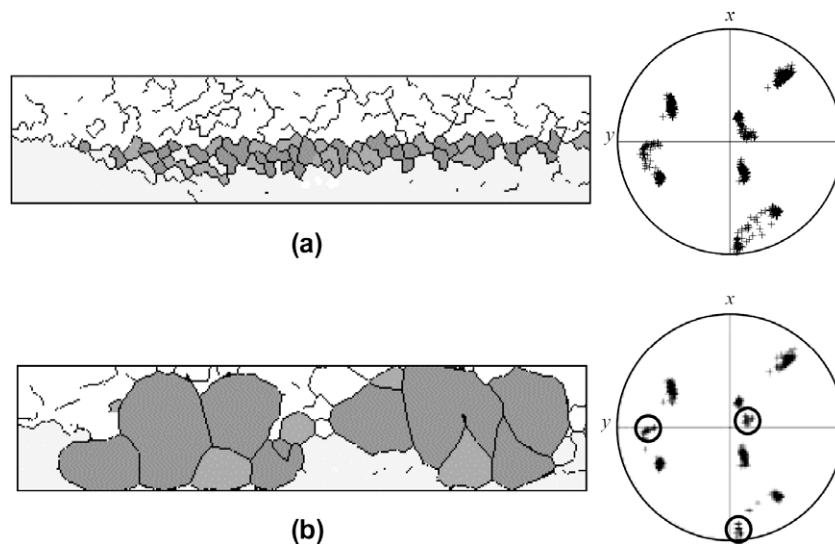


Fig. 38. Results of Bate from a network annealing model with the initial representation of microstructure derived from a CPFE simulation [155]. The initial number of crystallites was 900. Only grain boundaries with misorientations greater than  $3^\circ$  are shown. Darker grains are near the cube orientation. The configuration at 400 remaining crystallites is shown in (b). The resulting grain orientations are given in the {001} pole figure [155].

two criteria [408] (Fig. 39). A similar approach of applying a cellular automaton model to CPFE simulation data of a deformed superalloy for the prediction of local recrystallization phenomena was used by Zambaldi et al. [162] (Fig. 40).

#### 9.2.10. Simulations of multiphase TRIP steels

The mechanical behavior of a TRIP-assisted steel is simulated for an uniaxially loaded sample composed of a single austenitic grain surrounded by a matrix of ferritic grains. The purpose of the present simulation is to study the TRIP effect as a function of crystallographic orientations, i.e. the orientation of the austenitic and ferritic grains

with respect to the applied load as well as the orientation mismatch between neighboring grains.

In the present analysis, a cubic sample of size  $a^3$  (see Fig. 41) that represents a single grain of austenite surrounded by a matrix of ferrite is considered. In the undeformed state, the polyhedral austenitic grain occupies approximately 13% of the total volume of the sample. The sample is initially stress-free and is subsequently subjected to a uniaxial tensile loading, which is prescribed through the following boundary conditions. (i) The normal displacement and the tangential traction on the external faces 2, 3 and 5 are set to zero. (ii) The normal displacement on the external face 1 equals to  $u_1 = 10^{-4}at$ , with time

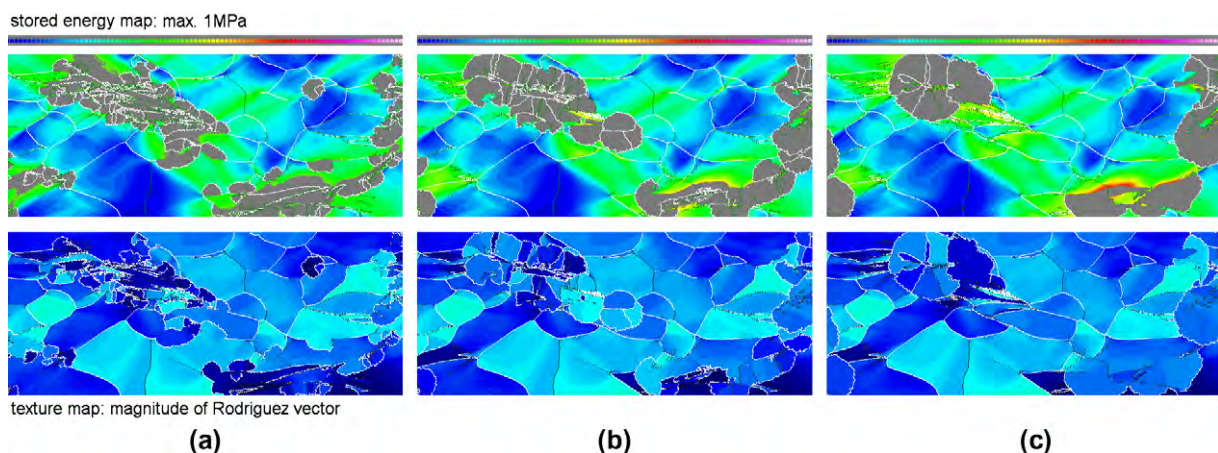


Fig. 39. 2-D simulation of recrystallization in deformed aluminum on the basis of CPFE data. Dislocation density in terms of the driving force (top) and microtexture (bottom) at an intermediate recrystallization step for different nucleation conditions. The texture is given in terms of the magnitude of the Rodriguez vector. The gray regions indicate recrystallization. The maximum occurring driving force is 1 MPa. The thick white lines indicate grain boundaries above  $15^\circ$ . The thin green lines indicate misorientations between  $5^\circ$  and  $15^\circ$ . The simulation parameters are: 800 K; thermodynamic instability criterion: site-saturated spontaneous nucleation in cells with at least 50% (a), 60% (b), and 70% (c), respectively, of the maximum occurring dislocation density (threshold value).

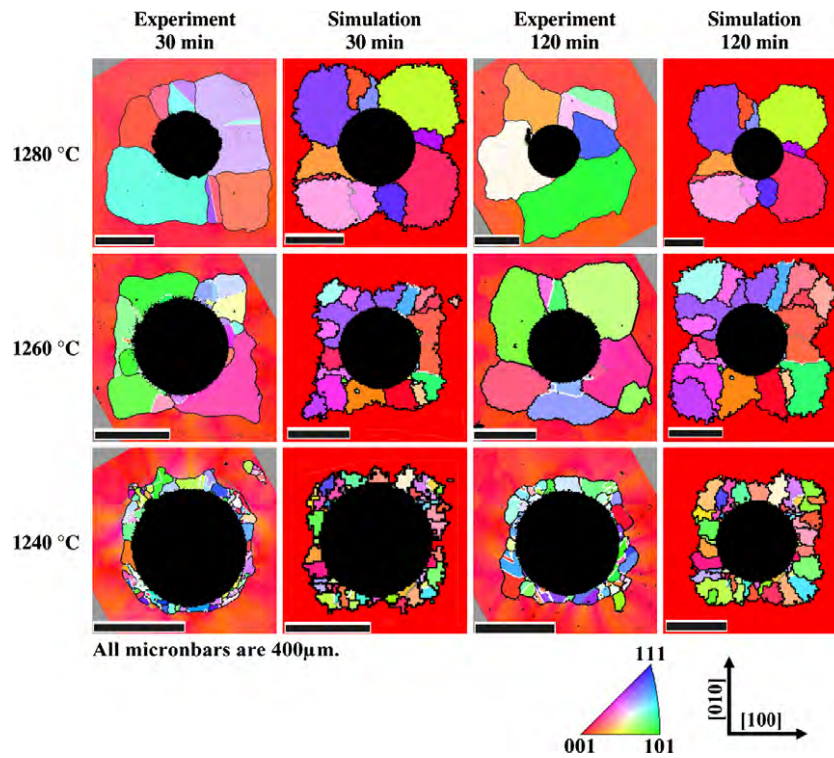


Fig. 40. Simulation results, showing evolving recrystallization microstructures around an indenter in a Ni-base superalloy, compared to EBSD measurements. The normal Miller indices are indicated in terms of an inverse pole figure color scheme. The arrows indicate the orientation of the parent single crystal. White lines in the experimental results indicate first-order annealing twins, black lines are used for high-angle grain boundaries with a misorientation of more than  $15^\circ$  [162].

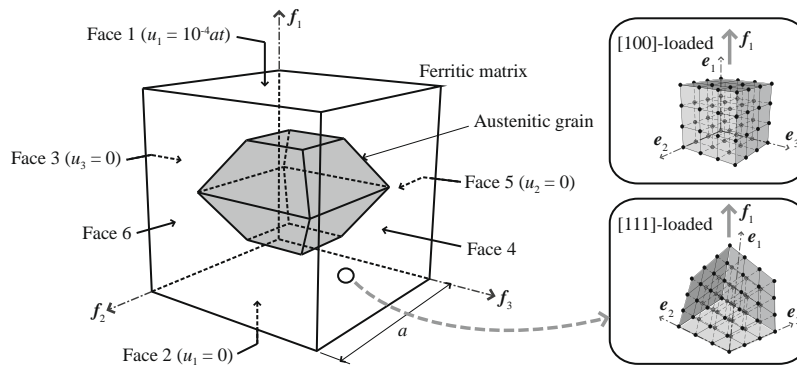


Fig. 41. A cubic sample representing a TRIP steel microstructure that consists of one grain of austenite in a ferritic matrix under uniaxial tensile loading.

interval  $0 < t \leq 2000$  s, and the tangential traction is set to zero. (iii) The remaining faces (4 and 6) are traction-free. The applied boundary conditions correspond to an axial straining rate of  $10^{-4} \text{ s}^{-1}$ . The simulation is performed at a constant temperature of 300 K. The parameters used in the model for the ferrite are the same as those used in [82], which are representative of a ferrite-based matrix in typical multiphase TRIP steels. The model parameters for the austenite are the same as those used in [82], which are calibrated from a TRIP steel with an austenite carbon concentration of 1.4 wt.%. In the simulations, four TRIP steel microstructures with different austenitic and ferritic crystallographic orientations (textures) are considered, namely (1)

$[100]_A-[100]_F$ , (2)  $[100]_A-[111]_F$ , (3)  $[111]_A-[100]_F$  and (4)  $[111]_A-[111]_F$ -loaded samples.

Figs. 42a and b illustrate the effective stress-strain response and the evolution of the austenitic volume fraction of the TRIP steel samples 1–4. In general, samples 2 and 4 (with  $[111]_F$ -loaded ferritic matrix) show a higher axial stress response than samples 1 and 3 (with  $[100]_F$ -loaded ferritic matrix), which indicates that ferrite loaded in  $[111]_F$  direction is stronger than that loaded in  $[100]_F$  direction (an analysis of the Schmid stress suggests that  $[111]_F$ -loaded ferrite gives the highest stress response under uniaxial tensile loading). Furthermore, samples containing a  $[111]_A$ -loaded austenitic grain give a relatively high initial

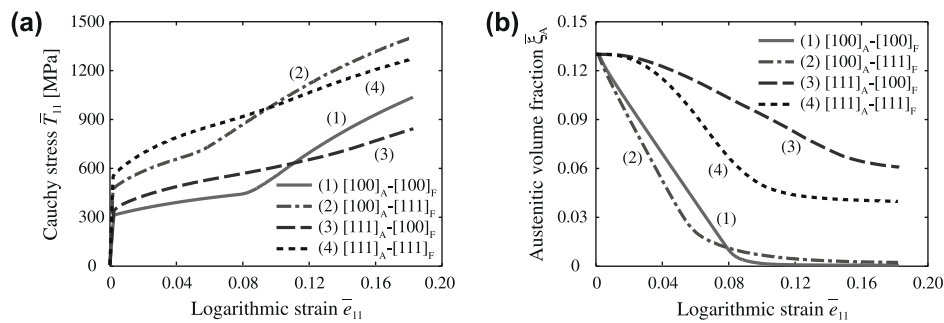


Fig. 42. Axial stress response (a) and the evolution of austenitic volume fraction (b) as a function of the axial logarithmic strain of TRIP steel samples consisting of an austenitic grain embedded in a ferritic matrix.

yield stress in comparison to the corresponding samples with a  $[100]_A$ -loaded austenitic grain. As reported in Refs. [78,82,263],  $[100]_A$ -loaded austenite is a more favorable orientation for transformation. In other words,  $[100]_A$ -loaded austenite transforms at a low stress level, whereas transformation of the  $[111]_A$ -loaded austenite occurs at a relatively high stress level. This is in agreement with experimental observations for TRIP steels (see e.g. [409,410]). In addition, the  $[100]_A$ -loaded austenitic grain (in samples 1 and 2) transforms at a higher rate than the austenitic grain loaded in  $[111]_A$  direction (samples 3 and 4), as depicted in Fig. 42b. At about 0.08 axial strain, the austenitic grain in samples 1 and 2 has been (almost) fully transformed into the harder martensitic phase. Consequently, the axial stress response of samples 1 and 2 increases rapidly after about 0.08 axial strain. Furthermore, Fig. 42b shows that transformation behavior in the austenitic grain is dependent not only on the orientation of the austenitic grain itself but also on the orientation of the surrounding ferritic matrix. The effect of the mismatch between the orientation of the transforming austenitic grain and the surrounding matrix can be quite significant (cf. e.g. samples 3 and 4).

#### 9.2.11. Evaluating CPFE results for damage prediction

At present, the fracture initiation parameter (*fip*) introduced in Section 7 is a static metric; an evolving *fip* has not yet been developed. However, it is clear that CPFE modeling provides the information necessary to evaluate an evolving *fip*. Preliminary CPFE modeling (using phenomenological hardening relationships) of one of the microstructures used to develop the *fip* showed greatly enhanced activation of the secondary twinning system responsible for the observed microcrack where it occurred (see Figs. 43 and 44). Only spatially resolved crystal plasticity could predict such a result. Remarkably, elements surrounding this boundary had only a modest stress-strain history (i.e. modest strain energy). The twinning system responsible for the crack appeared to geometrically accommodate a strain concentration that occurred on the other (upper left) side of grain 14. Thus, damage developed in response to a nearby local strain concentration at the left edge of grain 14, where strain transfer across a grain boundary some distance from the strain concentration led

to weakening of the boundary. This example suggests that while large local strains may be the ultimate driving force for damage, the failure event may not be nucleated where the large strains occur.

### 9.3. Macroscopic examples

#### 9.3.1. Using elastic constants from ab initio simulations for predicting textures and texture-dependent elastic properties of $\beta$ -Ti

This section presents applications on the prediction of textures and texture-dependent elastic properties using multiscale CPFE simulations where the elastic constants are obtained by ab initio simulations (density-functional theory) [411]. We apply this approach to binary Ti–Nb bio-material alloys that can be used for human implants. The two models we combine (ab initio, CPFE) work at very different length and time scales. The strength of this combination for predicting certain polycrystal properties lies in the fact that continuum-based theoretical models such as CPFE rely on a number of ground state properties (e.g. elastic tensor). The use of texture data is in such cases (elasticity) sufficient to predict realistic data also for complex polycrystalline aggregates irrespective of their thermomechanical process history. A particular advantage of using an FEM-based method rather than an analytical or semi-analytical approach for obtaining the polycrystal stiffness from corresponding ab initio single crystal data is that it allows one to consider any kind of crystallographic texture, including also intra- or in-grain interactions. Most homogenization methods for obtaining the elastic modulus of a polycrystal such as the Voigt, Reuss, Hill or Hershey [301,302,412,413] models usually either neglect texture or assume highly simplified boundary conditions. A further important aspect of using ab initio elastic results in conjunction with crystal mechanical simulations is the fact that for the elastic constants of single crystals (which are a necessary input to CPFE simulations) experimental data are often lacking [414,415]. Details about the ab initio calculations used in this section are given in [416].

The goal of the first example is to investigate the dependence of the rolling texture evolution of two  $\beta$ -Ti–Nb binary alloys on the elastic properties. For this purpose we



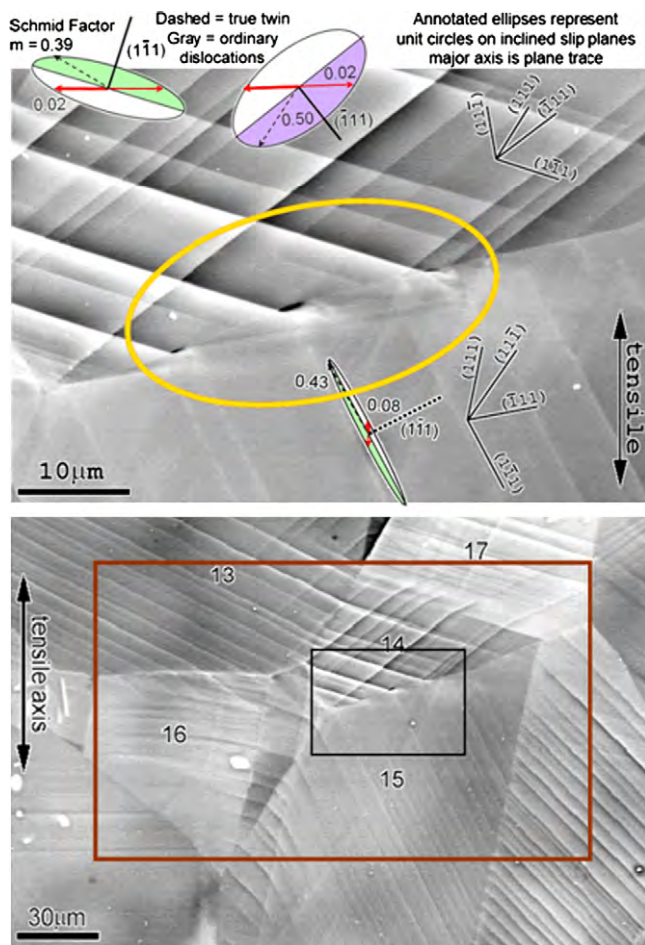


Fig. 43. Microcracks arising from twin interactions with a grain boundary in TiAl. Ellipses represent tilted unit circles on slip planes identified by poles, with slip or twinning vectors as indicated, with shaded half below the surface. Schmid factors are based upon the global (vertical) stress direction. The surrounding microstructure was modeled using CPFE.

used different elastic constants in terms of the magnitude of the tensor components and the elastic anisotropy. These elastic constants, which were obtained from ab initio electronic structure calculations [416], served as constitutive input variables in a CPFE simulation in conjunction with a viscoplastic hardening law [415].

$\beta$ -Ti alloys have bcc crystal lattice structure. At room temperature the structure can be stabilized by the addition of Nb or Mo. As slip systems we used  $\{110\}$ ,  $\{112\}$  and  $\{123\}$  slip planes, and  $\langle 111 \rangle/2$  Burgers vectors [417,418]. Two alloys were investigated, namely Ti–18 at.%Nb and Ti–31 at.%Nb. The elastic constants for Ti–18 at.%Nb as calculated by the ab initio method were  $C_{11} = 49.8$  GPa,  $C_{12} = 21.4$  GPa and  $C_{44} = 33.1$  GPa. The Zener anisotropy ratio, which is defined as  $2C_{44}/(C_{11} - C_{12})$ , amounts to 2.4. The predicted elastic constants for Ti–31 at.%Nb were  $C_{11} = 72.6$  GPa,  $C_{12} = 31.1$  GPa and  $C_{44} = 19.3$  GPa, giving a Zener ratio of 1.1. The rolling texture simulation was conducted using plane-strain compression boundary conditions and random initial texture. Fig. 45 shows the predicted crystallographic textures in terms of a set of

$\varphi_2 = 45^\circ$  sections through Euler space for the two cases. The results show that there is no pronounced relationship between slip system selection and the magnitude and anisotropy of the elastic constants.

A second (elastic) example of using ab initio elastic stiffness constants in a CPFE framework is shown in Fig. 46. The two diagrams present the distribution of the equivalent elastic stress and strain values in a randomly textured polycrystalline aggregate consisting of 200 grains and  $32 \times 32 \times 32$  elements for three different elastic tensors (magnitude, anisotropy) of three  $\beta$ -Ti alloys. The specimens were subjected to a unidirectional, purely elastic tensile load. The data show that an increase in the elastic anisotropy (quantified here in terms of the Zener ratio) leads to a remarkable increase in the spread of the stress–strain distribution. This means that local elastic loads (hot spots) among neighboring grains become more frequent as the elastic anisotropy increases. This effect may play a role in such diverse fields as internal stress evolution and stress corrosion cracking.

### 9.3.2. Grain meshing strategies in CPFE modeling

Delannay et al. [126] tested a set of different simulation approaches for the prediction of texture development and microscopic strain heterogeneity in cold-rolled ultra-low-carbon and multiphase steels under uniaxial tension (Fig. 47). The polycrystalline sample is represented by a FE mesh that is loaded under periodic boundary conditions. The individual crystals are shaped as cubes or as truncated octahedrons, defining three different levels of mesh refinement. Simulations rely on a simplified implementation of crystal plasticity, in which elastic strains are considered infinitesimal. The constitutive law is integrated fully implicitly in a reference frame that is tied to the crystal lattice. The results of the micro–macro modeling are compared to experimental data. The authors observe that the simulations with truncated octahedral grains yield improved predictions compared to those with cuboidal grains. This result is of relevance particularly for engineering applications of CPFE models where economical mesh and texture mapping strategies must be used owing to time and mesh size constraints.

### 9.3.3. Simulation of earing during cup drawing of steel and aluminum

This section presents examples of the CPFE method in the field of engineering forming problems at the macroscopic scale. The first example is about the prediction of earing during forming of a ferritic 17% Cr (X6Cr17, AISI 430) stainless steel sheet considering through-thickness gradients of the crystallographic texture. A texture component CPFE method (TCCP-FEM) [13,119,128,130,142] is used for the simulation of cup drawing. The simulation includes the through-thickness texture gradient of the starting hot band [419,420]. The simulation predicts the development of the orientation distribution and the earing profile during cup forming considering  $\{110\}\langle 111 \rangle$ ,  $\{112\}\langle 111 \rangle$  and



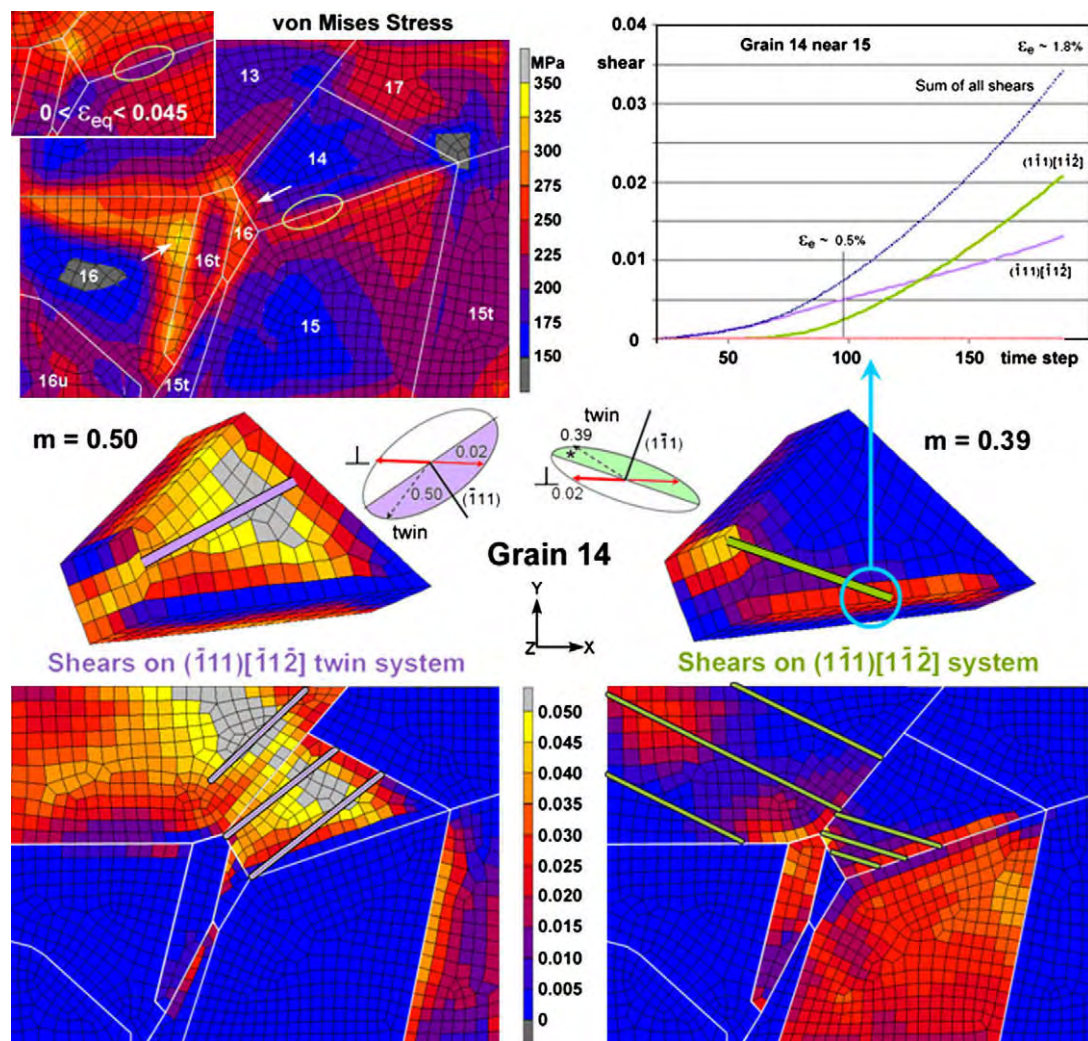


Fig. 44. Effective stress and equivalent strain (upper left) had modest values where microcracks were observed (ellipse). In the elements where microcracks were observed, the secondary twinning system was more activated than the primary twin system, consistent with experimental observations in Fig. 43.

$\{123\}\langle 111 \rangle$  slip systems [417]. The results are compared to another FE simulation (based on a Hill48 yield surface [421]) and to experimental data.

Fig. 48 shows the predicted and the measured earing profiles in terms of the relative ear height (normalized by the average height). The ear profile predicted by the simulation with the texture components of only the center layer ( $s = 0.0$ ) reveals a shape with a broad maximum around  $45^\circ$ . On the other hand, the profile simulated with the texture of only the subsurface layer ( $s = 0.8$ ) is characterized by a broad minimum in the same region ( $45^\circ$ ). The reason for this difference is that the texture components fitted from each respective layer of the material reproduced various initial textures and, consequently, different anisotropy. The course of the ear profile calculated by using only the texture components of the subsurface layer,  $s = 0.8$ , can be presumably explained by the influence of the relatively weak intensity of the  $\{111\}\langle 112 \rangle$  component of the starting texture in this layer. The high orientation density of the  $\{111\}\langle 112 \rangle$  texture component in the initial texture of the

mid-thickness layer ( $s = 0.0$ ) is responsible for the ear shape with the strong peak at  $45^\circ$  observed for the simulation that was performed by using the texture components of this layer. The results also show that the texture component CPFE simulation which used the gradient texture (1/3 of the through-thickness volume occupied by the center layer texture ( $s = 0.0$ ) and 2/3 of the volume occupied by the subsurface layer texture ( $s = 0.8$ ) where 1/3 accounts for the bottom and 1/3 for the top surface region, respectively) fits the experimental data better than that obtained from the Hill48 yield surface prediction. The second example, Fig. 49, shows a similar comparison between experiment and simulation for a cube-textured aluminum sheet after cup drawing. In this case no through-thickness texture gradients existed.

#### 9.3.4. Virtual material testing for stamping simulations based on crystal plasticity simulations

In the modern practice of simulating complex industrial stamping operations, the prediction of spring-back still

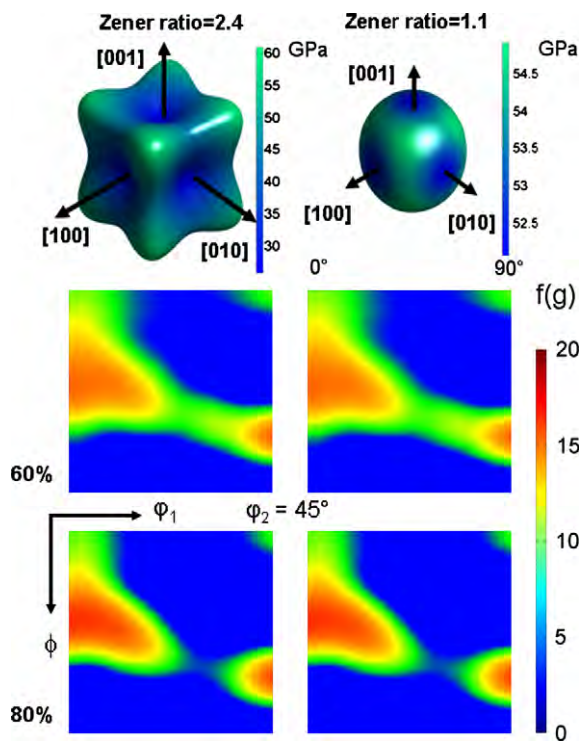


Fig. 45.  $\varphi_2 = 45^\circ$  sections of the orientation distribution functions obtained for deformation texture simulations of two  $\beta$ -Ti-Nb binary alloys to various strains (given in terms of the engineering thickness reduction) using two different sets of elastic constants. Top row: Young's modulus surface diagram of Ti-18 at.%Nb (left) and Ti-31 at.%Nb (right). The Zener ratio is defined as  $2C_{44}/(C_{11} - C_{12})$ . Units for the modulus surface plots are in GPa. Units for the textures are in orientation densities,  $f(g)$ .

lacks accuracy. In commercial software packages currently used, for instance, in the automotive industry, various empirical constitutive laws for stamping are available. As these approaches provide only limited empirical access to the material anisotropy they do not properly take into account the effects of microstructure and texture and their evolution during deformation. The CPFE method bridges the gap between the polycrystalline texture and macroscopic mechanical properties and opens the path to a more profound consideration of metal anisotropy in stamping process simulations.

The example in this section presents an application of the CPFE method for the concept of virtual material testing using a representative volume element (RVE) approach [217]. By using such numerical test protocols it becomes possible to determine the actual shape of the yield locus as well as corresponding Lankford parameters through CPFE simulations, and to use this information to calibrate empirical constitutive models used, for example, in the automotive industry. Along with standard uniaxial tensile tests, other strain paths can be numerically monitored, such as biaxial tensile, compressive or shear tests. In the present example the use of the CPFE method for virtual testing is demonstrated for a low-carbon steel grade. The parameters of an empirical yield surface function were cal-

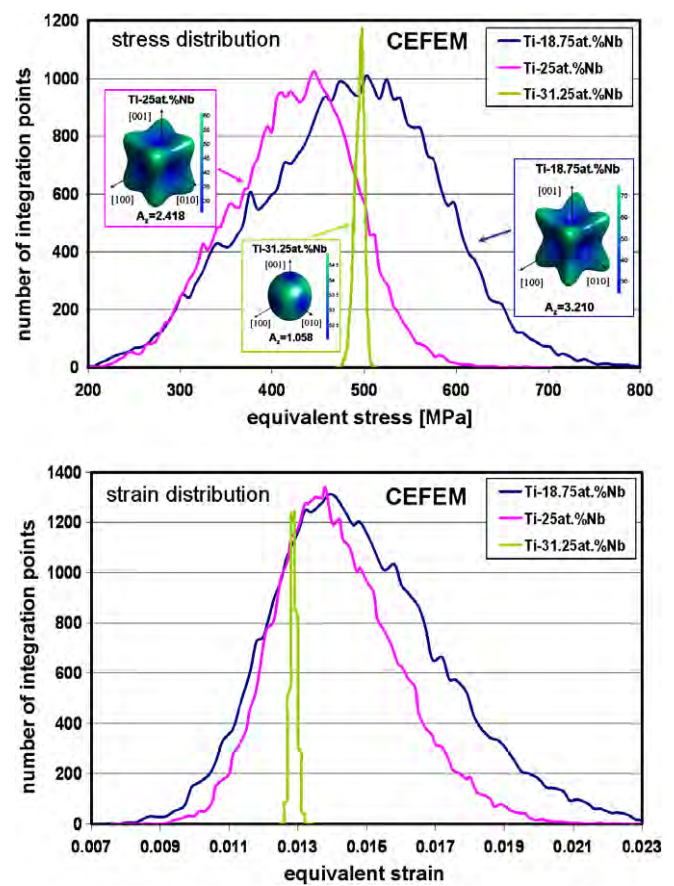


Fig. 46. Crystal elasticity finite element (CEFE) predictions of the distribution of elastic equivalent stress and strain values in three randomly textured polycrystalline  $\beta$ -Ti alloy aggregates each consisting of 200 grains and  $32 \times 32 \times 32$  finite elements. Each polycrystalline aggregate is characterized by a specific elastic tensor which was calculated using ab initio methods. The (nearly) isotropic case yields practically no internal mechanical spread, while the most anisotropic case leads to pronounced local stress-strain concentrations. The samples were subjected to tensile loading (purely elastic).

ibrated using CPFE predictions and a commercial stamping part was simulated (Fig. 50).

## 10. Challenges and open questions

This review showed that the CPFE method offers a comprehensive theoretical approach for the inclusion of micro-mechanical models and concepts in a unified theory of crystal plasticity including proper boundary condition treatment. However, there are critical gaps in the framework and in the experimental information that is required to support further development. The open questions can be grouped into issues of microstructure patterning; homogenization; physics and statistics behind constitutive models; damage mechanics; multiscale approaches; numerical stability; coupling to experiments; and alternative solution methods for crystal plasticity constitutive models.

The first category (microstructure patterning) refers to the fact that, during deformation, defects in crystals tend to self-organize into patterns which often reveal hierarchi-



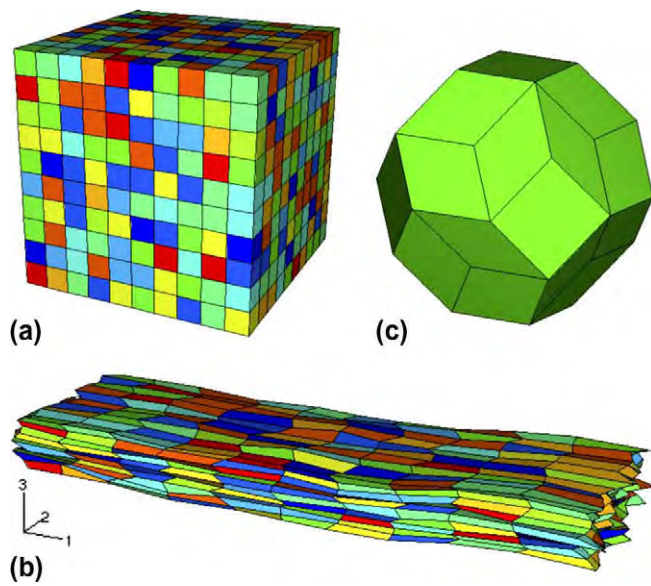


Fig. 47. Representation of the FE meshes used by Delannay et al. [126]. (a) Initial mesh in the simulation where brick shapes were used. (b) Result of plane-strain compression (periodic boundary conditions, 70% thickness reduction along  $3\times$ ). (c) Representation of one grain in the simulation as truncated octahedron [126].

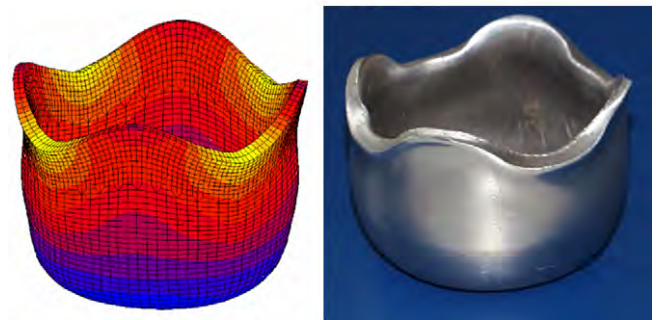
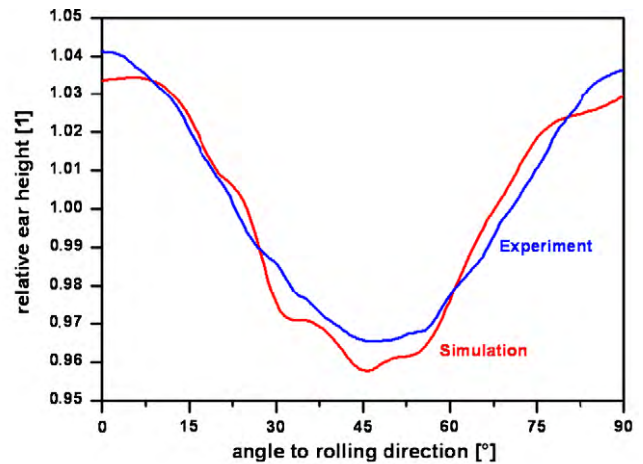


Fig. 49. Comparison of the earing profile between experiment and texture component CPFE simulation for a cube-textured aluminum sheet after cup drawing.

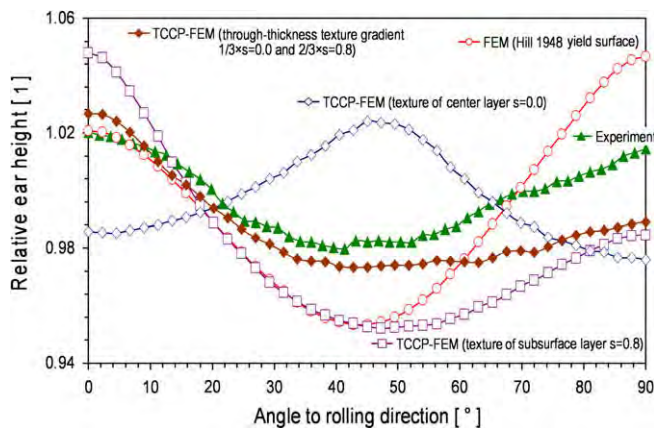


Fig. 48. Simulations and experimental data of the earing profile (ear height/average height) after cup drawing of a ferritic stainless steel (X6Cr17, AISI 430) with texture gradients. Different cases were simulated: in one case the texture component CPFE used only the texture components observed in the mid-thickness layer of the material as starting texture for all elements (at  $s = 0$ ). A second simulation used the subsurface texture components (at  $s = 0.8$ ) as starting texture for all elements. A third simulation used a mixture of mid-thickness texture components (at  $s = 0.0$ ) for the center element layer (1/3 of all mesh elements) and the subsurface texture components (at  $s = 0.8$ ) for the two surface element layers (2/3 of all mesh elements). In all cases the mesh consisted of three finite elements across the sheet thickness. Additionally, a Hill 48 yield surface calculation was performed where the coefficients were fitted from experimentally obtained  $r$ -values for this sheet.

cal structure. Different types of lattice defects reveal in part different deformation-induced pattern characteristics which often change in character and size scale as deformation proceeds (dislocation cells, subgrains, microbands, shear bands, martensite lamellae, twins packages, faceting, raf-

ting). Presently there is no adequate description of these processes within CPFE models linking the properties and dynamics of individual defects to a quantitative description of patterns in a form suitable for inclusion in non-local continuum theories, although promising energy minimization approaches have been discussed by Müller [422], Ortiz and Repetto [423], Bhattacharya [424], Aubry and Ortiz [425], Conti et al. [426] and Dmitrieva et al. [427].

The second category (homogenization) refers to the process by which the properties of a certain aggregate volume are derived from the local properties of its constituents by averaging over space and/or time. Homogenization is a most critical aspect for successful applications of the CPFE method at the mesoscopic scale and for macroscopic forming applications. It is clear that the microstructure and crystallographic texture of large parts cannot be presented via grain-by-grain maps (e.g. transferred from EBSD data onto a FE mesh). Instead, homogenized averages, formulated as separate submodels, must provide the mechanical response of a representative volume element [1,138,142,428]. These submodels deal with complex deformation mechanisms concerning the details of the interaction among competing deformation carriers, grains and phases at a simplified level. Typical approaches in this domain follow Taylor–Bishop–Hill or self-consistent model assumptions. Recent ideas for a more realistic treatment of local interactions in the field of multycrystal homogenization are advanced

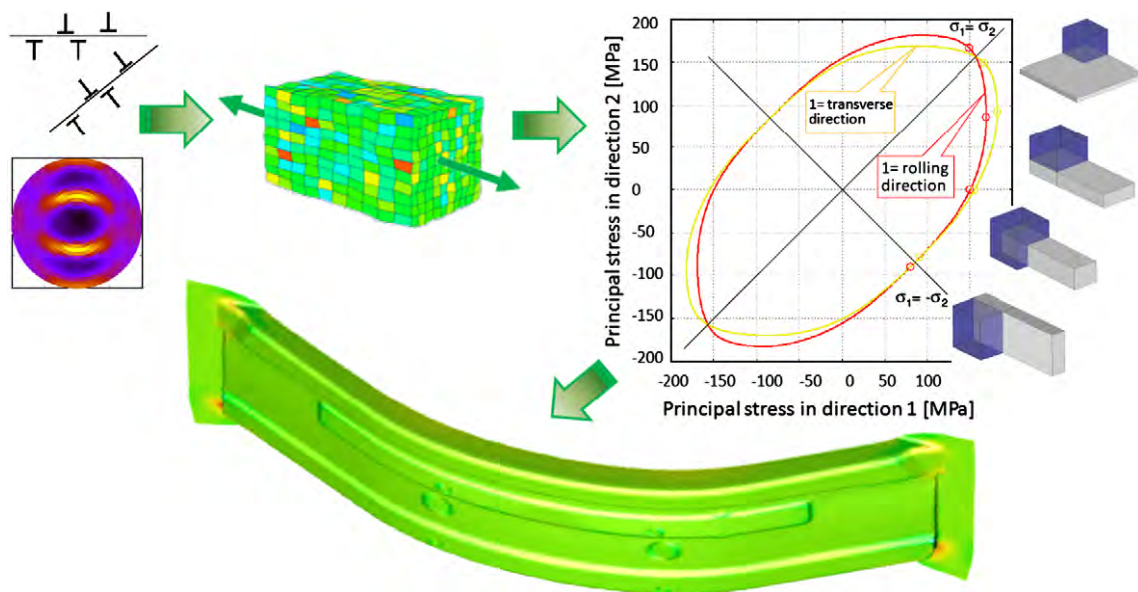


Fig. 50. Application of the CPFE method for virtual material testing using a representative volume element (RVE) approach. The parameters of an empirical yield locus function were calibrated for a low-carbon steel grade using CPFE and a commercial stamping part was simulated [217].

grain-interaction Taylor–Bishop–Hill-type model variants as introduced by the groups of Gottstein [319], Van Houtte [429] and Eisenlohr [430]. Alternatively, homogenization can also be conducted in two subsequent steps in the form of a hybrid approach. The first one consists in the assembly of virtual polycrystalline (and, if required, multiphase) specimens and the subsequent simulation of their integral response under load. The second step consists in feeding these results into simpler constitutive laws (e.g. as fitting constants into a yield surface polynomial) which do not require a CPFE framework (Fig. 50). These techniques are, for instance, currently under development for engineering applications in the automotive industry [217].

The third category (physics and statistics) refers to open questions behind constitutive CPFE model formulations. Some issues in this context involve the treatment of nucleation and growth phenomena of twins and martensite lamellae. In this field even some of the fundamental metallurgical mechanisms are not yet fully understood. Examples are nucleation models for deformation twins which are based on cooperatively acting configurations of partial dislocations or the nucleation of martensite plates at shear bands or existing interfaces. Furthermore, the degree of plastic deformation of martensite in an austenitic environment is not yet well understood. Methods need to be developed to efficiently model the formation of ultra-thin twins, twin packages and repeated twinning (higher-order deformation twins). Another issue is the constitutive formulation of misfit stresses around martensite lamellae. A further challenge associated with the consideration of multiple crystallographic deformation mechanisms within the same volume element lies in the degree of local homogenization that is required to tackle their interactions. This means that for some cases only one type of deformation

mechanism (e.g. dislocation slip) may prevail, while in others a mix (e.g. dislocation slip and deformation twinning) must be considered at the same integration point. The latter situation requires definition of a submodel (homogenization model) that describes the interaction of coexisting deformation mechanisms at the same field point. In addition to developing better models for mechanistic details, approaches for alloy element effects will also be a strategic area of further research. Future efforts in this direction must aim at capturing elementary chemical details in constitutive laws. Most CPFE simulations which are compared to experimental data have, for good reasons, been conducted on (commercially) pure metals or certain well-characterized simple alloys. Future formulations should consider changes caused by solid-solution effects and coherent or incoherent precipitations [162] on a sound physical and systematic basis so that variations in the mechanical response among similar alloys can be investigated [431]. Incorporation strategies that transfer the outcomes of phase-field modeling are a promising means to connect alloying and microstructure evolution to assess mechanical response. Other open questions in this field refer to the statistical limits of constitutive laws that typically anticipate some average density of defects but not their discrete arrangement. For dislocation-based constitutive formulations it may be important to consider in more detail mechanical effects that possibly start to dominate at small scales such as slip localization and slip burst events; dislocation source depletion; GNDs; surface source/sink effects; or grain boundary nucleation of dislocations [177,427,432]. Suitable dislocation-based frameworks, which could be modified to capture at least certain aspects of these mechanisms, have been suggested by various groups, e.g. [18–26,55,57]. Similar questions exist for the



role of the grain boundary structure on the mechanical response [21,25,41,45,95,233,248,249]. The role of diffusion in accommodating local strain concentrations, particularly in the context of creep and grain boundary sliding, has only recently been attempted, but only in two dimensions [61,62]. Finally it must be discussed how small the density of lattice defects may become within a certain element without violating the statistics behind a constitutive law. The latter questions are particularly relevant when applying the CPFE method to ultrafine structures (small samples, small grain size, lamellar structures, wire-drawn microstructures).

The fourth category (damage mechanics) deals with the overlap between crystal plasticity and fracture phenomena. The CPFE method is well suited for the identification of critical local parameters which may lead to damage initiation [199,200]. This advantage is obviously due to its ability to map realistic grain assemblies so that the effects of certain critical ingredients or configurations of such a given microstructure can be properly taken into account in a simulation. The main open question in this field is the identification of the mechanical and microstructure criteria that are responsible for local damage initiation. In some cases, such as in the presence of weak second-phase interfaces or brittle inclusions, the location of damage nucleation is rather trivial, but in other cases where damage occurs in otherwise homogeneous single-phase polycrystals, more complex rules are required. Possible criteria that are currently being investigated by CPFE simulations are critical local values for the accumulated amount of shear, deformation energy density or stress. In addition to the comparison of corresponding simulations with experiments it would also make sense to derive adequate damage criteria, such as modified Griffith models, which can help to establish a quantitative link between mechanical quantities that the CPFE method provides and damage nucleation. Promising approaches along these lines were recently investigated by the group of Bieler [199,200,380–383].

The fifth main aspect comprises multiscale models in conjunction with the CPFE method. Obviously this is a broad issue which needs to be refined. The term multiscale modeling refers to the integration of constitutive model ingredients which stem from different time and/or length scales and, as a rule, from different submodels. In the case of the CPFE method a most obvious need for multiscale approaches exists for those topics where current constitutive models have reached their limits. A prominent example is the integration of dislocation interactions which have been obtained from discrete dislocation dynamic codes into statistical dislocation density-based laws used in CPFE models. This approach is currently pursued by Arsenlis and Tang [65]. The direct use of results obtained from atomic-scale simulations is still a great challenge since a huge discrepancy in space, and particularly in time scale, exists between the atomistic and the crystal plasticity scale. Recent progress along these lines has been reported in the field of damage initiation where interactions between the microstructure scale

and the atomic scale play a dominant role [8,322,347–350]. For conventional dislocation motion it must be considered, though, that plasticity investigations via molecular dynamics simulations usually describe high-rate loading situations owing to the tiny integration steps required by the method. The deformation rates in such cases are typically orders of magnitude above realistic scales so that the transfer of such information must be done with great care since the results cannot in all cases be used for low-rate deformation constitutive models that typically prevail in CPFE simulations. Therefore, it may be more pertinent for molecular dynamics simulations of plasticity to provide certain constants or mechanisms for improved formulations of dislocation core structures, mobility, non-Schmid behavior, dislocation reactions, damage initiation and hardening mechanisms [265–267]. Other combinations are conceivable where a continuum-scale FE method is used for a proper boundary condition treatment around a simulation regime that is treated by an atomistic method. Finally, much progress may be expected from including thermodynamic and kinetic quantities that are derived by *ab initio* simulations [411,414–416,433]. These quantities can be fractions of coexisting phases, elastic constants [414,415,434] or the dependence of certain metallurgical properties on the chemical composition [416]. Although *ab initio* methods work at the electronic scale, i.e. at smaller integration steps than molecular dynamics simulations, many predictions obtained by them such as thermodynamic quantities can be directly linked to mesoscopic CPFE constitutive laws. We expect that results from parameter-free *ab initio* simulations obtained by using electron density functional approaches can particularly provide basic insight and constants for constitutive problems that are not accessible otherwise. Concerning the combination of the CPFE method with macroscopic mechanical simulation approaches, a most promising development might be the introduction of virtual laboratories, where expensive mechanical tests can be replaced by mesoscopic CPFE simulations. A typical example is the replacement of biaxial polycrystal tests as required for fitting yield surface formulations by CPFE predictions [217].

The sixth category of challenges are numerical and software aspects associated with the CPFE method. In this area the main issues are improved convergence behavior of the CPFE constitutive equations as well as a robust, modular and parallelized code architecture. A more practical advantage of the CPFE method in that context is that it can be used in conjunction with commercial or academic FE solvers in the form of easy-to-use user-defined materials subroutines. Various groups (including the current authors) make their software available as freeware for non-commercial use upon request.

The seventh category concerns the requirement of a more detailed comparison between crystal plasticity predictions and corresponding experiments. Modern characterization tools allow a detailed mechanical, metallurgical and crystallographic description of materials. The advantage of CPFE models is that they predict not only one

internal variable but a set of variables that can be effectively compared to corresponding experiments. Typical examples are crystallographic orientations, crack analysis, surface roughness, stress and strain, as well as corresponding gradient, patterning and localization effects associated with them (Table 2).

The last category concerns alternatives to the FE method for solving crystal elasticity, or respectively crystal plasticity, constitutive models. Some classical approaches were discussed in the section on homogenization. For instance, self-consistent and Taylor-based models, including in part also higher-order grain interaction terms, can serve for solving polycrystal mechanical problems without using finite elements at least under simplified boundary conditions [115,309,310,318,319,429,436,437]. Another important development for integrating crystal elasticity and plasticity constitutive models are direct fast Fourier methods [300] and Fourier-based spectral approaches [438,439]. These methods solve the equilibrium and compatibility constraints for anisotropic elastic or elastic–plastic polycrystal and polyphase problems using fast Fourier transforms [300,435,438–441]. The discrete Fourier approach renders the governing set of differential equations into a discrete algebraic problem which can be solved quicker than the conventional weak-form variational approach used by the FE method. In order to use discrete series expansions, spectral methods have to use a fixed grid and a representative cell arrangement of the microstructure considered. Discrete Fourier formulations imply periodicity of the modeled aggregate. Since the displacements lead to state values between the fixed coordinates of the discrete Fourier set-up, interpolation functions must be used.

A purely elastic example of using different stiffness tensors in the direct fast Fourier method of Lebensohn [300,435] is shown in Fig. 51. The two diagrams present the distribution of the equivalent elastic stress and strain values in a randomly textured polycrystalline aggregate consisting of 200 grains and  $32 \times 32 \times 32$  Fourier points for three different elastic tensors (magnitude, anisotropy) under a unidirectional tensile load. The entire aggregate remained in the elastic regime during loading. The results are very similar to the corresponding FE predictions presented in Fig. 46. The differences are attributed to the fact that the direct fast Fourier predictions used periodic boundary conditions, while the FE approach used a free surface.

## 11. Conclusions

It was demonstrated that the CPFE method is a powerful modeling tool for a wide range of mechanical problems in the field of materials science and engineering. We have shown that the dyadic kinematic formulation of the constitutive laws in the CPFE method allows the user to map such diverse deformation mechanisms as dislocation slip, martensite formation, twinning, grain boundary shear and deformation via shear banding (in glass), and, in part,

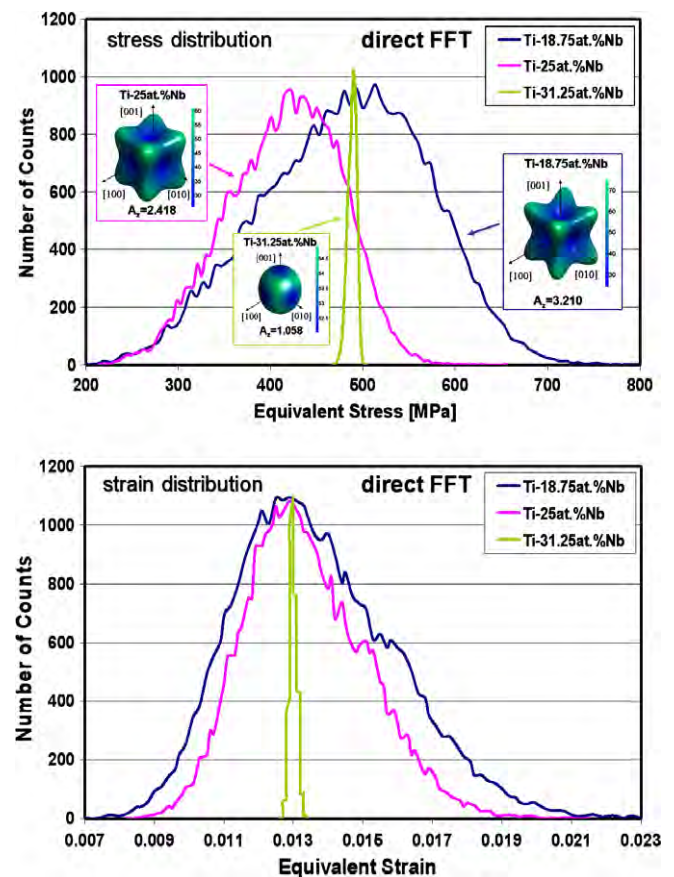


Fig. 51. Direct fast Fourier predictions of an elastic problem based on the approach of Lebensohn [300,435]. The results show the distribution of elastic equivalent stress and strain in three randomly textured polycrystalline  $\beta$ -Ti alloy aggregates, each consisting of 200 grains and  $32 \times 32 \times 32$  Fourier points. Each polycrystalline aggregate is characterized by a specific elastic tensor which was calculated using ab initio methods. The (nearly) isotropic case yields practically no internal mechanical spread, while the most anisotropic case leads to pronounced local stress–strain concentrations. The samples were subjected to tensile loading. The results are similar to the corresponding FE predictions presented above in Fig. 46. The differences between the direct fast Fourier and the FE results are attributed to the fact that the direct fast Fourier predictions used periodic boundary conditions while the FE approach used a free surface.

also their interactions, rendering the method a multimechanism and multiphysics approach. Its greatest potential lies, therefore, in the mesoscopic (inter-grain scale, grain cluster scale) and microscopic regime (grain scale, intra-grain scale). It was further shown that the CPFE method, when formulated in conjunction with an appropriate homogenization scheme, is also capable of dealing with macroscopic mechanical materials problems such as encountered in metal forming, tool design or process engineering. The particular strength of the FE method lies in studying the influence of boundary conditions on mechanical or microstructural predictions. This advantage renders the CPFE method an ideal companion for synergistic analysis of complex mechanical tests where a detailed sensitivity check is of relevance for a proper interpretation

of the experimental observations. Another more practical advantage of the method is that it can be used in conjunction with commercial or academic FE solvers in the form of user-defined materials subroutines (the software of the authors is available as freeware for non-commercial use upon request).

## Acknowledgments

The authors are grateful for multiple financial support of projects which were relevant for this overview such as the DFG Leibniz award funding, various DFG grants (Normalverfahren), DFG-SFB 370, and DFG-SFB 761 (SFB: Collaborative Research Center; DFG: Deutsche Forschungsgemeinschaft, German Research Foundation). We are thankful for many helpful discussions with Marc Geers, Lallit Anand, Günter Gottstein, Surya Kalidindi, Raul Radovitzky, Darren E. Mason, Heinrich Mecking, Ricardo Lebensohn, Fred Kocks, Paul Van Houtte, and Zisu Zhao. D.D.T. acknowledges supervision of S. van der Zwaag, S. Turteltaub, and A. Suiker (Delft University of Technology, the Netherlands) during his Ph.D. work at Delft University. We are particularly thankful to Craig S. Hartley for intense and in-depth discussions on flow kinematics and the sequence of dislocation deformation.

## References

- [1] Raabe D, Klose P, Engl B, Imlau K-P, Friedel F, Roters F. Concepts for integrating plastic anisotropy into metal forming simulations. *Adv Eng Mater* 2002;4:169–80.
- [2] Raabe D, Roters F, Barlat F, Chen L-Q, editors. *Continuum scale simulation of engineering materials fundamentals—microstructures—process applications*. Weinheim, Germany: Wiley-VCH; 2004 [ISBN 3-527-30760-5].
- [3] Sachs G. Zur Ableitung einer Fließbedingung. *Z VDI* 1928;72:734–6.
- [4] Taylor GI. Plastic strain in metals. *J Inst Met* 1938;62:307–24.
- [5] Bishop JFW, Hill R. A theory of the plastic distortion of a polycrystalline aggregate under combined stresses. *Philos Mag* 1951;42:414–27.
- [6] Bishop JFW, Hill R. A theoretical derivation of the plastic properties of a polycrystalline face centered metal. *Philos Mag* 1951;42:1298–307.
- [7] Kröner E. On the plastic deformation of polycrystals. *Acta Metall* 1961;9:155–61.
- [8] Curtin WA, Miller RE. Atomistic/continuum coupling in computational materials science. *Modell Simul Mater Sci Eng* 2003;11:R33–68.
- [9] Arsenlis A, Parks DM, Becker R, Bulatov VV. On the evolution of crystallographic dislocation density in non-homogeneously deforming crystals. *J Mech Phys Solids* 2004;52(6):1213–46.
- [10] Vitek V, Mrovec M, Bassani JL. Influence of non-glide stresses on plastic flow: from atomistic to continuum modeling. *Mater Sci Eng A* 2004;365:31–7.
- [11] Zienkiewicz OC. *The finite element method in structural and continuum mechanics*. 1st ed. New York: McGraw-Hill; 1967.
- [12] Zienkiewicz OC, Taylor RL. *The finite element method for solid and structural mechanics*. 6th ed. Butterworth-Heinemann; 2005.
- [13] Zhao Z, Mao W, Roters F, Raabe D. A texture optimization study for minimum earing in aluminium by use of a texture component crystal plasticity finite element method. *Acta Mater* 2004;52:1003–12.
- [14] Sachtleber M, Zhao Z, Raabe D. Experimental investigation of plastic grain interaction. *Mater Sci Eng A* 2002;336(1–2):81–7.
- [15] Raabe D, Sachtleber M, Weiland H, Scheele G, Zhao Z. Grain-scale micromechanics of polycrystal surfaces during plastic straining. *Acta Mater* 2003;51:1539–60.
- [16] Rice JR. Inelastic constitutive relations for solids: an internal variable theory and its application to metal plasticity. *J Mech Phys Solids* 1971;19:433–55.
- [17] Asaro RJ, Rice JR. Strain localization in ductile single crystals. *J Mech Phys Solids* 1977;25:309–38.
- [18] Arsenlis A, Parks DM. Crystallographic aspects of geometrically-necessary and statistically-stored dislocation density. *Acta Mater* 1999;47(5):1597–611.
- [19] Arsenlis A, Parks DM. Modeling the evolution of crystallographic dislocation density in crystal plasticity. *J Mech Phys Solids* 2002;50(9):1979–2009.
- [20] Evers LP, Parks DM, Brekelmans WAM, Geers MGD. Crystal plasticity model with enhanced hardening by geometrically necessary dislocation accumulation. *J Mech Phys Solids* 2002;50(11):2403–24.
- [21] Evers LP, Brekelmans WAM, Geers MGD. Scale dependent crystal plasticity framework with dislocation density and grain boundary effects. *Int J Solids Struct* 2004;41(10):5209–30.
- [22] Cheong K-S, Busso EP. Discrete dislocation density modelling of single phase FCC polycrystal aggregates. *Acta Mater* 2004;52:665–675.
- [23] Ma A, Roters F. A constitutive model for fcc single crystals based on dislocation densities and its application to uniaxial compression of aluminium single crystals. *Acta Mater* 2004;52(12):3603–12.
- [24] Ma A, Roters F, Raabe D. A dislocation density based constitutive model for crystal plasticity FEM including geometrically necessary dislocations. *Acta Mater* 2006;54:2169–79.
- [25] Ma A, Roters F, Raabe D. On the consideration of interactions between dislocations and grain boundaries in crystal plasticity finite element modeling—theory, experiments, and simulations. *Acta Mater* 2006;54:2181–94.
- [26] Evers LP, Brekelmans WAM, Geers MGD. Non-local crystal plasticity model with intrinsic SSD and GND effects. *J Mech Phys Solids* 2004;52(10):2379–401.
- [27] Peirce D, Asaro RJ, Needleman A. An analysis of nonuniform and localized deformation in ductile single crystals. *Acta Metall* 1982;30:1087–119.
- [28] Becker R. Effects of strain localization on surface roughening during sheet forming. *Acta Mater* 1998;46:1385–401.
- [29] Zhao Z, Radovitzky R, Cuitiño A. A study of surface roughening in fcc metals using direct numerical simulation. *Acta Mater* 2004;52(20):5791–804.
- [30] Yue ZF. Surface roughness evolution under constant amplitude fatigue loading using crystal plasticity. *Eng Fract Mech* 2005;72:749–57.
- [31] Siska F, Forest S, Gumbsch P. Simulations of stress strain heterogeneities in copper thin films: texture and substrate effects. *Comput Mater Sci* 2007;39:137–41.
- [32] Zhao Z, Ramesh M, Raabe D, Cuitiño A, Radovitzky R. Investigation of three-dimensional aspects of grain-scale plastic surface deformation of an aluminum oligocrystal. *Int J Plast* 2008;24:2278–97.
- [33] Becker R, Panchanadeeswaran S. Effects of grain interactions on deformation and local texture in polycrystals. *Acta Mater* 1995;43:2701–19.
- [34] Mika DP, Dawson PR. Effects of grain interaction on deformation in polycrystals. *Mater Sci Eng A* 1998;257:62–76.
- [35] Acharya A, Beaudoin AJ. Grain-size effect in viscoplastic polycrystals at moderate strains. *J Mech Phys Solids* 2000;48:2213–30.
- [36] Meissonnier FT, Busso EP, O'Dowd NP. Finite element implementation of a generalised non-local rate-dependent crystallographic formulation for finite strains. *Comput Mater Sci* 2001;17:601–40.

- [37] Barbe F, Decker L, Jeulin D, Cailletaud G. Intergranular and intragranular behavior of polycrystalline aggregates. Part 1: F.E. model. *Int J Plast* 2001;17:513–36.
- [38] Raabe D, Sachtleber M, Zhao Z, Roters F, Zaefferer S. Micromechanical and macromechanical effects in grain scale polycrystal plasticity experimentation and simulation. *Acta Mater* 2001;49(17):3433–41.
- [39] Park SJ, Han HN, Oh KH, Raabe D, Kim JK. Finite element simulation of grain interaction and orientation fragmentation during plastic deformation of BCC metals. *Mater Sci Forum* 2002;408–4:371–6.
- [40] Clarke AP, Humphreys FJ, Bate PS. Lattice rotations at large second-phase particles in polycrystalline aluminum. *Mater Sci Forum* 2003;426:399–404.
- [41] Wei YJ, Anand L. Grain-boundary sliding and separation in polycrystalline metals: application to nanocrystalline fcc metals. *J Mech Phys Solids* 2004;52:2587–616.
- [42] Fu H-H, Benson DJ, Meyers MA. Computational description of nanocrystalline deformation based on crystal plasticity. *Acta Mater* 2004;52:4413–25.
- [43] Diard O, Leclercq S, Rousselier G, Cailletaud G. Evaluation of finite element based analysis of 3D multicrystalline aggregates plasticity: application to crystal plasticity model identification and the study of stress and strain fields near grain boundaries. *Int J Plast* 2005;21:691–722.
- [44] Bate PS, Hutchinson WB. Grain boundary area and deformation. *Scripta Mater* 2005;52:199–203.
- [45] Wei YJ, Su C, Anand L. A computational study on the mechanical behavior of nanocrystalline fcc metals. *Acta Mater* 2006;54:3177–90.
- [46] Murphy BP, Cuddy H, Harewood FJ, Connolly T, McHugh PE. The influence of grain size on the ductility of micro-scale stainless steel stent struts. *J Mater Sci—Mater Med* 2006;17:1–6.
- [47] Deka D, Joseph DS, Ghosh S, Mills MJ. Crystal plasticity modeling of deformation and creep in polycrystalline Ti-6242. *Metall Mater Trans A* 2006;37:1371–88.
- [48] Counts WA, Braginsky WA, Battaile CC, Holm EA. Predicting the Hall–Petch effect in fcc metals using non-local crystal plasticity. *Int J Plast* 2008;24:1243–63.
- [49] Gurtin ME, Anand L, Lele SP. Gradient single-crystal plasticity with free energy dependent on dislocation densities. *J Mech Phys Solids* 2007;55:1853–78.
- [50] Venkatramani G, Ghosh S, Mills M. A size-dependent crystal plasticity finite-element model for creep and load shedding in polycrystalline titanium alloys. *Acta Mater* 2007;55:971–3986.
- [51] Okumura D, Higashi Y, Sumida K, Ohno N. A homogenization theory of strain gradient single crystal plasticity and its finite element discretization. *Int J Plast* 2007;23:1148–66.
- [52] Gerken JM, Dawson PR. A finite element formulation to solve a non-local constitutive model with stresses and strains due to slip gradients. *Comput Methods Appl Mech Eng* 2008;197:1343–61.
- [53] Gerken JM, Dawson PR. A crystal plasticity model that incorporates stresses and strains due to slip gradients. *J Mech Phys Solids* 2008;56:1651–72.
- [54] Kuroda M, Tvergaard V. On the formulations of higher-order strain gradient crystal plasticity models. *J Mech Phys Solids* 2008;56:1591–608.
- [55] Bitzek E, Derlet PM, Anderson PM, Van Swygenhoven H. The stress–strain response of nanocrystalline metals: a statistical analysis of atomistic simulations. *Acta Mater* 2008;56:846–4857.
- [56] Borg U, Niordson CF, Kysar JW. Size effects on void growth in single crystals with distributed voids. *Int J Plast* 2008;24: 688–701.
- [57] Li L, Anderson PM, Lee M-G, Bitzek E, Derlet P, Van Swygenhoven H. The stress–strain response of nanocrystalline metals: a quantized crystal plasticity approach. *Acta Mater* 2009;57:812–22.
- [58] McHugh PE, Mohrmann R. Modelling of creep in a Ni base superalloy using a single crystal plasticity model. *Comput Mater Sci* 1997;9:134–40.
- [59] Balasubramanian S, Anand L. Plasticity of initially textured hexagonal polycrystals at high homologous temperatures: application to titanium. *Acta Mater* 2002;50:133–48.
- [60] Hasija V, Ghosh S, Mills MJ, Joseph DS. Deformation and creep modeling in polycrystalline Ti–6Al alloys. *Acta Mater* 2003;51:4533–49.
- [61] Bower AF, Winer E. A two-dimensional finite element method for simulating the constitutive response and microstructure of polycrystals during high temperature plastic deformation. *J Mech Phys Solids* 2004;52:1289–317.
- [62] Agarwal S, Briant CL, Krajewski PE, Bower AF, Taleff EM. Experimental validation of two-dimensional finite element method for simulating constitutive response of polycrystals during high temperature plastic deformation. *J Mater Eng Perf* 2007;16: 170–8.
- [63] Venkataramani G, Kirane K, Ghosh S. Microstructural parameters affecting creep induced load shedding in Ti-6242 by a size dependent crystal plasticity FE model. *Int J Plast* 2008;24:428–54.
- [64] Xu B, Yonezu A, Yue Z, Chen X. Indentation creep surface morphology of nickel-based single crystal superalloys. *Comput Mater Sci* 2009;46:275–85.
- [65] Arsenlis A, Tang M. Simulations on the growth of dislocation density during Stage 0 deformation in BCC metals. *Modell Simul Mater Sci Eng* 2003;11:251–64.
- [66] McDowell D L. Viscoplasticity of heterogeneous metallic materials. *Mater Sci Eng R* 2008;62:67–123.
- [67] Marketz F, Fischer FD. Micromechanical modelling of stress-assisted martensitic transformation. *Modell Simul Mater Sci Eng* 1994;2:1017–46.
- [68] Marketz F, Fischer FD. A mesoscale study on the thermodynamic effect of stress on martensitic transformation. *Metall Mater Trans A* 1995;26:267–78.
- [69] Tomita Y, Iwamoto T. Constitutive modeling of TRIP steel and its application to the improvement of the mechanical properties. *Int J Mech Sci* 1995;37:1295–305.
- [70] Diani JM, Sabar H, Berveiller M. Micromechanical modelling of the transformation induced plasticity (TRIP) phenomenon in steels. *Int J Eng Sci* 1995;33:1921–34.
- [71] Diani JM, Parks DM. Effects of strain state on the kinetics of strain-induced martensite in steels. *J Mech Phys Solids* 1998;46(9): 1613–35.
- [72] Cherkaoui M, Berveiller M, Sabar H. Micromechanical modeling of martensitic transformation-induced plasticity (TRIP) in austenitic single crystals. *Int J Plast* 1998;14:597–626.
- [73] Cherkaoui M, Berveiller M, Lemoine X. Coupling between plasticity and martensitic phase transformation: overall behavior of polycrystalline TRIP steels. *Int J Plast* 2000;16:1215–41.
- [74] Thamburaja P, Anand L. Polycrystalline shape-memory materials: effect of crystallographic texture. *J Mech Phys Solids* 2001;49:709–37.
- [75] Tomita Y, Iwamoto T. Computational prediction of deformation behavior of TRIP steels under cyclic loading. *Int J Mech Sci* 2001;43:2017–34.
- [76] Govindjee S, Miehe C. A multi-variant martensitic phase transformation model: formulation and numerical implementation. *Comput Methods Appl Mech Eng* 2001;191:215–38.
- [77] Anand L, Gurtin ME. Thermal effects in the superelasticity of crystalline shape-memory materials. *J Mech Phys Solids* 2003;51:1015–58.
- [78] Turteltaub S, Suiker ASJ. Transformation-induced plasticity in ferrous alloys. *J Mech Phys Solids* 2005;53:1747–88.
- [79] Thamburaja P. Constitutive equations for martensitic reorientation and detwinning in shape-memory alloys. *J Mech Phys Solids* 2005;53:825–56.
- [80] Lan YJ, Xiao NM, Li DZ, Li YY. Mesoscale simulation of deformed austenite decomposition into ferrite by coupling a cellular automaton method with a crystal plasticity finite element model. *Acta Mater* 2005;53:991–1003.



- [81] Turteltaub S, Suiker ASJ. Grain size effects in multiphase steels assisted by transformation-induced plasticity. *Int J Solids Struct* 2006;43:7322–36.
- [82] Tjahjanto DD, Turteltaub S, Suiker ASJ. Crystallographically-based model for transformation-induced plasticity in multiphase carbon steels. *Continuum Mech Thermodyn* 2008;19:399–422.
- [83] Geers MGD, Kouznetsova VG. Modeling the interaction between plasticity and the austenite–martensite transformation. *Int J Multiscale Comput* 2007;5:29–140.
- [84] Peirce D, Asaro RJ, Needleman A. Material rate dependence and localized deformation in crystalline solids. *Acta Metall* 1983;31:1951–76.
- [85] Beaudoin AJ, Dawson PR, Mathur KK, Kocks UF. A hybrid finite element formulation for polycrystal plasticity with consideration of macrostructural and microstructural linking. *Int J Plast* 1995;11:501–21.
- [86] Sarma GB, Dawson PR. Texture predictions using a polycrystal plasticity model incorporating neighbor interactions. *Int J Plast* 1996;12(8):1023–54.
- [87] Sarma GB, Dawson PR. Effects of interactions among crystals on the inhomogeneous deformations of polycrystals. *Acta Mater* 1996;44:1937–53.
- [88] Sarma GB, Radhakrishnan B, Zacharia T. Finite element simulations of cold deformation at the mesoscale. *Comput Mater Sci* 1998;12:105–23.
- [89] Forest S. Modeling slip, kink and shear banding in classical and generalized single crystal plasticity. *Acta Mater* 1998;46:3265–81.
- [90] Bhattacharyya A, El-Danaf E, Kalidindi SR, Doherty RD. Evolution of grain-scale microstructure during large strain simple compression of polycrystalline aluminum with quasi-columnar grains: OIM measurements and numerical simulations. *Int J Plast* 2001;17:861–83.
- [91] Miller MP, Turner TJ. A methodology for measuring and modeling crystallographic texture gradients in processed alloys. *Int J Plast* 2001;17:783–805.
- [92] Raabe D, Zhao Z, Park S-J, Roters F. Theory of orientation gradients in plastically strained crystals. *Acta Mater* 2002;50:421–40.
- [93] Kim H-K, Oh S-I. Finite element analysis of grain-by-grain deformation by crystal plasticity with couple stress. *Int J Plast* 2003;19:1245–70.
- [94] Choi SH. Simulation of stored energy and orientation gradients in cold-rolled interstitial free steels. *Acta Mater* 2003;51:1775–88.
- [95] Zaefferer S, Kuo J-C, Zhao Z, Winning M, Raabe D. On the influence of the grain boundary misorientation on the plastic deformation of aluminum bicrystals. *Acta Mater* 2003;51(16):4719–35.
- [96] Eriau P, Rey C. Modeling of deformation and rotation bands and of deformation induced grain boundaries in IF steel aggregate during large plane strain compression. *Int J Plast* 2004;20:1763–88.
- [97] Sarma GB, Radhakrishnan B. Modeling microstructural effects on the evolution of cube texture during hot deformation of aluminum. *Mater Sci Eng A* 2004;385:91–104.
- [98] Roters F, Wang Y, Kuo J-C, Raabe D. Comparison of single crystal simple shear deformation experiments with crystal plasticity finite element simulations. *Adv Eng Mater* 2004;6(8):653–6.
- [99] Kim K-H, Kim H-K, Oh S-I. Deformation behavior of pure aluminum specimen composed of a few grains during simple compression. *J Mater Process Technol* 2006;171:205–13.
- [100] daFonseca JQ, Oliver EC, Bate PS, Withers PJ. Evolution of intergranular stresses during in situ straining of IF steel with different grain sizes. *Mater Sci Eng A* 2006;437:26–32.
- [101] You X, Connolly T, McHugh PE, Cuddy H, Motz C. A combined experimental and computational study of deformation in grains of biomedical grade 316LVM stainless steel. *Acta Mater* 2006;54:4825–40.
- [102] Musienko A, Tatschl A, Schmidegg K, Kolednik O, Pippan R, Caillaud G. Three-dimensional finite element simulation of a polycrystalline copper specimen. *Acta Mater* 2007;55:4121–36.
- [103] Han T-S, Dawson PR. A two-scale deformation model for polycrystalline solids using a strongly-coupled finite element methodology. *Comput Methods Appl Mech Eng* 2007;196:2029–43.
- [104] Zhang F, Bower AF, Mishra RK, Boyle KP. Numerical simulations of necking during tensile deformation of aluminum single crystals. *Int J Plast* 2009;25:49–69.
- [105] Asaro RJ, Needleman A. Texture development and strain hardening in rate dependent polycrystals. *Acta Metall* 1985;33:923–53.
- [106] Becker R. Analysis of texture evolution in channel die compression—I. Effects of grain interaction. *Acta Metall Mater* 1991;39:1211–30.
- [107] Becker R, Butler JF, Hu H, Lalli LA. Analysis of an aluminum single crystal with unstable initial orientation (001) [111] in channel die compression. *Metall Trans A* 1991;22:45–58.
- [108] Bronkhorst CA, Kalidindi SR, Anand L. Polycrystalline plasticity and the evolution of crystallographic texture in FCC metals. *Philos Trans Roy Soc Lond A* 1992;341(1662):443–77.
- [109] Kalidindi SR, Bronkhorst CA, Anand L. Crystallographic texture evolution in bulk deformation processing of fcc metals. *J Mech Phys Solids* 1992;40:537–69.
- [110] Beaudoin AJ, Mecking H, Kocks UF. Development of localized orientation gradients in fcc polycrystals. *Philos Mag A* 1996;73:1503–17.
- [111] Bertram A, Böhlke T, Kraska M. Numerical simulation of deformation induced anisotropy of polycrystals. *Comput Mater Sci* 1997;9:158–67.
- [112] Mika DP, Dawson PR. Polycrystal plasticity modeling of intracrystalline boundary textures. *Acta Mater* 1999;47:1355–69.
- [113] Miehe C, Schröder J, Schotte J. Computational homogenization analysis in finite plasticity simulation of texture development in polycrystalline materials. *Comput Methods Appl Mech Eng* 1999;171:387–418.
- [114] Kalidindi SR. Modeling anisotropic strain hardening and deformation textures in low stacking fault energy fcc metals. *Int J Plast* 2001;17:837–60.
- [115] Van Houtte P, Delannay L, Kalidindi SR. Comparison of two grain interaction models for polycrystal plasticity and deformation texture prediction. *Int J Plast* 2002;18:359–77.
- [116] Delannay L, Kalidindi SR, Van Houtte P. Quantitative prediction of textures in aluminium cold rolled to moderate strains. *Mater Sci Eng A* 2002;336:233–44.
- [117] Raabe D, Zhao Z, Mao W. On the dependence of in-grain subdivision and deformation texture of aluminum on grain interaction. *Acta Mater* 2002;50:4379–94.
- [118] Bate PS, An YG. Plastic anisotropy in AA5005 Al–1Mg: predictions using crystal plasticity finite element analysis. *Scripta Mater* 2004;51:973–7.
- [119] Raabe D, Zhao Z, Roters F. Study on the orientational stability of cube-oriented FCC crystals under plane strain by use of a texture component crystal plasticity finite element method. *Scripta Mater* 2004;50:1085–90.
- [120] Li SY, Van Houtte P, Kalidindi SR. A quantitative evaluation of the deformation texture predictions for aluminium alloys from crystal plasticity finite element method. *Modell Simul Mater Sci Eng* 2004;12:845–70.
- [121] Anand L. Single-crystal elasto-viscoplasticity: application to texture evolution in polycrystalline metals at large strains. *Comput Methods Appl Mech Eng* 2004;193:5359–83.
- [122] Roters F, Jeon-Haurand HS, Raabe D. A texture evolution study using the texture component crystal plasticity FEM. *Mater Sci Forum* 2005;495–497:937–44.
- [123] Van Houtte P, Van Bael A, Seefeldt M, Delannay L. The application of multiscale modelling for the prediction of plastic anisotropy and deformation textures. *Mater Sci Forum* 2005;495–497:31–41.
- [124] Li S, Kalidindi SR, Beyerlein IJ. A crystal plasticity finite element analysis of texture evolution in equal channel angular extrusion. *Mater Sci Eng A* 2005;410–411:207–12.

- [125] Van Houtte P, Kanjarla AK, Van Bael A, Seefeldt M, Delannay L. Multiscale modelling of the plastic anisotropy and deformation texture of polycrystalline materials. *Eur J Mech—Solids* 2006;25:634–48.
- [126] Delannay L, Jacques PJ, Kalidindi SR. Finite element modeling of crystal plasticity with grains shaped as truncated octahedrons. *Int J Plast* 2006;22:1879–98.
- [127] Tang JG, Zhang XM, Chen ZY, Deng YL. Simulation of rolling deformation texture of fcc metals with crystal plasticity finite element model. *Mater Sci Technol* 2006;22:1171–6.
- [128] Tikhovskiy I, Raabe D, Roters F. Simulation of the deformation texture of a 17 stainless steel using the texture component crystal plasticity FE method considering texture gradients. *Scripta Mater* 2006;54:1537–42.
- [129] Lee MG, Wang J, Anderson PM. Texture evolution maps for upset deformation of body-centered cubic metals. *Mater Sci Eng A* 2007;463:263–70.
- [130] Tikhovskiy I, Raabe D, Roters F. Simulation of earing during deep drawing of an Al-3 (AA 5754) using a texture component crystal plasticity FEM. *J Mater Process Technol* 2007;183:169–75.
- [131] Mayeur JR, McDowell DL, Neu RW. Crystal plasticity simulations of fretting of Ti–6Al–4V in partial slip regime considering effects of texture. *Comput Mater Sci* 2008;41:356–65.
- [132] Delannay L, Melchior MA, Signorelli JW, Remacle JF, Kuwabara T. Influence of grain shape on the planar anisotropy of rolled steel sheets—evaluation of three models. *Comput Mater Sci* 2009;45:739–43.
- [133] Beaudoin AJ, Mathur KK, Dawson PR, Johnson GC. Three-dimensional deformation process simulation with explicit use of polycrystal plasticity models. *Int J Plast* 1993;9:833–60.
- [134] Beaudoin AJ, Dawson PR, Mathur KK, Kocks UF, Korzekwa DA. Application of polycrystal plasticity to sheet forming. *Comput Methods Appl Mech Eng* 1994;117:49–70.
- [135] Neale KW. Use of crystal plasticity in metal forming simulations. *Int J Mech Sci* 1993;35:1053–63.
- [136] Kalidindi SR, Schoenfeld SE. On the prediction of yield surfaces by the crystal plasticity models for fcc polycrystals. *Mater Sci Eng A* 2000;293:20–129.
- [137] Nakamachi E, Xie CL, Harimoto M. Drawability assessment of BCC steel sheet by using elastic/crystalline viscoplastic finite element analyses. *Int J Mech Sci* 2001;43:631–52.
- [138] Zhao Z, Mao W, Roters F, Raabe D. Introduction of a texture component crystal plasticity finite element method for anisotropy simulations. *Adv Eng Mater* 2001;3:984–90.
- [139] Xie CL, Nakamachi E. Investigations of the formability of BCC steel sheets by using crystalline plasticity finite element analysis. *Mater Des* 2002;23:59–68.
- [140] Goh C-H, Neu RW, McDowell DL. Crystallographic plasticity in fretting of Ti–6Al–4V. *Int J Plast* 2003;19:1627–50.
- [141] McGarry JP, O'Donnell BP, McHugh PE, McGarry JG. Analysis of the mechanical performance of a cardiovascular stent design based on micromechanical modelling. *Comput Mater Sci* 2004;31:421–38.
- [142] Raabe D, Roters F. Using texture components in crystal plasticity finite element simulations. *Int J Plast* 2004;20:339–61.
- [143] Tugcu P, Neale KW, Wu PD, Inal K. Crystal plasticity simulation of the hydrostatic bulge test. *Texture Microstruct* 2004;20:1603–53.
- [144] Delannay L, Beringhier M, Chastel Y, Loge RE. Simulation of cup-drawing based on crystal plasticity applied to reduced grain samplings. *Mater Sci Forum* 2005;495–497:1639–44.
- [145] Raabe D, Wang Y, Roters F. Crystal plasticity simulation study on the influence of texture on earing in steel. *Comput Mater Sci* 2005;34:221–34.
- [146] Dick T, Caillaud G. Fretting modelling with a crystal plasticity model of Ti6Al4V. *Comput Mater Sci* 2006;38:113–25.
- [147] Chen YP, Lee WB, To S. Influence of initial texture on formability of aluminum sheet metal by crystal plasticity FE simulation. *J Mater Process Technol* 2007;192–193:397–403.
- [148] Raabe D. Recrystallization models for the prediction of crystallographic textures with respect to process simulation. *J Strain Anal Eng Des* 2007;42:253–68.
- [149] Nakamachi E, Tam NN, Morimoto H. Multi-scale finite element analyses of sheet metals by using SEM-EBSD measured crystallographic RVE models. *Int J Plast* 2007;23:450–89.
- [150] Ocenasek J, Rodriguez Ripoll M, Weygand SM, Riedel H. Multi-grain finite element model for studying the wire drawing process. *Comput Mater Sci* 2007;39:23–8.
- [151] Li S, Donohue BR, Kalidindi SR. A crystal plasticity finite element analysis of cross-grain deformation heterogeneity in equal channel angular extrusion and its implications for texture evolution. *Mater Sci Eng A* 2008;480:17–23.
- [152] Li HJ, Jiang Z, Han JT, Wei DB, Pi HC, Tieu AK. Crystal plasticity finite element modeling of necking of pure aluminium during uniaxial tensile deformation. *Steel Res* 2008;2:655–62.
- [153] Zhuang WM, Wang SW, Cao J, Lin LG, Hart C. Hydroforming of micro tubes: crystal plasticity finite element modeling. *Steel Res* 2008;1:293–300 [special issue].
- [154] Zamiri A, Bieler TR, Pourboghrat F. Anisotropic crystal plasticity finite element modeling of the effect of crystal orientation and solder joint geometry on deformation after temperature change. *J Electron Mater* 2009;38:231–40.
- [155] Bate P. Modelling deformation microstructure with the crystal plasticity finite-element method. *Philos Trans Roy Soc Lond A* 1999;357:1589–601.
- [156] Raabe D, Becker R. Coupling of a crystal plasticity finite element model with a probabilistic cellular automaton for simulating primary static recrystallization in aluminum. *Modell Simul Mater Sci Eng* 2000;8:445–62.
- [157] Raabe D. Yield surface simulation for partially recrystallized aluminum polycrystals on the basis of spatially discrete data. *Comput Mater Sci* 2000;19:13–26.
- [158] Radhakrishnan B, Sarma G, Weiland H, Baggethun P. Simulations of deformation and recrystallization of single crystals of aluminum containing hard particles. *Modell Simul Mater Sci Eng* 2002;8:737–50.
- [159] Raabe D. Cellular automata in materials science with particular reference to recrystallization simulation. *Annu Rev Mater Res* 2002;32:53–76.
- [160] Takaki T, Yamanaka Y, Higa Y, Tomita Y. Phase-field model during static recrystallization based on crystal-plasticity theory. *J Comput Aided Mater Des* 2007;14:75–84.
- [161] Semiatin SL, Weaver DS, Goetz RL, Thomas JP, Turner TJ. Deformation and recrystallization during thermomechanical processing of a nickel-base superalloy ingot material. *Mater Sci Forum* 2007;550:129–40.
- [162] Zambaldi C, Roters F, Raabe D, Glatzel U. Modeling and experiments on the indentation deformation and recrystallization of a single-crystal nickel-base superalloy. *Mater Sci Eng A* 2007;454–455:433–40.
- [163] Loge R, Bernacki M, Resk H, Delannay L, Dignonnet H, Chastel Y, et al. Linking plastic deformation to recrystallization in metals using digital microstructures. *Philos Mag* 2008;88(30):3691–712.
- [164] Kalidindi SR. Incorporation of deformation twinning in crystal plasticity models. *J Mech Phys Solids* 1998;46:267–90.
- [165] Staroselsky A, Anand L. Inelastic deformation of polycrystalline face centered cubic materials by slip and twinning. *J Mech Phys Solids* 1998;46:671–96.
- [166] Marketz WT, Fischer FD, Kauffmann F, Dehm G, Bidlingmaier T, Wanner A, et al. On the role of twinning during room temperature deformation of TiAl based alloys. *Mater Sci Eng A* 2002;329–331:177–83.
- [167] Staroselskya A, Anand L. A constitutive model for hcp materials deforming by slip and twinning: application to magnesium alloy AZ31B. *Int J Plast* 2003;19:1843–64.
- [168] Marketz WT, Fischer FD, Clemens H. Deformation mechanisms in TiAl intermetallics—experiments and modeling. *Int J Plast* 2003;19:281–321.

- [169] Salem AA, Kalidindi SR, Semiatin SL. Strain hardening due to deformation twinning in  $\alpha$ -titanium: constitutive relations and crystal-plasticity modeling. *Acta Mater* 2005;53:3495–502.
- [170] Wang Y, Raabe D, Klüber C, Roters F. Orientation dependence of nanoindentation pile-up patterns and of nanoindentation microtextures in copper single crystals. *Acta Mater* 2004;52:2229–38.
- [171] Zaaferani N, Raabe D, Singh RN, Roters F, Zaefferer S. Three dimensional investigation of the texture and microstructure below a nanoindent in a Cu single crystal using 3D EBSD and crystal plasticity finite element simulations. *Acta Mater* 2006;54:1707–994.
- [172] Raabe D, Ma D, Roters F. Effects of initial orientation, sample geometry and friction on anisotropy and crystallographic orientation changes in single crystal microcompression deformation: a crystal plasticity finite element study. *Acta Mater* 2007;55:4567–83.
- [173] Casals O, Ocenasek J, Alcalá J. Crystal plasticity finite element simulations of pyramidal indentation in copper single crystals. *Acta Mater* 2007;55:55–68.
- [174] Zaaferani N, Raabe D, Roters F, Zaefferer S. On the origin of deformation-induced rotation patterns below nanoindents. *Acta Mater* 2008;56:31–42.
- [175] Alcalá J, Casals O, Ocenasek J. Micromechanics of pyramidal indentation in fcc metals: single crystal plasticity finite element analysis. *J Mech Phys Solids* 2008;56:3277–303.
- [176] Weber F, Schestakow I, Roters F, Raabe D. Texture evolution during bending of a single crystal copper nanowire studied by EBSD and crystal plasticity finite element simulations. *Adv Eng Mater* 2008;10:737–41.
- [177] Demir E, Raabe D, Zaaferani N, Zaefferer S. Experimental investigation of geometrically necessary dislocations beneath small indents of different depths using EBSD tomography. *Acta Mater* 2009;57:559–69.
- [178] Miehe C. Exponential map algorithm for stress updates in anisotropic multiplicative elastoplasticity for single crystals. *Int J Numer Methods Eng* 1996;39:3367–90.
- [179] Bachu V, Kalidindi SR. On the accuracy of the predictions of texture evolution by the finite element technique for fcc polycrystals. *Mater Sci Eng A* 1998;257:108–17.
- [180] Harewood FJ, McHugh PE. Investigation of finite element mesh independence in rate dependent materials. *Comput Mater Sci* 2006;37:442–53.
- [181] Amirkhizi AV, Nemat-Nasser S. A framework for numerical integration of crystal elasto-plastic constitutive equations compatible with explicit finite element codes. *Int J Plast* 2007;23:1918–37.
- [182] Harewood FJ, McHugh PE. Comparison of the implicit and explicit finite element methods using crystal plasticity. *Comput Mater Sci* 2007;39:481–94.
- [183] Kuchnicki SN, Cuitiño AM, Radovitzky RA. Efficient and robust constitutive integrators for single-crystal plasticity modeling. *Int J Plast* 2006;22:1988–2011.
- [184] Melchior MA, Delannay L. A texture discretization technique adapted to polycrystalline aggregates with non-uniform grain size. *Comput Mater Sci* 2006;37:557–64.
- [185] Zhao Z, Kuchnicki S, Radovitzky R, Cuitiño A. Influence of in-grain mesh resolution on the prediction of deformation textures in fcc polycrystals by crystal plasticity FEM. *Acta Mater* 2007;55:2361–73.
- [186] Li HW, Yang H, Sun ZC. A robust integration algorithm for implementing rate dependent crystal plasticity into explicit finite element method. *Int J Plast* 2008;24:267–88.
- [187] Ritz H, Dawson PR. Sensitivity to grain discretization of the simulated crystal stress distributions in FCC polycrystals. *Modell Simul Mater Sci Eng* 2009;17.
- [188] Barton NR, Knap J, Arsenlis A, Becker R, Hornung RD, Jefferson DR. Embedded polycrystal plasticity and adaptive sampling. *Int J Plast* 2001;24:242–66.
- [189] Bruzzi MS, McHugh PE, O'Rourke F, Linder T. Micromechanical modelling of the static and cyclic loading of an Al 2124-SiC MMC. *Int J Plast* 2001;17:565–99.
- [190] Turkmen HS, Dawson PR, Miller MP. The evolution of crystalline stresses of a polycrystalline metal during cyclic loading. *Int J Plast* 2002;18:941–69.
- [191] Turkmen HS, Loge RE, Dawson PR, Miller MP. On the mechanical behavior of AA 7075-t6 during cyclic loading. *Int J Fatigue* 2003;25:267–81.
- [192] Kysar JW, Gan YX, Mendez-Arzuza G. Cylindrical void in a rigid-ideally plastic single crystal. Part I: anisotropic slip line theory solution for face-centered cubic crystals. *Int J Plast* 2005;21:1481–520.
- [193] Sinha S, Ghosh S. Modeling cyclic ratcheting based fatigue life of HSLA steels using crystal plasticity FEM simulations and experiments. *Int J Fatigue* 2006;28:1690–704.
- [194] Potirniche GP, Hearndon JL, Horstemeyer MF, Ling XW. Lattice orientation effects on void growth and coalescence in fcc single crystals. *Int J Plast* 2006;22:921–42.
- [195] Zhang M, Zhang J, McDowell DL. Microstructure-based crystal plasticity modeling of cyclic deformation of Ti–6Al–4V. *Int J Plast* 2007;23:1328–48.
- [196] Cheong K-S, Smillie MJ, Knowles DM. Predicting fatigue crack initiation through image-based micromechanical modeling. *Acta Mater* 2007;55:1757–68.
- [197] Dunne FPE, Walker A, Rugg D. A systematic study of hcp crystal orientation and morphology effects in polycrystal deformation and fatigue. *Proc Roy Soc Lond A* 2007;463:1467–89.
- [198] Liu WH, Zhang XM, Tang JG, Du Y. Simulation of void growth and coalescence behavior with 3D crystal plasticity theory. *Comput Mater Sci* 2007;40:130–9.
- [199] Bieler TR, Eisenlohr P, Roters F, Kumar D, Mason DE, Crimp MA, et al. The role of heterogeneous deformation on damage nucleation at grain boundaries in single phase metals. *Int J Plast* 2009;25:1655–83.
- [200] Kumar D, Bieler TR, Eisenlohr P, Mason DE, Crimp MA, Roters F, et al. On predicting nucleation of microcracks due to slip-twin interactions at grain boundaries in duplex  $\gamma$ -TiAl. *J Eng Mater Technol* 2008;130:021012-1–021012-12.
- [201] Patil SD, Narasimhan R, Biswas P, Mishra RK. Crack tip fields in a single edge notched aluminum single crystal specimen. *J Eng Mater Technol* 2008;130:021013.
- [202] Watanabe I, Terada K, deSouza EA, Peric D. Characterization of macroscopic tensile strength of polycrystalline metals with two-scale finite element analysis. *J Mech Phys Solids* 2008;56:1105–25.
- [203] Mayama T, Sasaki K, Kuroda M. Quantitative evaluations for strain amplitude dependent organization of dislocation structures due to cyclic plasticity in austenitic stainless steel 316L. *Acta Mater* 2008;56:2735–43.
- [204] Hartig C, Mecking H. Finite element modelling of two phase FeCu polycrystals. *Comput Mater Sci* 2005;32:370–7.
- [205] Tjahjanto DD, Roters F, Eisenlohr P. Iso-work-rate weighted-Taylor homogenization scheme for multiphase steels assisted by transformation-induced plasticity effect. *Steel Res Int* 2007;78:777–83.
- [206] Inal K, Simha HM, Mishra RK. Numerical modeling of second-phase particle effects on localized deformation. *J Eng Mater Technol* 2008;130:021003.
- [207] Vogler TJ, Clayton JD. Heterogeneous deformation and spall of an extruded tungsten alloy: plate impact experiments and crystal plasticity modeling. *J Mech Phys Solids* 2008;56:297–335.
- [208] Anand L, Sun C. A theory for amorphous viscoplastic materials undergoing finite deformations, with application to metallic glasses. *J Mech Phys Solids* 2005;53:1362–96.
- [209] Anand L, Su C. A constitutive theory for metallic glasses at high homologous temperatures. *Acta Mater* 2007;55:3735–47.
- [210] Nye JF. Some geometrical relations in dislocated crystals. *Acta Metall* 1953;1:153–62.
- [211] Kröner E. *Kontinuumstheorie der Versetzungen und Eigenspannungen*. Berlin: Springer; 1958 [in German].



- [212] Ashby MF. The deformation of plastically non-homogeneous materials. *Philos Mag* 1970;21:399–424.
- [213] Kröner E. Continuum theory of defects. In: *Physics of defects*. Amsterdam, Netherlands: North-Holland Publishing Company; 1981. p. 217.
- [214] Larson BC, Yang W, Ice GE, Swadener JG, Budai JD, Tischler JZ. Three-dimensional X-ray structural microscopy with submicrometre resolution. *Nature* 2002;415:887–90.
- [215] Kuo J-C, Zaefferer S, Zhao Z, Winning M, Raabe D. Deformation behaviour of aluminium-Bicrystals. *Adv Eng Mater* 2003;5:563–6.
- [216] Zaefferer S, Wright SI, Raabe D. 3D-orientation microscopy in a FIB SEM: a new dimension of microstructure characterisation. *Metall Mater Trans A* 2008;39:374–89.
- [217] Kraska M, Doig M, Tikhomirov D, Raabe D, Roters F. Virtual material testing for stamping simulations based on polycrystal plasticity. *Comput Mater Sci* 2009;46:383–92.
- [218] Courant R. Variational methods for the solution of problems of equilibrium and vibrations. *Bull Am Math Soc* 1943;49:1–23.
- [219] Zienkiewicz OC, Taylor RL, Zhu JZ. The finite element method: its basis and fundamentals. 6th ed. Butterworth-Heinemann; 2005.
- [220] Zienkiewicz OC, Taylor RL, Nithiarasu P. The finite element method for fluid dynamics. 6th ed. Butterworth-Heinemann; 2005.
- [221] Taylor GI. The mechanism of plastic deformation of crystals. Part I—theoretical. *Proc Roy Soc Lond A* 1934;145:362–87.
- [222] Taylor GI. The mechanism of plastic deformation of crystals. Part II—comparison with observations. *Proc Roy Soc Lond A* 1934;145:388–404.
- [223] Orowan E. Zur Kristallplastizität I–III. *Z Phys* 1934;89:605–59.
- [224] Polanyi M. Über eine Art Gitterstörung, die einen Kristall plastisch machen könnte. *Z Phys* 1934;89:660–4.
- [225] Harren SV, Dève H, Asaro RJ. Shear band formation in plane strain compression. *Acta Metall* 1988;36:2435–80.
- [226] Harren SV, Asaro RJ. Nonuniform deformations in polycrystals and aspects of the validity of the Taylor model. *J Mech Phys Solids* 1989;37:191–232.
- [227] Tóth LS, Van Houtte P. Discretization techniques for orientation distribution functions. *Texture Microstruct* 1992;19:229–44.
- [228] Eisenlohr P, Roters F. Selecting a set of discrete orientations for accurate texture reconstruction. *Comput Mater Sci* 2008;42:670–8.
- [229] Fleck NA, Muller GM, Ashby MF, Hutchinson JW. Strain gradient plasticity: theory and experiment. *Acta Metall Mater* 1994;42:475–87.
- [230] Fleck NA, Hutchinson JW. Strain gradient plasticity. *Advances in applied mechanics*, vol. 33. New York: Academic Press; 1997. p. 1825–57.
- [231] Nix WD, Gao H. Indentation size effects in crystalline materials: a law of strain gradient plasticity. *J Mech Phys Solids* 1998;46: 411–25.
- [232] Gao H, Huang Y. Geometrically necessary dislocation and size-dependent plasticity. *Scripta Mater* 2003;48(2):113–8.
- [233] Ma A, Roters F, Raabe D. Studying the effect of grain boundaries in dislocation density based crystal plasticity finite element simulations. *Int J Solids Struct* 2006;43:7287–303.
- [234] Suiker ASJ, Turteltaub S. Computational modelling of plasticity induced by martensitic phase transformations. *Int J Numer Methods Eng* 2005;63:1655–93.
- [235] Bilby BA. Continuum distributions of dislocations. *Progress in solid mechanics*, vol. 1. Amsterdam, Netherlands: North-Holland Publishing Company; 1960. p. 331.
- [236] Bilby BA, Gardner LRT, Smith E. The relation between dislocation density and stress. *Acta Metall* 1958;6:29–33.
- [237] Kröner E. Allgemeine Kontinuumstheorie der Versetzungen und Eigenspannungen. *Arch Ration Mech Anal* 1959;4:273–334.
- [238] Lee EH, Liu DT. Finite-strain elastic–plastic theory with application to plane-wave analysis. *J Appl Phys* 1967;38:19–27.
- [239] Bilby BA, Bullough R, Smith E. Continuous distributions of dislocations: a new application of the methods of non-Riemannian geometry. *Proc Roy Soc Lond A* 1955;231:263–73.
- [240] Hutchinson JW. Bounds and self-consistent estimates for creep of polycrystalline materials. *Proc Roy Soc Lond A* 1976;348:1001–127.
- [241] Voce E. The relationship between stress and strain for homogeneous deformation. *J Inst Met* 1948;74:537–62.
- [242] Kocks UF. Laws of work-hardening and low temperature creep. *J Eng Mater Technol* 1976;98:76–83.
- [243] Kocks UF. A statistical theory of flow stress and work-hardening. *Philos Mag* 1966;13:541.
- [244] Mecking H, Kocks UF. Kinetics of flow and strain hardening. *Acta Metall* 1986;29:1865–75.
- [245] Hall EO. The deformation and ageing of mild steel. III: discussion of results. *Proc Phys Soc B* 1951;64:747.
- [246] Petch NJ. The cleavage strength of polycrystals. *J Iron Steel Inst* 1953;25.
- [247] Nemat-Nasser S, Ni L, Okinaka T. A constitutive model for fcc crystals with application to polycrystalline OFHC copper. *Mech Mater* 1998;30(4):325–41.
- [248] Shen Z, Wagoner RH, Clark WAT. Dislocation pile-up and grain boundary interactions in 304 stainless steel. *Scripta Metall* 1986;20(6):921–6.
- [249] Clark WAT, Wagoner RH, Shen ZY, Lee TC, Robertson IM, Birnbaum HK. On the criteria for slip transmission across interfaces in polycrystals. *Scripta Metall Mater* 1992;26(2):203–6.
- [250] Jacques JP, Ladrrière J, Delannay F. On the influence of interactions between phases on the mechanical stability of retained austenite in transformation-induced plasticity multiphase steels. *Metall Mater Trans A* 2001;32:2759–68.
- [251] Greenwood GW, Johnson RH. The deformation of metals under small stresses during phase transformation. *Proc Roy Soc Lond A* 1965;283:403.
- [252] Fischer FD, Reisner G, Werner EA, Tanaka K, Cailletaud G, Antretter T. A new view on transformation-induced plasticity (TRIP). *Int J Plast* 2000;16:723–48.
- [253] Patel JR, Cohen M. Criterion for the action of applied stress in martensitic transformation. *Acta Metall* 1953;1(5):531–8.
- [254] Wechsler MS, Lieberman DE, Read TA. On the theory of the formation of martensite. *Appl Phys A—Mater* 1953;19(11):1503–15.
- [255] Ball JM, James RD. Fine phase mixtures as minimizers of energy. *Arch Ration Mech Anal* 1987;100(1):13–52.
- [256] Olson GB, Cohen M. Kinetics of strain-induced martensitic nucleation. *Metall Trans A* 1975;6(4):791–5.
- [257] Stringfellow RG, Parks DM, Olson GB. A constitutive model for transformation plasticity accompanying strain-induced martensitic transformations in metastable austenitic steels. *Acta Metall Mater* 1992;40(7):1703–16.
- [258] Leblond JB, Mottet G, Devaux JC. A theoretical and numerical approach to the plastic behaviour of steels during phase-transformation—I. Derivation of general relations. *J Mech Phys Solids* 1986;34:395–409.
- [259] Leblond JB, Mottet G, Devaux JC. A theoretical and numerical approach to the plastic behaviour of steels during phase-transformation—II. Study of classical plasticity for ideal-plastic phases. *J Mech Phys Solids* 1986;34:411–32.
- [260] Bhattacharyya A, Weng GJ. An energy criterion for the stress-induced martensitic transformation in a ductile system. *J Mech Phys Solids* 1994;42:1699–724.
- [261] Levitas VI, Idesman AV, Stein E. Shape memory alloys: micromechanical modeling and numerical analysis of structures. *J Intell Mater Syst Struct* 1999;10:983–96.
- [262] Levitas VI, Idesman AV, Olson GB. Continuum modeling of strain-induced martensitic transformation at shear-band intersections. *Acta Mater* 1999;47(1):219–33.
- [263] Turteltaub S, Suiker ASJ. A multi-scale thermomechanical model for cubic to tetragonal martensitic phase transformations. *Int J Solids Struct* 2006;43:4509–45.
- [264] Hull D, Bacon DJ. Introduction to dislocations. 4th ed. Butterworth-Heinemann; 2001.

- [265] Duesbery MS, Vitek V. Plastic anisotropy in BCC transition metals. *Acta Mater* 1998;46(5):1481–92.
- [266] Bassani JL, Ito K, Vitek V. Complex macroscopic plastic flow arising from non-planar dislocation core structures. *Mater Sci Eng A* 2001;319–321:97–101.
- [267] Vitek V, Mrovec M, Gröger R, Bassani JL, Racherla V, Yin L. Effects of non-glide stresses on the plastic flow of single and polycrystals of molybdenum. *Mater Sci Eng A* 2004;387–389:138–42.
- [268] Tjahjanto DD, Turteltaub S, Suiker ASJ, van der Zwaag S. Modelling of the effects of grain orientation on transformation-induced plasticity in multiphase steels. *Modell Simul Mater Sci Eng* 2006;14:617–36.
- [269] Hirth JP, Lothe J. Theory of dislocations. 2nd ed. Krieger Publishing Company–John Wiley & Sons, Ltd.; 1982.
- [270] Van Houtte P. Simulation of the rolling and shear texture of brass by the Taylor theory adapted for mechanical twinning. *Acta Metall* 1978;26:591–604.
- [271] Christian JW, Mahajan S. Deformation twinning. *Prog Mater Sci* 1995;39(1–2):1–157.
- [272] Bolling GF, Richman RH. Continual mechanical twinning: part I: formal description. *Acta Metall* 1965;13:709–45.
- [273] Köster W, Speidel MO. Der Einfluss der Temperatur und der Korngröße auf die ausgeprägte Streckgrenze von Kupferlegierungen. *Z Metallkd* 1965;9:1050 [in German].
- [274] Mahajan S, Williams DF. Deformation twinning in metals and alloys. *Int Met Rev* 1973;18:43.
- [275] Venables JA. In: Reed-Hill RE, Hirth JP, Rogers HC, editors. Deformation twinning. New York: Gordon & Breach; 1964.
- [276] Harding J. The yield and fracture behaviour of high-purity iron single crystals at high rates crystals at high rates of strain. *Proc Roy Soc Lond A* 1967;299:464–90.
- [277] Harding J. Yield and fracture of high-purity iron single crystals under repeated tensile impact loading. *Mem Sci Rev Met* 1968;65:245.
- [278] Hokka M, Kuokkala V-T, Curtze S, Vuoristo T, Apostol M. Characterization of strain rate and temperature dependent mechanical behavior of TWIP steels. *J Phys IV* 2006;134:1301–6.
- [279] Armstrong R, Worthington PJ. In: Rohde RW, Butcher BM, Holland JR, Karnes CH, editors. Metallurgical effects at high strain rates. New York: Plenum Press; 1973.
- [280] Vöhringer O. Einsatzspannung für mechanische Zwillingsbildung bei  $\alpha$ -Kupferlegierungen. *Z Metallkd* 1976;67:518–24.
- [281] Song SG, Gray III GT. Influence of temperature and strain rate on slip and twinning behavior of Zr. *Metall Mater Trans A* 1995;26:2665–75.
- [282] Meyers MA, Andrade UR, Chokshi AH. Effect of grain size on the high-strain, high-strain-rate behavior of copper. *Metall Mater Trans A* 1995;26:2881–93.
- [283] El-Dana E, Kalidindi SR, Doherty RD. Influence of grain size and stacking fault energy on deformation twinning in FCC metals. *Metall Mater Trans A* 1998;30:1223.
- [284] Rémy L. Maclage et transformation martensitique CFC-HC induite par déformation plastique dans les alliages austéniques à basse énergie de défaut d'empilement des systèmes Co–Ni–Cr–Mo et Fe–Mn–Cr–C. PhD thesis, ENSMP; 1975.
- [285] Karaman I, Sehitoglu H, Gall K, Chumlyakov YI. On the deformation mechanisms in single crystal Hadfield manganese steels. *Scripta Mater* 1998;38:1009–15.
- [286] Karaman I, Sehitoglu H, Gall K, Chumlyakov YI, Maier HJ. Deformation of a single crystal Hadfield steel by twinning and slip. *Acta Mater* 2000;48:1345–59.
- [287] Doquet V. Twinning and multiaxial cyclic plasticity of a low stacking-fault-energy f.c.c. alloy. *Acta Metall Mater* 1993;41:2451–9.
- [288] Schlögl SM, Fischer FD. The role of slip and twinning in the deformation behaviour of polysynthetically twinned crystals of TiAl: a micromechanical model. *Philos Mag A* 1997;75: 621–36.
- [289] Mecking H, Hartig C, Kocks UF. Deformation modes in gamma-TiAl as derived from the single crystal yield surface. *Acta Mater* 1996;44:1309–21.
- [290] Kalidindi SR. A crystal plasticity framework for deformation twinning. In: Continuum scale simulation of engineering materials. Wiley-VCH; 2004. p. 543–60.
- [291] Meng L, Yang P, Xie Q, Ding H, Tang Z. Dependence of deformation twinning on grain orientation in compressed high manganese steels. *Scripta Mater* 2007;56:931–4.
- [292] Salem AA, Kalidindi SR, Doherty RD, Semiatin SL. Strain hardening due to deformation twinning in  $\alpha$ -titanium: mechanics. *Metall Mater Trans A* 2006;37:259–68.
- [293] Bunge HJ. Texture analysis in materials science. London: Butterworths; 1982.
- [294] Böhlke T, Haus U-U, Schulze V. Crystallographic texture approximation by quadratic programming. *Acta Mater* 2006;54:1359–68.
- [295] Smit RJM, Brekelmans WAM, Meijer HEH. Prediction of the mechanical behavior of nonlinear heterogeneous systems by multi-level finite element modeling. *Comput Methods Appl Mech Eng* 1998;155(1–2):181–92.
- [296] Feyel F, Chaboche JL. FE<sup>2</sup> multiscale approach for modelling the elastoviscoplastic behaviour of long fibre SiC/Ti composite materials. *Comput Methods Appl Mech Eng* 2000;183(3–4):309–30.
- [297] Kouznetsova V, Brekelmans WAM, Baaijens FPT. An approach to micro–macro modeling of heterogeneous materials. *Comput Mech* 2001;27(1):37–48.
- [298] Miehe C, Schotte J, Lambrecht M. Homogenization of inelastic solid materials at finite strains based on incremental minimization principles. Application to the texture analysis of polycrystals. *J Mech Phys Solids* 2002;50(10):2123–67.
- [299] Moulinec H, Suquet P. A numerical method for computing the overall response of nonlinear composites with complex microstructure. *Comput Methods Appl Mech Eng* 1998;157(1–2):69–94.
- [300] Lebensohn RA. N-site modeling of a 3D viscoplastic polycrystal using fast Fourier transform. *Acta Mater* 2001;49(14):2723–37.
- [301] Reuss A. Berechnung der Fließgrenze von Mischkristallen auf Grund der Plastizitätsbedingung für Einkristalle. *Z Angew Math Mech* 1929;9:49–58 [in German].
- [302] Voigt W. Über die Beziehung zwischen den beiden Elastizitätskonstanten isotroper Körper. *Wied Ann* 1889;38:573–87 [in German].
- [303] Eshelby JD. The determination of the elastic field of an ellipsoidal inclusion, and related problems. *Proc Roy Soc Lond A* 1957;241:376–96.
- [304] Nemat-Nasser S, Hori M. Micromechanics: overall properties of heterogeneous materials. 2nd ed. Amsterdam: Elsevier; 1999.
- [305] Kröner E. Berechnung der elastischen Konstanten des Vielkristalls aus den Konstanten des Einkristalls. *Z Phys* 1958;151:504–18 [in German].
- [306] Mori T, Tanaka K. Average stress in matrix and average elastic energy of materials with misfitting inclusions. *Acta Metall* 1973;21(5):571–4.
- [307] Benveniste Y. A new approach to the application of Mori–Tanaka's theory in composite materials. *Mech Mater* 1987;6(2):147–57.
- [308] Hill R. Continuum micro-mechanics of elastoplastic polycrystals. *J Mech Phys Solids* 1965;13(2):89–101.
- [309] Lebensohn RA, Tomé CN. A self-consistent anisotropic approach for the simulation of plastic deformation and texture development of polycrystals: application to zirconium alloys. *Acta Metall Mater* 1993;41(9):2611–24.
- [310] Berveiller M, Zaoui A. An extension of the self-consistent scheme to plastically-flowing polycrystals. *J Mech Phys Solids* 1978;26(5–6): 325–44.
- [311] Masson R, Bornert M, Suquet P, Zaoui A. An affine formulation for the prediction of the effective properties of nonlinear composites and polycrystals. *J Mech Phys Solids* 2000;48(6–7):1203–27.
- [312] Doghri I, Ouair A. Homogenization of two-phase elasto-plastic composite materials and structures: study of tangent operators, cyclic plasticity and numerical algorithms. *Int J Solids Struct* 2003;40(7):1681–712.

- [313] Delannay L, Doghri I, Pierard O. Prediction of tension–compression cycles in multiphase steel using a modified incremental mean-field model. *Int J Solids Struct* 2007;44(22–23):7291–306.
- [314] Van Houtte P. On the equivalence of the relaxed Taylor theory and the Bishop–Hill theory for partially constrained plastic deformation of crystals. *Mater Sci Eng* 1982;55(1):69–77.
- [315] Van Houtte P. A comprehensive mathematical formulation of an extended Taylor–Bishop–Hill model featuring relaxed constraints, the Renouard–Wintenberger theory and a strain rate sensitivity model. *Texture Microstruct* 1988;8–9:313–50.
- [316] Honneff H, Mecking H. A method for the determination of the active slip systems and orientation changes during single crystal deformation. In: Gottstein G, Lücke K, editors. *Proceedings of the 5th international conference on texture of materials (ICOTOM-5)*, Aachen. Berlin: Springer; 1978. p. 265.
- [317] Kocks UF, Chandra H. Slip geometry in partially constrained deformation. *Acta Metall* 1982;30:695–709.
- [318] Van Houtte P, Li S, Seefeldt M, Delannay L. Deformation texture prediction: from the Taylor model to the advanced Lamel model. *Int J Plast* 2005;21(3):589–624.
- [319] Crumbach M, Pomana G, Wagner P, Gottstein G. A Taylor type deformation texture model considering grain interaction and material properties. Part I—fundamentals. In: Gottstein G, Molodov DA, editors. *Proceedings of the first joint international conference on recrystallisation and grain growth*. Berlin: Springer; 2001. p. 1053–60.
- [320] Wagner P. Zusammenhänge zwischen mikro- und makroskopischen Verformungsinhomogenitäten und der Textur. PhD thesis, RWTH Aachen; 1994.
- [321] Schäfer C, Song J, Gottstein G. Modeling of texture evolution in the deformation zone of second-phase particles. *Acta Mater* 2009;57:1026–34.
- [322] Clayton JD, McDowell DL. Homogenized finite elastoplasticity and damage: theory and computations. *Mech Mater* 2004;36:825–47.
- [323] Clayton JD. Modeling dynamic plasticity and spall fracture in high density polycrystalline alloys. *Int J Solids Struct* 2005;42:4613–40.
- [324] Clayton JD. Dynamic plasticity and fracture in high density polycrystals: constitutive modeling and numerical simulation. *J Mech Phys Solids* 2005;53:261–301.
- [325] Lehockey EM, Palumbo G. On the creep behaviour of grain boundary engineered nickel. *Mater Sci Eng A* 1997;237:168–72.
- [326] Nicolaou PD, Semiatin SL. An analysis of the effect of continuous nucleation and coalescence on cavitation during hot tension testing. *Acta Mater* 2000;48:3441–50.
- [327] Nicolaou PD, Semiatin SL. Hybrid micromechanical–macroscopic model for the analysis of tensile behavior of cavitating materials. *Metall Mater Trans A* 2003;34.
- [328] Horstemeyer MF, Ramaswamy S, Negrete M. Using a micromechanical finite element parametric study to motivate a phenomenological macroscale model for void/crack nucleation in aluminum with a hard second phase. *Mech Mater* 2003;35:675–87.
- [329] Pardoën T, Dumont D, Deschamps A, Brechet Y. Grain Boundary versus transgranular ductile failure. *J Mech Phys Solids* 2003;51:637.
- [330] Wilkinson DS, Pompe W, Oeschner M. Modeling the mechanical behavior of heterogeneous multi-phase materials. *Progress in Materials Science* 2001;46:379–405.
- [331] Lemaitre J, Chaboche J-L. *Mechanics of solid materials*. 2nd ed. Cambridge: Cambridge University Press; 1998.
- [332] Luccioni B, Oller S. A directional damage model. *Comput Methods Appl Mech Eng* 2003;192:1119–45.
- [333] Menzel A, Ekh M, Runesson K, Steinmann P. A framework for multiplicative elastoplasticity with kinematic hardening coupled to anisotropic damage. *Int J Plast* 2005;21:397–434.
- [334] Voyiadis GZ, Dorgan RJ. Framework using functional forms of hardening internal state variables in modeling elasto-plastic-damage behavior. *Int J Plast* 2007;23:1826–59.
- [335] Barlat F, Brem JC, Yoon JW, Chung K, Dick RE, Lege DJ, et al. Plane stress yield function for aluminum alloy sheets—part I: theory. *Int J Plast* 2002;19:1297–319.
- [336] Vasudevan AK, Doherty RD. Grain boundary ductile fracture in precipitation hardened aluminum alloys. *Acta Metall* 1987;35:1193–219.
- [337] Suresh S, Vasudevan AK, Tosten M, Howell PR. Microscopic and macroscopic aspects of fracture in lithium containing aluminum alloys. *Acta Metall* 1987;35:25–46.
- [338] Tsang J, Beddoes J, Merati A. Detection methods for nucleation and short fatigue cracks in 2025-T3 aluminum alloy. In: *Aerospace materials and manufacturing: development, testing, and life cycle issues*, MetSoc/CIM; 2004. p. 275–87.
- [339] Simonovski I, Nilsson KF, Cizelj L. The influence of crystallographic orientation on crack tip displacements of microstructurally small, kinked crack crossing the grain boundary. *Comput Mater Sci* 2007;39:817–28.
- [340] Dunne FPE, Wilkinson AJ, Allen R. Experimental and computational studies of low cycle fatigue crack nucleation in a polycrystal. *Int J Plast* 2007;23:273–95.
- [341] Thorning C, Somers MAJ, Wert JA. Grain interaction effects in polycrystalline Cu. *Mater Sci Eng A* 2005;397:215–28.
- [342] Tatschl A, Kolednik O. On the experimental characterization of crystal plasticity in polycrystals. *Mater Sci Eng A* 2003;342:152.
- [343] Cheong K-S, Busso EP. Effects of lattice misorientations on strain heterogeneities in FCC polycrystals. *J Mech Phys Solids* 2006;54:671–89.
- [344] Hao S, Liu WK, Moran B, Vernerey F, Olson GB. Multi-scale constitutive model and computational framework for the design of ultra-high strength, high toughness steels. *Comput Methods Appl Mech Eng* 2004;193:1865–908.
- [345] Dawson PR, Mika DP, Barton NR. Finite element modeling of lattice misorientations in aluminum polycrystals. *Scripta Mater* 2002;47:713–7.
- [346] Kalidindi SR, Anand L. Large deformation simple compression of a copper single crystal. *Metall Trans A* 1993;24:989–92.
- [347] Hao S, Moran B, Liu WK, Olson GB. A hierarchical multi-physics model for design of high toughness steels. *J. Computer-Aided Materials Design* 2003;10:99–142.
- [348] Liu WK, Karpov EG, Zhang S, Park HS. An introduction to computational nanomechanics and materials. *Comput Methods Appl Mech Eng* 2004;193:529–1578.
- [349] Voyiadis GZ, Abu Al-Rub RK, Palazotto AN. Thermodynamic framework for coupling of non-local viscoplasticity and non-local anisotropic viscodamage for dynamic localization problems using gradient theory. *Int J Plast* 2004;20:981–1038.
- [350] Buchheit TE, Wellman GW, Battaile CC. Investigating the limits of polycrystal plasticity modeling. *Int J Plast* 2005;21:221–49.
- [351] Watanabe T. An approach to grain-boundary design for strong and ductile polycrystals. *Res Mechanica* 1984;11:47–84.
- [352] Palumbo G, Lehockey EM, Lin P. Applications for grain boundary engineered materials. *JOM* 1998;50:40–3.
- [353] Watanabe T, Tsurekawa S. Toughening of brittle materials by grain boundary engineering. *Mater Sci Eng A* 2004;387–389:447–55.
- [354] Randle V. Twinning-related grain boundary engineering. *Acta Mater* 2004;52:4067–81.
- [355] Schuh CA, Kumar M, King WE. Analysis of grain boundary networks and their evolution during grain boundary engineering. *Acta Mater* 2003;51:687–700.
- [356] McGarrity ES, Duxbury PM, Holm EA. Statistical physics of grain-boundary engineering. *Phys Rev E* 2005;71(Pt. 2) [Art. No. 026102].
- [357] Kokawa H, Watanabe T, Karashima S. Sliding behavior and dislocation-structures in aluminum grain-boundaries. *Philos Mag A* 1981;44:1239.
- [358] Watanabe T, Tsurekawa S. Prediction and control of grain boundary fracture in brittle materials on the basis of the strongest-link theory. *Mater Sci Forum* 2005;485:55–62.



- [359] Needleman A. A continuum model for void nucleation by inclusion debonding. *J Appl Mech ASME* 1987;54:525–31.
- [360] Xu X-P, Needleman A. Numerical simulations of fast crack growth in brittle solids. *J Mech Phys Solids* 1994;42:1397–434.
- [361] Arata JJM, Kumar KS, Curtin WA, Needleman A. Crack growth across colony boundaries in binary lamellar TiAl. *Mater Sci Eng A* 2002;329:532–7.
- [362] Lejcek P, Paidar V. Challenges of interfacial classification for grain boundary engineering. *Mater Sci Technol* 2005;21:393–8.
- [363] Kawahara K, Ibaraki K, Tsurekawa S, Watanabe T. Distribution of plane matching boundaries for different types and sharpness of textures. *Mater Sci Forum* 2005;475–479:3871–4.
- [364] Wu MS, Nazarov AA, Zhou K. Misorientation dependence of the energy of [1–100] symmetrical tilt boundaries in hcp metals: prediction by the disclination-structural unit model. *Philos Mag* 2004;84:785–806.
- [365] Singh A, King AH. Tables of coincidence orientations for ordered tetragonal L1<sub>0</sub> alloys for a range of axial ratios. *Acta Cryst B* 1993;49:266–72.
- [366] Livingston JD, Chalmers B. Multiple slip in bicrystal deformation. *Acta Metall* 1957;5:322.
- [367] Werner E, Prantl W. Slip transfer across grain and phase boundaries. *Acta Metall Mater* 1990;38:3231–42.
- [368] de Koning M, Kurtz RJ, Bulatov VV, Henager CH, Hoagland RG, Cai W, et al. Modeling of dislocation-grain boundary interactions in FCC metals. *J. Nucl. Mater* 2003;323:281–9.
- [369] Luster J, Morris MA. Compatibility of deformation in two-phase Ti–Al alloys: dependence on microstructure and orientation relationships. *Metall Mater Trans A* 1995;26:1745.
- [370] Gibson MA, Forwood CT. Slip transfer of deformation twins in duplex gamma-based Ti–Al alloys. III. Transfer across general large-angle gamma–gamma grain boundaries. *Philos Mag A* 2002;82:1381.
- [371] Bollmann W. The stress-field of a model triple-line disclination. *Mater Sci Eng* 1991;136:1–7.
- [372] Randle V. The influence of grain junctions and boundaries on superplastic deformation. *Acta Metall Mater* 1995;43:1741–9.
- [373] Wu MS, He MD. Prediction of crack statistics in a random polycrystal damaged by the pile-ups of extrinsic grain-boundary dislocations. *Philos Mag* 1999;79:271–92.
- [374] Tsurekawa S, Kokubun S, Watanabe T. Effect of grain boundary microstructures of brittle fracture in polycrystalline molybdenum. *Mater Sci Forum* 1999;304(3):687–92.
- [375] Kobayashi S, Tsurekawa S, Watanabe T. Grain boundary hardening and triple junction hardening in polycrystalline molybdenum. *Acta Mater* 2005;53:1051–7.
- [376] Lim LC, Raj R. Continuity of slip screw and mixed-crystal dislocations across bicrystals of nickel at 573-K. *Acta Metall* 1985;33:1577.
- [377] Wang MG, Ngan AHW. Indentation strain burst phenomenon induced by grain boundaries in niobium. *J Mater Res* 2004;19:2478–86.
- [378] Sun S, Adams BL, King WE. Observations of lattice curvature near the interface of a deformed aluminium bicrystal. *Philos Mag A* 2000;80:9–25.
- [379] Ashmawi WM, Zikry MA. Grain boundary effects and void porosity evolution. *Mech Mater* 2003;35:537.
- [380] Simkin BA, Crimpand MA, Bieler TR. A factor to predict microcrack nucleation at  $\gamma$ – $\gamma$  grain boundaries in TiAl. *Scripta Mater* 2003;49:149–54.
- [381] Simkin BA, Ng BC, Bieler TR, Crimp MA, Mason DE. Orientation determination and defect analysis in the near-cubic intermetallic  $\gamma$ -TiAl using SACP, ECCI, and EBSD. *Intermetallics* 2003;11:215–23.
- [382] Ng BC, Bieler TR, Crimp MA, Mason DE. Prediction of crack paths based upon detailed microstructure characterization in a near- $\gamma$  TiAl alloy. In: *Materials damage prognosis*. Warrendale, PA: TMS; 2005. p. 307–14.
- [383] Bieler TR, Fallahi A, Ng BC, Kumar D, Crimp MA, Simkin BA, et al. Fracture initiation/propagation parameters for duplex TiAl grain boundaries based on twinning, slip, crystal orientation, and boundary misorientation. *Intermetallics* 2005;13:979–84.
- [384] Boehlert CJ, Longanbach SC, Bieler TR. The effect of thermomechanical processing on the creep behavior of Udimet alloy 188. *Philos Mag A* 2008;88:641–64.
- [385] Sinha V, Spowart MJ, Mills MJ, Williams JC. Observations on the faceted initiation site in the dwell-fatigue tested Ti-6242 alloy: crystallographic orientation and size effects. *Metall Mater Trans A* 2006;37:1507–18.
- [386] Bieler TR, Nicolaou PD, Semiatin SL. An experimental and theoretical investigation of the effect of local colony orientations and misorientation on cavitation during hot working of Ti–6Al–4V. *Metall Mater Trans A* 2005;36:129–40.
- [387] Bieler TR, Goetz RL, Semiatin SL. Anisotropic plasticity and cavity growth during upset forging of Ti–6Al–4V. *Mater Sci Eng A* 2005;405:201–13.
- [388] MSC.Marc User's Manual 2007, User Subroutines and Special Routines, vol. D. MSC; 2007.
- [389] Abaqus User Subroutines Reference Manual Version 6.7. Dassault Systèmes; 2007.
- [390] Sarma GB, Zacharia T. Integration algorithm for modeling the elasto-viscoplastic response of polycrystalline materials. *J Mech Phys Solids* 1999;47:1219–38.
- [391] Maniatty AM, Dawson PR, Lee Y-S. A time integration algorithm for elasto-viscoplastic cubic crystals applied to modelling polychrystalline deformation. *Int J Numer Methods Eng* 1992;35:1565–88.
- [392] Cuitiño AM, Ortiz M. Computational modelling of single crystals. *Modell Simul Mater Sci Eng* 1992;1:225–63.
- [393] Han C-S, Ma A, Roters F, Raabe D. A finite element approach with patch projection for strain gradient plasticity formulations. *Int J Plast* 2007;23:690–710.
- [394] Nielsen SF, Lauridsen EM, Juul Jensen D, Poulsen HF. A three-dimensional X-ray diffraction microscope for deformation studies of polycrystals. *Mater Sci Eng A* 2001;319–321:179–81.
- [395] Konrad J, Zaefferer S, Raabe D. Investigation of orientation gradients around a hard Laves particle in a warm rolled Fe<sub>3</sub>Al-based alloy by a 3D EBSD-FIB technique. *Acta Mater* 2006;54:1369–80.
- [396] Bastos A, Zaefferer S, Raabe D. 3-Dimensional EBSD study on the relationship between triple junctions and columnar grains in electrodeposited CoNi films. *J Microsc* 2008;230:487–98.
- [397] Uchic MD, Dimiduk DM, Florando JN, Nix WD. Sample dimensions influence strength and crystal plasticity. *Science* 2004;305:986–9.
- [398] Greer JR, Oliver WC, Nix WD. Size dependence of mechanical properties of gold at the microscale in the absence of strain gradients. *Acta Mater* 2005;53:1821–30.
- [399] Dimiduk DM, Uchic MD, Parthasarathy TA. Size affected single slip behavior of pure Ni microcrystals. *Acta Mater* 2005;53:4065–77.
- [400] Kiener D, Pippan R, Motz C, Kreuzer H. Microstructural evolution of the deformed volume beneath microindents in tungsten and copper. *Acta Mater* 2006;54:2801–11.
- [401] Zhao Z, Mao W, Raabe D. Influence of grain neighborhood on FCC texture simulation. *Mater Sci Forum* 2002;408–412:281–6.
- [402] Raabe D, Zhao Z, Roters F. *Mater Sci Forum* 2002;408–412:275–80.
- [403] Hölscher M, Raabe D, Lücke K. Relationship between rolling textures and shear textures in f.c.c. and b.c.c. metals. *Acta Metall* 1994;42:879–86.
- [404] Ma A, Roters F, Raabe D. A dislocation density based constitutive law for BCC materials in crystal plasticity FEM. *Comput Mater Sci* 2007;39:91–5.
- [405] Roters F, Raabe D, Gottstein G. Work hardening in heterogeneous alloys—a microstructural approach based on three internal state variables. *Acta Mater* 2000;48:4181–9.
- [406] Kuo J-C. Mikrostrukturmechanik von Bikristallen mit Kippkorn-grenzen. PhD thesis, Germany: RWTH Aachen; 2003.

- [407] Raabe D. Introduction of a scaleable 3D cellular automaton with a probabilistic switching rule for the discrete mesoscale simulation of recrystallization phenomena. *Philos Mag A* 1999;79:2339–58.
- [408] Raabe D. Mesoscale simulation of recrystallization textures and microstructures. *Adv Eng Mater* 2001;3:745–52.
- [409] Kruijver SO, Zhao L, Sietsma J, Offerman SE, van Dijk NH, Lauridsen EM, et al. In situ observation on the mechanical stability of austenite in TRIP-steel. *J Phys IV* 2003;104:499–502.
- [410] Oliver EC, Whithers PJ, Daymond MR, Ueta S, Mori T. Neutron-diffraction study of stress-induced martensitic transformation in TRIP steel. *Appl Phys A—Mater Sci Proc* 2002;74:S1143–5.
- [411] Bockstedte M, Kley A, Neugebauer J, Scheffler M. Density-functional theory calculations for poly-atomic systems: electronic structure, static and elastic properties and ab initio molecular dynamics. *Comput Phys Commun* 1997;107:187–222.
- [412] Hill R. The elastic behavior of a crystalline aggregate. *Proc Roy Soc Lond A* 1952;65:349–54.
- [413] Hershey AV. The elasticity of an isotropic aggregate of anisotropic cubic crystals. *J Appl Mech ASME* 1954;21:236–40.
- [414] Counts WA, Friak M, Battaile CC, Raabe D, Neugebauer J. A comparison of polycrystalline elastic constants computed by analytic homogenization schemes and FEM. *Phys Status Solidi B* 2008;245:2644–9.
- [415] Ma D, Friak M, Neugebauer J, Raabe D, Roters F. Multiscale simulation of polycrystal mechanics of textured  $\beta$ -Ti alloys using ab initio and crystal-based finite element methods. *Phys Status Solidi B* 2008;245:2642–8.
- [416] Raabe D, Sander B, Friak M, Ma D, Neugebauer J. Theory-guided bottom-up design of beta-titanium alloys as biomaterials based on first principles calculations: theory and experiments. *Acta Mater* 2007;55:4475–87.
- [417] Raabe D. Simulation of rolling textures of bcc metals under consideration of grain interactions and  $\{110\}$ ,  $\{112\}$  and  $\{123\}$  slip planes. *Mater Sci Eng A* 1995;197:31–7.
- [418] Raabe D. Investigation of contribution of  $\{123\}$  slip planes to development of rolling textures in bcc metals by use of Taylor models. *Mater Sci Technol* 1995;11:455–60.
- [419] Raabe D, Lücke K. Textures of ferritic stainless steels. *Mater Sci Technol* 1993;9:302–12.
- [420] Fedosseev A, Raabe D. Application of the method of superposition of harmonic currents for the simulation of inhomogeneous deformation during hot rolling of FeCr. *Scripta Metall* 1994;30:1–6.
- [421] Hill R. A theory of the yielding and plastic flow of anisotropic metals. *Proc Roy Soc Lond A* 1948;193:281–97.
- [422] Müller S. Variational models for microstructure and phase transitions. In: Hildebrandt S, Struwe M, editors. *Lectures at the C.I.M.E. summer school on calculus of variations and geometric evolution problems*, vol. 2. Springer Lecture Notes in Mathematics, C.I.M.E. Lecture Notes, Cetraro; 1996. p. 85–210.
- [423] Ortiz M, Repetto EA. Non-convex energy minimization and dislocation structures in ductile single crystals. *J Mech Phys Solids* 1999;47:397–462.
- [424] Bhattacharya K. *Microstructure of martensite*. Oxford University Press; 2003.
- [425] Aubry S, Ortiz M. The mechanics of deformation-induced subgrain-dislocation structures in metallic crystals at large strains. *Proc Roy Soc Lond A* 2003;459:3131–58.
- [426] Conti S, Hauret P, Ortiz M. Concurrent multiscale computing of deformation microstructure by relaxation and local enrichment with application to single-crystal plasticity. *Multiscale Model Simul* 2007;6:135–57.
- [427] Dmitrieva O, Dondl PW, Müller S, Raabe D. Lamination microstructure in shear deformed copper single crystals. *Acta Mater* 2009;57:3439–49.
- [428] Böhlke T, Risy G, Bertram A. A texture component model for anisotropic polycrystal plasticity. *Comput Mater Sci* 2005;32:284–93.
- [429] Van Houtte P, Delannay L, Samajdar I. Quantitative prediction of cold rolling textures in low-carbon steel by means of the LAMEL model. *Texture Microstruct* 1999;31:109–49.
- [430] Eisenlohr P, Tjahjanto DD, Hochrainer T, Roters F, Raabe D. Comparison of texture evolution in fcc metals predicted by various grain cluster homogenization schemes. *Int J Mater Res* 2009;4:500–9.
- [431] Fressengeas C, Beaudoin AJ, Lebyodkin M, Kubin LP, Estrin Y. Dynamic strain aging: a coupled dislocation—solute dynamic model. *Mater Sci Eng A* 2005;400–401:226–30.
- [432] Huang HC, Van Swygenhoven H. Atomistic simulations of mechanics of nanostructures. *MRS Bull* 2009;34:160–2.
- [433] Counts WA, Friak M, Raabe D, Neugebauer J. Using ab initio calculations in designing bcc Mg–Li alloys for ultra light-weight applications. *Acta Mater* 2009;57:69–76.
- [434] Friak M, Counts WA, Raabe D, Neugebauer J. Error-propagation in multiscale approaches to the elasticity of polycrystals. *Phys Status Solidi B* 2008;245:2636–41.
- [435] Lebensohn RA, Brenner R, Castelnau O, Rollett AD. Orientation image-based micromechanical modelling of subgrain texture evolution in polycrystalline copper. *Acta Mater* 2008;56:3914–26.
- [436] Molinari A, Canova GR, Ahzi S. A self-consistent approach of the large deformation polycrystal viscoplasticity. *Acta Metall* 1987;35(12):2983–94.
- [437] Liu Y, Gilormini P, Ponte Castañeda P. Variational self-consistent estimates for texture evolution in viscoplastic polycrystals. *Acta Mater* 2003;51:5425–37.
- [438] Kalidindi SR, Duvvuru HK, Knezevic M. Spectral calibration of crystal plasticity models. *Acta Mater* 2006;54:1795–804.
- [439] Kalidindi SR, Binci M, Fullwood D, Adams BL. Elastic properties closures using second-order homogenization theories: case studies in composites of two isotropic constituents. *Acta Mater* 2006;54:3117–26.
- [440] Michel JC, Moulinec H, Suquet P. Effective properties of composite materials with periodic microstructure: a computational approach. *Comput Methods Appl Mech Eng* 1999;172:109–43.
- [441] Wu X, Proust G, Knezevic M, Kalidindi SR. Elastic–plastic property closures for hexagonal close-packed polycrystalline metals using first-order bounding theories. *Acta Mater* 2007;55:2729–37.
- [442] Hansen N. The effect of grain size and strain on the tensile flow stress of copper at room temperature. In: Haasen P, Gerold V, Kosterz G, editors. *Proceedings of the 5th international conference on the strength of metals and alloys*, vol. 2. Oxford: Pergamon Press; 1979. p. 849–54.